

**Royal Meteorological Institute of Belgium**

Scientific Report

---

**IONOSPHERE - PLASMASPHERE SYSTEM BEHAVIOUR  
AT DISTURBED AND EXTREME MAGNETIC CONDITIONS**


by

**STANIMIR M. STANKOV**

31 March 2002

The research reported in this document has been sponsored by  
the Belgian Federal Office for Scientific, Technical and Cultural Affairs

*Approved and submitted by*



---

*Jean-Claude Jodogne, Dr. Ir., Project Supervisor  
Head, Department of Geophysics*

---

Department of Geophysics, Royal Meteorological Institute of Belgium

2002

## ACKNOWLEDGEMENTS

I thank Dr. Jean-Claude Jodogne, Prof. Ivan Kutiev, Dr. René Warnant, Dr. Norbert Jakowski, and Dr. Jean Rasson for the helpful discussions.

The research has been financially supported by the Belgian Federal Office for Scientific, Technical and Cultural Affairs and the Royal Meteorological Institute of Belgium.

Thanks are also due to the Royal Observatory of Belgium and the DLR / Institute of Communication and Navigation for the data used in this report.

**Royal Meteorological Institute of Belgium**

**IONOSPHERE - PLASMASPHERE SYSTEM BEHAVIOUR  
AT DISTURBED AND EXTREME MAGNETIC CONDITIONS**

by

**STANIMIR M. STANKOV**

Brussels  
2002

## TABLE OF CONTENTS

<b>1. Introduction</b>	<b>1</b>
<b>2. Theory</b>	<b>3</b>
2.1 The solar wind	4
2.2 The Earth's magnetic field	5
2.3 Solar activity and indices	6
2.4 Geomagnetic activity and indices	7
2.5 Geomagnetic and ionospheric storms	8
2.6 Thermosphere - ionosphere coupling	9
2.7 Ionosphere - plasmasphere coupling	10
<b>3. Measurements</b>	<b>11</b>
3.1 Vertical incidence sounding of the ionosphere	13
3.2 GPS-based Total Electron Content	15
3.3 Geomagnetic observations	18
3.4 Cosmic rays	20
<b>4. Case studies of storms</b>	<b>23</b>
4.1 The storm on 10 January 1997	25
4.2 The storm on 15-17 July 2000	28
4.3 The storm on 31 March 2001	32
4.4 Discussion	35
<b>5. Synthetic index of local response to magnetic activity</b>	<b>37</b>
5.1 The index based on foF2 measurements	38
5.2 The index based on GPS TEC measurements	40
<b>6. A new method for TEC forecasting based on GPS measurements</b>	<b>43</b>
6.1 Monthly-median forecast	48
6.2 Geomagnetically-correlated short-term forecast	52
<b>7. A new method for reconstruction of the vertical electron density distribution based on GPS TEC, upper transition level and ionosonde measurements</b>	<b>55</b>
7.1 Mathematical formulation	57
7.2 Evaluation of analytical models used in electron profile reconstruction	65
7.3 Operational model for real-time reconstruction of the electron density	75
<b>8. Summary</b>	<b>85</b>
<b>References</b>	<b>87</b>

# 1. INTRODUCTION

‘Space weather’ is a term, denoting the complex interaction processes between the Sun and interplanetary space (with the radiation and atomic particles emitted) on the one hand, and the Earth on the other. In the highly-developed, and increasingly technology-dependent modern world, the knowledge of the space weather is becoming more and more important. The effects of this phenomenon are many and varied: they include electronic failures, telecommunication and navigation system breakdowns, geomagnetically-induced currents (GIC) damaging oil/gas pipelines and electric power transmissions, radiation hazardous to space- and air-craft crews, etc.

Space weather and its effects are determined primarily by the Sun, solar wind and solar/galactic cosmic rays, while the Earth’s magnetosphere, ionosphere, plasmasphere and thermosphere all bear the influence. The coupled thermosphere-ionosphere-plasmasphere system is therefore a very complex dynamic system responding quickly to those effects. All investigations of its inter-relationship are very difficult, expensive and insufficient, particularly regarding the periods of disturbed and extreme geomagnetic conditions.

The research reported here aims at improving the understanding of the ionosphere-plasmasphere response to the geomagnetic/ionospheric storms. It is a fact, that complex measurements provide better opportunity for such research, so various types of observations have been used – from traditional vertical ionospheric soundings to the very latest GPS-based TEC calculations. The primary source is the comprehensive database of the Dourbes Geophysics Centre of the Belgian Royal Meteorological Institute.

This report is organised in the following manner. First, basic theoretical considerations are given, related to the research topic. Next, the observations used are described in some detail. Further, results from four major topics of interest are presented: case studies of storms, local response to geomagnetic activity, TEC forecasting, and vertical electron density distribution reconstructed from TEC and ionosonde measurements.

The ionospheric storms, defined as the large ionosphere-plasmasphere perturbations, induced by the solar flares and coronal mass ejections, is still a challenging subject of investigation. Observations of the whole thermosphere-ionosphere-plasmasphere system response to storms have been well documented for several decades. Nevertheless, many questions stay unanswered and many early studies are now being questioned and improved by new discoveries. Traditionally, the 'geospheric' storm effects have been investigated by means of vertical radio-sounding measurement techniques (ionosondes) providing long series of data for the ionised atmospheric layers. Later, with the advancement of the satellite technology, in-situ observations of the plasma composition and behaviour has helped the research. Most recently, the GPS-measured TEC, both ground and space-based, contributed significantly for the knowledge of the storms' global development. In addition to the above methods, the numerical modelling approach allows the combination of various observations, better coupling with theoretical investigations, and spreading the information about essential processes and parameters over areas which are not directly observed. Presented are case studies of several major storms.

The response of a given ionosphere characteristic  $F$  (like  $f_oF_2$ ,  $M3000F_2$ , or TEC) is better analysed through the relative deviation,  $Fr = (F - F_{med})/F_{med}$ , of the actual observed characteristic from its median value,  $F_{med}$ . It strongly depends on the geomagnetic indices (e.g.  $A_p$  and  $K_p$ ) in a highly non-linear fashion. For developing geomagnetically-correlated short-term forecasting methods, a new synthetic index is required. This new synthetic index is actually a function showing the  $Fr$  dependence on the geomagnetic index (say  $K_p$ ) used for the forecast. However, the new synthetic index (function) demonstrates strong seasonal and spatial variability and should be determined for each measurement site separately. At Dourbes, there are two types of measurements that can be used for the purpose – ionosonde ( $f_oF_2$ ) and GPS-based TEC measurements.

The GPS-derived TEC has proved to be a robust characteristic best representing the ionospheric state during disturbed geomagnetic conditions. Long and short-term TEC forecasting is an important need in the communication and navigation practice. Presented is a new forecasting method consisting of two major parts: (i) TEC monthly median extrapolation (up to 15 days ahead) using Fourier series approximation based on actual data from the past 12 months. (ii) Forecast of the relative deviations of measured TEC from its median values (up to 24 hours ahead) using the  $K_p$  index and adjusted through an auto-correlation procedure. Preliminary tests show a good agreement between measured and predicted values.

A new formula of the electron density profiles above the peak height is introduced. The formula is based on the Epstein layer and depends on the  $O^+$  and  $H^+$  scale heights and the  $O^+ - H^+$  transition level. Both scale heights have a ratio 1:16 reduced by a factor representing the change from magnetic field line direction to vertical direction. The bottom-side part of TEC (profile calculations using  $f_oF_2$ ,  $M_{3000}F_2$  and  $f_oE$ ) is subtracted from the GPS-measured TEC at the same location. The topside TEC, together with the empirically obtained  $O^+ - H^+$  transition level, are then used to deduce the unknown scale heights. The method is demonstrated on genuine data covering low and high solar activity conditions. Opportunities for an operational reconstruction model are also investigated.

Although global investigations are required for such a complicated topic as the ionosphere-plasmasphere response, long-term complex local observations can be very helpful for higher precision developments and research.

## 2. THEORY

The content of this chapter outlines the basic theoretical details related to the Earth's thermosphere–ionosphere–plasmasphere system and the geomagnetic/ionospheric storms.

Due to the nuclear fusion within the Sun and the acceleration processes occurring in its atmosphere, the Sun emits electromagnetic and partial radiation, which jointly maintain the Earth's ionosphere-plasmasphere system. The solar wind strikes the Earth's magnetic field, imparting a comet-like shape to the magnetosphere. So, first some information concerning the solar wind and the geomagnetic field is provided.

Next, the solar and geomagnetic activity is discussed together with the corresponding indices. The period between two successive maxima in the relative number of sunspots is on average eleven years, the peaks and troughs being known as the solar maximum and solar minimum. Variations are also observed in the geomagnetic activity. Therefore, some qualitative information should be available for reference and facilitation of research. Indices are used to monitor and describe the evolution of a physical phenomenon varying as a function of time. An index is defined as a number aiming at representing the amplitude of a physical parameter. A good index should establish sets of discrete values providing reliable, pertinent, and concentrated information.

Finally, some important topics related to the thermosphere-ionosphere and ionosphere-plasmasphere coupling processes are presented.

## 2.1 The solar wind

Due to the nuclear fusion within the Sun, it emits electromagnetic and particle radiation. The electromagnetic radiation stretches through the entire spectrum - from gamma, X-ray and ultraviolet radiation, through the visible light, to the infrared and solar radio radiation. A common feature of the electromagnetic radiation is that the photons (the light quanta carrying the energy and momentum of a light wave) have a velocity of 300000 km/s, thus covering the distance between the Sun and Earth (150 million km) in only about eight minutes.

Because the solar corona is not in hydrostatic equilibrium, but is expanding continuously, matter leaves the Sun and flows out into space. From optical observations and theoretical calculations, it is found that beyond 15 or 20 solar radii the outward convective acceleration exceeds the inward gravitational acceleration, and therefore matter leaves the Sun. Unlike electromagnetic radiation, the particles emitted by the Sun (the relatively slow solar wind and the rapid solar cosmic rays) pass through the heliosphere at different speeds. The bulk velocity of the solar wind particles is usually between 200 and 700 km/s with a mode at 400 km/s. On the other hand, the solar cosmic rays are faster and may well reach velocities around 100000 km/s.

Both solar wind and solar cosmic rays contain mostly hydrogen nuclei, but also heavier iron and nickel nuclei. Space probes confirmed the existence of the solar wind and gave a more detailed and definite picture of its composition and other characteristics. Although the solar wind consists mainly of protons and electrons, other constituents like  $^3\text{He}^{++}$ ,  $^4\text{He}^+$ ,  $^4\text{He}^{++}$ ,  $\text{O}^{+5}$ ,  $\text{O}^{+6}$ , and  $\text{O}^{+7}$  have also been observed (Akasofu and Chapman, 1972). Summarised, the most important solar wind plasma characteristics are as follows (Hargreaves, 1992):

- Solar wind blows continuously, velocity on average 400 km/s;
- Energy is more directed than random ( $\Delta E/E \sim 0.01$ );
- Flow is almost radially from the Sun;
- Power flux is about  $10^{-4} \text{ Wm}^{-2}$ ;
- Composition mainly of electrons and protons and electrons, with a few per cent  $\alpha$ -particles and heavy nuclei;
- Particle density within the range  $3\text{-}10 \text{ cm}^{-3}$ , mode at  $5 \text{ particles cm}^{-3}$ ;
- Proton energy about  $\frac{1}{2} \text{ keV}$ ;
- Electron energy about  $\frac{1}{4} \text{ eV}$ ;
- Solar wind is strong and irregular, with periods ranging from minutes to a few hours.

The solar wind exerts pressure continuously against the Earth's magnetic field, sharply delimiting its front (day) side (approximately 60000 km away from Earth) and extending (in a comet-like shape) the magnetosphere up to a million kilometers on the night-side of the Earth.

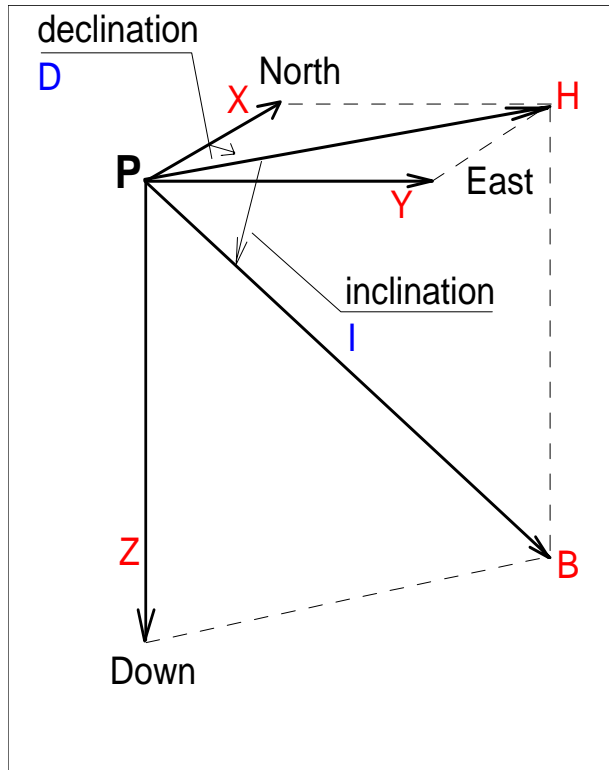
A particular form of the solar wind is the coronal mass ejection (CME), which is much higher in mass and travel much faster (up to three times) than the speed of the solar wind. A CME may contain in addition helium and electrons, all particles held together by the strong CME intrinsic magnetic fields.

As said above, all emissions are continuous, but radiation levels are increased significantly during periods of solar eruptions. Thus, the CMEs can generate strong geomagnetic perturbations in the Earth's magnetic field intensity, on average 12 times per year of high solar activity and 1.3 times at a solar minimum. The charged particles, striking the magnetic field follow the lines of magnetic force down into the atmosphere (especially at high latitudes) causing phenomenae like auroras.



## 2.2 The Earth's magnetic field

The magnetic field of the Earth is a vector field which intensity  $\mathbf{B}$  at an arbitrary point P can be specified in several ways using any three of the following independent components:



$\mathbf{B}$  - total magnetic field intensity;  
 $\mathbf{H}$  - the horizontal vector component of the field intensity  $\mathbf{B}$ ;  
 $\mathbf{X}$  - the northward horizontal component of  $\mathbf{B}$ ;  
 $\mathbf{Y}$  - the eastward horizontal component of  $\mathbf{B}$ ;  
 $\mathbf{Z}$  - vertical component of  $\mathbf{B}$  (positive if downward);  
 $D$  - declination-the deviation of  $\mathbf{H}$  from the northward horizontal direction (positive if eastward);  
 $I$  - inclination (dip) - the deviation of  $\mathbf{B}$  from  $\mathbf{H}$  (positive if downward).

If any three of the above components are available, the rest of them can be determined from the following formulae:

$$B^2 = X^2 + Y^2 + Z^2 = H^2 + Z^2$$

$$H^2 = X^2 + Y^2$$

$$X = H \cdot \cos D$$

$$Y = H \cdot \sin D = X \cdot \tan D$$

$$Z = B \cdot \sin I = H \cdot \tan I$$

$$D = \arctan(Y/X)$$

$$I = \arctan(Z/H)$$

**Fig. 2-1** The geomagnetic force  $\mathbf{B}$ , its rectangular components  $X, Y$ , and  $Z$ , and the elements  $H, D$ , and  $I$ .

Assuming the Earth is a sphere of radius  $a$ , and supposing that no electric currents flow across its surface, the magnetic field will have a potential  $V$  satisfying the Laplace's equation ( $\nabla^2 V = 0$ ). Thus, the potential can be conveniently represented by the following series expansion of spherical harmonics (Chapman and Bartels, 1940):

$$V = a \sum_{n=1}^{\infty} \sum_{m=0}^n P_n^m(\cos \theta) \left\{ \left[ c_n^m \left( \frac{r}{a} \right)^n + \left( 1 - c_n^m \right) \left( \frac{a}{r} \right)^{n+1} \right] A_n^m \cos m\phi + \left[ s_n^m \left( \frac{r}{a} \right)^n + \left( 1 - s_n^m \right) \left( \frac{a}{r} \right)^{n+1} \right] B_n^m \sin m\phi \right\}$$

where  $r, \theta, \phi$  are the spherical polar coordinates,  $P_n^m$  are the associated Legendre polynomials, and  $c_n$  and  $s_n$  are numbers between 0 and 1.

For the study of the ionosphere-plasmasphere system dynamics, the use of geomagnetic (dipole) coordinates and time is much more convenient than the use of geographical ones. Also, the geomagnetic time is very useful when studying magnetic storms, auroras, and other related phenomena. For a point P, having geographic coordinates  $\varphi$  (latitude) and  $\lambda$  (longitude), the corresponding geomagnetic coordinates  $\Phi$  (geom.latitude) and  $\Lambda$  (geom.longitude) are obtained through the following expressions:

$$\sin \Phi = \sin \varphi \cdot \sin \varphi_0 + \cos \varphi \cdot \cos \varphi_0 \cdot \cos(\lambda - \lambda_0)$$

$$\sin \Lambda = \cos \varphi \cdot \sin(\lambda - \lambda_0) / \cos \Phi \quad \text{or} \quad \sin \Lambda = -(\sin \varphi - \sin \varphi_0 \cdot \sin \Phi) / (\cos \varphi_0 \cdot \cos \Phi)$$

where  $\varphi_0$  and  $\lambda_0$  are the geographic latitude and longitude of the geomagnetic pole in the Northern (geographic) hemisphere.

## 2.3 Solar activity and indices

The intensity of the solar emissions varies with times and quantification of the solar activity is therefore required for research purposes.

In 1848 Rudolph Wolf devised a daily method of estimating solar activity by counting the number of individual spots and groups of spots on the face of the sun. Wolf chose to compute his sunspot number by adding 10 times the number of groups to the total count of individual spots, because neither quantity alone completely captured the level of activity. Nowadays, the Wolf sunspot counts continue, since no other index of the sun's activity reaches into the past as far and as continuously. An avid astronomical historian and an unrivaled expert on sunspot lore, Wolf confirmed the existence of a cycle in sunspot numbers. He also more accurately determined the cycle's length to be 11.1 years by using early historical records. Wolf discovered independently the coincidence of the sunspot cycle with disturbances in the earth's magnetic field. Today, an observer computes a daily sunspot number by multiplying the number of groups seen by ten and then adding this product to his total count of individual spots, same way that Wolf did. Many refer to the sunspot number as a Wolf number or count (or as a Zurich Sunspot Number). Results, however, vary greatly, since the measurement strongly depends on observer interpretation and experience and on the stability of the Earth's atmosphere above the observing site. Moreover, the use of Earth as a platform from which to record these numbers contributes to their variability, too, because the sun rotates and the evolving spot groups are distributed unevenly across solar longitudes. To compensate for these limitations, each daily international number is computed as a weighted average of measurements made from a network of cooperating observatories. Sunspot counts rise and fall approximately every 11.1 years. The cycle, though, is not symmetrical, for the spot count takes on the average about 4.8 years to rise from a minimum to a maximum and another 6.2 years to fall to a minimum once again. Also, not all cycles are equally intense. The largest annual mean number (190.2) occurred in 1957 during the 19<sup>th</sup> cycle. Today, much more sophisticated measurements of solar activity are made routinely, but none has the link with the past that sunspot numbers have.

The Sun radiates a thermal radio emission at all times, but the emission greatly intensifies during solar flares (sudden brightening of a small area of the photosphere remaining visible for minutes and even hours) and when active regions are visible. It has been found that the total emission at radio wavelengths is a reliable indicator of the solar activity, particularly the intensity at a wavelength of 10.7 cm, reported in flux units of  $10^{-22} \text{ Wm}^{-2}\text{Hz}^{-1}$ . This quantity is used also as solar activity indicator, named the F10.7 index.

The F10.7 index is conveniently linked to the sunspot number. Correlation studies of the solar irradiance (S) with sunspot number (R) and 10.7 cm flux (F) in flux units determined (Hargreaves, 1992) the following relations:

$$S = 1366.82 + 7.71 \times 10^{-3} R$$

$$S = 1366.27 + 8.98 \times 10^{-3} F$$

Two interesting problems are the approximation and prediction of solar activity based on sunspot number / F10.7 index data. It has been proven (De Meyer, 1981) that the solar activity is rather an hybrid between an harmonic variation and a series of pulses (a sequence of independent and partly overlapping events, triggered periodically at intervals of about 11 years). Therefore, the solar activity cannot be considered as a definite periodic phenomenon subjected to a long-range predictability.

## 2.4 Geomagnetic activity and indices

The level of geomagnetic activity is of key importance for studies dealing with various aspects of the solar-terrestrial relationship including the geomagnetism, atmospheric, ionospheric and magnetospheric physics, climatology, medicine, etc. Since the beginning of continuous recording of the Earth's magnetic field variations, many indices have been devised to monitor its complex perturbations (Menvielle and Berthelier, 1991). Geomagnetic indices have multiple purposes: (i) provide information on the level of the geomagnetic activity via analysing related phenomenae, (ii) help the investigations of the geomagnetic activity itself, (iii) facilitate studies of the geomagnetic activity response to various parameters, such as solar wind and interplanetary magnetic field, etc.

At a given station, the observed geomagnetic field variation is a sum of two major components – secular and transient. The source of the *secular* variation is internal, while the transient variation is due to mainly external sources. Of particular interest for the current study is the *transient* variation which is a signature of the currents taking place in the magnetosphere under the influence of the solar wind. The complexity of the solar wind-magnetosphere-ionosphere system coupling results in currents flowing in the ionosphere and magnetosphere e.g. field-aligned, magnetopause and induced currents. All this leaves its mark on the geomagnetic field at the Earth's surface and differs with the geographic location of the observatory. Therefore, other reasons to introduce indices is to quantify variations due to an isolated effect (e.g. the ring current axis-symmetric variations described by Dst) and also to estimate the global energy input in the magnetosphere (the purpose of the planetary indices, such as Ap and Kp). The transient variations are subdivided into regular and irregular variations. The *regular* variations appear every day and are representative for quiet geomagnetic conditions. They are explained with the ionospheric current system whose position and shape are almost constant in a reference system fixed with respect to the Sun; such systems are called Sq, standing for 'solar quiet' conditions. On the other hand, the *irregular* variations are caused by the magnetospheric energy input and strongly related to the magnetospheric storms. Some of the observed perturbations have global coverage (seen only during daytime), while others are intense at high latitudes and disappear at low latitudes.

Presently, there are two groups of indices that are most widely in use – the K indices and the Dst index. The *K index* takes into the account the morphological characteristics of the transient irregular variations, according to the morphological rules established by Mayaud (1967). A local K index is assigned at the local observatories to each 3-hour interval of GMT time. By definition, the 3-hour K index is the number of the class which corresponds to the larger of the two ranges measured on the horizontal components. The planetary Kp index is based on the range of variation within the 3-hour periods observed in the records from about a dozen selected magnetic observatories. After local weighting and averaging (Menvielle and Berthelier, 1991), the Kp value for each 3 hours of the day is obtained on a scale from 0 ('very quiet') to 9 ('very disturbed'). The scale is quasi-logarithmic and the integer values are subdivided into thirds by use of the symbols + and -, hence for example 3-,3+,4-,4+, etc. Ap is a daily index, derived from the same data, but converted to a linear scale and then averaged over the day. A convenient conversion is  $K_p = 1.739 \ln(0.423 A_p)$ . The *Dst index* gives the average (in longitude) depression of the horizontal component in low latitudes (due to the ring current), which is proportional to the total kinetic energy of the particles injected and trapped in the Van Allen (electron) belt (Akasofu and Chapman, 1972; Rangarajan, 1989). Thus, the Dst index is a quantitative index, strongly related to the magnetospheric parameters and serves as a useful indicator of the intensity and duration of magnetic storms. Although the definition of the index invokes magnetic disturbances, it can be deduced as a continuous function of the universal time.

## 2.5 Geomagnetic and ionospheric storms

The *geomagnetic* storm is defined (Matsushita, 1967; Akasofu and Chapman, 1972; Forster and Jakowski, 2000) as the complex effects (on the geomagnetic field and the terrestrial upper atmosphere) in response to the ‘collision’ of the system of interplanetary shock and solar plasma with the magnetosphere. The solar-wind density, velocity, and intensity of the embedded interplanetary magnetic field are highly variable. Sudden changes in these parameters, associated with abrupt intense emission of X-rays, EUV/UV radiation, and ejection of particles (with energies ranging from 1keV to more than 10Gev) originating from the Sun, result in drastic increase of energy input into the magnetosphere, thus generating a geomagnetic storm. A typical magnetospheric storm consists of three distinct phases. First is the *shock* phase, when interplanetary shock wave reaches the magnetosphere and severely compresses it. Next, a relatively calm period (lasting from 10 min up to 6 hours) follows, named *initial* phase. Finally, the *main* phase takes place, which begins at about the time when the shock-driving plasma reaches the magnetosphere. The main phase is characterised by a succession of explosive processes, called magnetospheric substorms. The level of geomagnetic activity, including storm conditions are described with Kp in the following manner: 0-2 (quiet), 3 (unsettled), 4 (active), 5 (minor), 6 (major), 7-9 (severe storm) conditions. The existence of a magnetic storm and its level of intensity (class) are defined by the Dst index in the following way. Storm conditions prevail whenever  $Dst < -50[nT]$ . A class II storm is defined for conditions with  $-100[nT] < Dst < -50[nT]$  for at least four hours. A class I storm is defined for conditions with  $Dst < -100[nT]$ . A geomagnetic storm begins either gradually or with an abrupt change named ‘sudden commencement’ (SSC or SC). Generally, a geomagnetic storm develops through initial, main, and recovery phases. The main phase of the storm begins at the time when the horizontal variation field of the Dst component, Dst(H), rapidly decreases lower than the pre-SC level and ends when Dst(H) reaches the maximum decrease. The initial and recovery phases are before and after the main phase; however, sometimes these phases are not easily identified in a storm.

The *ionospheric* storm is defined as the broad spectrum of strong ionospheric disturbances resulting from the start and development of a geomagnetic storm. The perturbations exceed the median variability and manifest complex behaviour depending on the spatial location and season. The F-region response is easily detected from ionosonde observations of NmF2 and HmF2 and the total electron content (TEC) measured by trans-ionospheric propagation techniques. Similarly to the magnetic storms, the ionospheric storm goes through an initial (positive) phase (lasting a few hours but occasionally brief or even missing) when the electron density and the electron content are greater than the ‘normal’ median values. This is followed by the main (negative) phase when the above quantities are reduced below their normal pre-event values. The negative phase often lasts for several days and during this period the ionosphere gradually returns (recovers) to its normal behaviour.

Greatest storm effects are observed at high and middle latitudes. Many statistical studies (Hargreaves, 1992; Proelss, 1993; Szuszczewicz et al., 1998; Forster and Jakowski, 2000) suggests that the magnitude and sign of effect depends on the time of day. The negative phase tends to be weaker in the afternoon and evening, stronger in the night and morning. Positive phases are often missing at stations being in the night sector at commencement. Seasonal and hemispheric effects are also remarkable. In the summer hemisphere, the negative phase is comparatively stronger and the positive phase is weaker. This holds true for both northern and southern hemispheres, however the inner-hemispheric difference is such that NmF2 is actually increased during the main phase of storms occurring in the southern winter. The hemispheric differences are explained with the larger separation between the geographic and geomagnetic poles in the south (Hargreaves, 1992).

## 2.6 Thermosphere-ionosphere system coupling

There are several aspects of the thermosphere-ionosphere coupling that should be considered when investigating the system response to geomagnetic activity. Under quiet solar/geomagnetic activity conditions, the ionosphere plasma is imbedded in a background neutral gas whose density dominates the electron-ion density by several orders of magnitudes. Thus, the neutral atmosphere forms the dominating background for the ionisation process particularly at lower altitudes below the F2-layer height. While the ionisation theory is generally clear for quiet conditions, the importance of the thermosphere composition and dynamics under storm conditions is not yet fully understood despite the decades-long research. If the densities of the major neutral constituents ( $N_2$ ,  $O_2$ ,  $O$ ,  $H$ ,  $He$ ) and the neutral gas temperature are known globally, the other parameters (like pressure gradients) of the neutral atmosphere are easily deductible. The pressure gradients, in particular, constitute the main driving force of the thermosphere wind system. At a given location, the horizontal wind system may act as a source or a sink for the neutral gas density, thus disturbing the barometric equilibrium and originating a vertical re-distribution (velocity) so the total divergence is reduced. At heights about 110 km the vertical motions are described as molecular diffusion; below this altitude – as turbulent (eddy) diffusion. Since different gaseous components have different vertical velocities, the net effect results in a change of the neutral atmosphere composition.

There is no doubt about the significance of the thermosphere composition for the thermosphere-ionosphere coupling. In the F2 region for example, the  $O^+$  density is the major ion. An increase in the parent  $O$  density causes an increase in the  $O^+$  production and a decrease in the downward diffusion velocity. Alternatively, an increase in the  $N_2$  and/or  $O_2$  concentration produces conditions for increased chemical loss of  $O^+$ , which in turn leads to a decrease in the  $O^+$  density in the region. A well-known fact is also that variations in the neutral gas particle densities may induce strong variations in the ion densities and electron temperatures, particularly if the  $O$  density variations are opposite to that of  $N_2$  and  $O_2$  densities.

Particular attention needs also the  $[O] / [N_2]$  density ratio. Its role for the manifestation of the negative storm phase, i.e. the electron density depletion, is well explained and generally accepted (Proelss, 1980; Proelss, 1995). It is the role of above ratio for the positive storm effects that is debatable. Some authors (Rishbeth et al., 1987; Fuller-Rowell et al., 1991; Field et al., 1998) explain the positive effect with the enhancement of the ratio, while others suggest that the effect is rather due to the dynamic nature of the thermosphere through neutral winds and electric currents. The quiet-time global thermospheric wind system is driven mainly by the solar heating and is thus stationary with respect to the Sun. During storms however, the sudden energy input into the polar regions leads to generation of strong perturbations propagating towards the equator resulting in ion density increase during daytime and effective maintenance of the F-region plasma during nighttime, thus explaining the positive storm effects (Jones and Rishbeth, 1971; Namgaladze et al., 2000; Foerster and Jakowski, 2000).

Other important phenomena are the ‘atmospheric dynamo’ (situated in the ionospheric E-region) and the ‘magnetospheric dynamo’ (taking place near the magnetopause and magnetospheric tail). The disturbed wind pattern during geomagnetic storms at the heights of the atmospheric dynamo (~105km) can lead to disturbance dynamo electric fields which in turn influence the plasma density and dynamics (Fejer, 1997). The magnetospheric dynamo is subjected to abrupt changes during storms. Thus, during relatively brief periods (of the order of approximately 1 hour), the magnetospheric electric fields penetrate deeply into the plasmasphere. A rapid increase of the dawn-dusk electric field induces an eastward directed field on the dayside hemisphere and westward field on the nightside (Foerster and Jakowski, 2000).

## 2.7 **Ionosphere-Plasmasphere system coupling**

Thermal plasma fluxes along the geomagnetic field lines are the energy and mass exchange carriers between the ionosphere and plasmasphere. There are three major mechanisms responsible for the ionosphere-plasmasphere coupling – the ionospheric influx/outflux, the interhemispheric fluxes, and plasmaspheric fluxes resulting from zonal electric fields.

The ionospheric outflux (the ion flux directed upward out of the ionosphere) is typical for the day-time hours. For example, a regular (under normal conditions) mid-latitude outflux is of the order of  $1-4 \times 10^8 [\text{cm}^{-2}\text{s}^{-1}]$ . A significant enhancement (up to  $1-2 \times 10^9 [\text{cm}^{-2}\text{s}^{-1}]$ ) of the outflux is reported for periods of increased solar/geomagnetic activity (Buonsanto et al., 1992).

The inter-hemispheric plasma exchange is also important. Such flows contribute to the post-storm flux-tube refilling (Horwitz et al., 1990), to the Nighttime Winter Anomaly of higher plasma densities in winter than in summer (Jakowski and Foerster, 1995), etc.

Plasma fluxes may also occur as a result of zonal disturbance electric fields (Mikhailov and Foerster, 1999). Westward electric fields push plasma from higher to lower L-shells with smaller tube volumes. In this way, the plasma pressure in the flux tube is increased, causing an enhanced plasma flux from the protonosphere down to the regions of the F-layer. Oppositely, the eastward electric field leads to plasma decompression in the tube, resulting in a significantly decreased plasmaspheric flow to the F-region.

### 3. MEASUREMENTS

Since the beginning of the twentieth century, various methods of investigating the thermosphere-ionosphere-plasmasphere system have been developed. These methods can be classified in the following major categories:

- vertical incidence sounding technique (ionosonde)
- ground-based measurements of the columnar electron content
- incoherent scatter radar technique
- satellite and rocket in-situ measurements
- remote sounding technique (e.g. the GPS occultation experiments)
- radio imaging technique (e.g. the magnetospheric imaging experiment)
- mathematical modelling

However, no single observational or simulating tool alone proved to adequately represent the physical processes in their complexities.

The Royal Meteorological Institute (RMI) Geophysics Centre at Dourbes (4.6°E, 50.1°N) is a complex observational site consisting of several observatories – ionosphere sounding, atmospheric, geomagnetic, cosmic rays, GPS TEC, etc., all connected with optical-fibre communication lines (Fig.3-1). A fast link allows to communicate with the RMI in Brussels, the Royal Observatory of Belgium (ROB) and the Belgian Institute for Space Aeronomy (BISA). Some information is shared and available via the world-wide web (WWW). First measurements at Dourbes started more than half a century ago and a vast amount of data have been accumulated during the years.

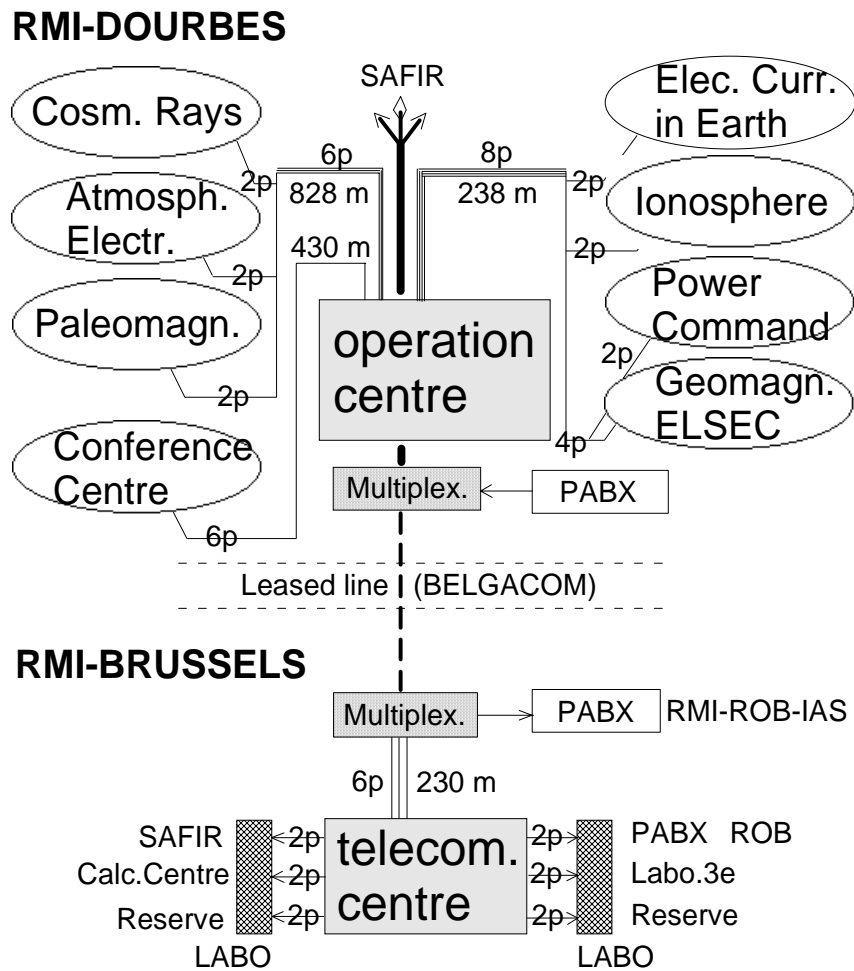


**Fig.3-1** The RMI measurement and communication network.  
 SAFIR – Thunderstorm alert system using radio interferometry.  
 A 2p connection consists of two cables with two optic fibres in each cable.



### 3.1 Vertical incidence sounding of the ionosphere

The vertical ionospheric sounding is still one of the most important observational techniques (Hargreaves, 1992; Dieminger et al., 1995). Low and high-frequency radio waves are transmitted upward and reflected in the ionosphere at the height where the refractive index becomes zero for vertical incidence, or  $\sin\varphi_0$ , where  $\varphi_0$  is the incidence angle. The standard piece of equipment is called ionospheric sounder (ionosonde), in which a transmitter and a receiver are swept synchronously in frequency, and the propagation time  $t_g$  (or the corresponding virtual height  $h' = 0.5ct_g$ ,  $c$ -speed of light) of the reflected signal recorded for each of the transmitted frequencies. The resulting ionogram represents the ionospheric echo time delay as a function of the radio frequency, which ionogram can be interpreted also as a profile of electron density ( $N_e$ ) against altitude. The electron density is deduced from the plasma frequency ( $f_p$ ) using the formula  $(f_p[\text{kHz}])^2 = 80.5N_e[\text{cm}^{-2}]$ .

The original sounding method has been improved during the years: digitisation was introduced; strength of the echo can be measured as well; with precise timing the transmitter and the receiver can be separated and thus sounding performed over oblique paths; topside sounders were developed thus allowing probing the ionosphere from above; etc.

The ionospheric soundings are carried out by a digital sounder (DGS-256) developed by the University of Massachusetts Lowell and featuring the operational characteristics given in Table 3-1. A DGS-256 ionogram is plotted in Fig.3-2.

The DGS-256 ionosonde automatically calculates the electron density profile assuming a model valley and outputs the coefficients of a Chebyshev polynomials expansion. It is very important because it provides opportunity for comparison of the ionosonde TEC (computed using ionosonde measurements) with the GPS TEC (derived from GPS observations).

<i>Operational Parameter</i>	<i>Range</i>	<i>ionogram settings for DB049</i>
frequency range	0.5 - 30 [MHz]	1-16
frequency scale	linear or logarithmic	linear
frequency steps	5, 10, 25, 50, 100, 200 [kHz]	100 [kHz]
range resolution	2.5, 5.0, 10.0 [km]	5.0 [km]
number of range pixels	128, 256	128
range start	selectable	60 [km]
pulse repetition range	50, 100, 200 [ $s^{-1}$ ]	100 [ $s^{-1}$ ]
pulse width	66, 133 [ $\mu s$ ]	66 [ $\mu s$ ]
transmitter RF power	$\leq 10$ [kW]	5 [kW]
duration of ionogram	selectable	4 [min]
phase code	interpulse pseudo-random biphas coding	
digitization	12 bit linear	
amplitude resolution	0.25 [dB]	
phase resolution	1.4°	
Doppler resolution	4 [Hz] or 12 [Hz]	4 [Hz]
wave polarization	O/X	
data display	video and paper	
data storage	disk, cartridge	

**Table 3-1** The Dourbes Ionosonde (DB049) – operational parameters and settings.  
After B.W.Reinisch (Dieminger et al., 1995).

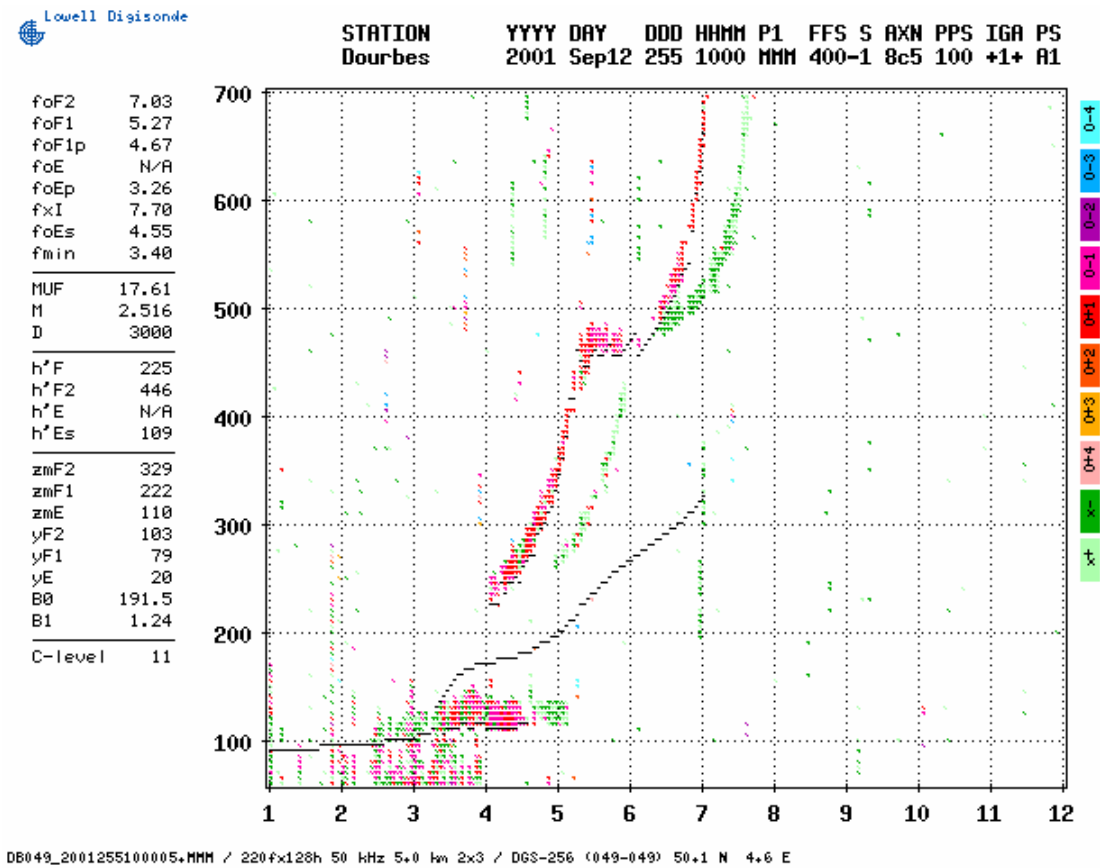


**Fig.3-2** The DGS-256 ionogram recorded at 10:00UT on 12/09/2001 at the RMI-Dourbes Centre.

### 3.2 GPS-based Total Electron Content measurements

The era of total electron content (TEC) measurements using very high frequency signals from geostationary satellites (height about 36000km) is essentially over. Such observations provide good time resolution, but the geographical coverage is limited by the small number of receiving stations. Another type of TEC measurements, based on the low-altitude polar orbiting satellites from the Navy Navigation Satellite System, provide good latitude coverage but have problems with the absolute calibration and give the content only up to the altitude of approximately 1100 km.

The best research opportunities so far offers the Global Positioning System (GPS) using dual-frequency transmissions. Important advantages of this type of observations are (Davies and Hartmann, 1997):

- Operational global coverage available: e.g. using the International GPS Geodynamics Service (IGS) geodetic network;
- Cost efficient measurements: radio signals are continuously provided and receivers are commercially available;
- Electron content measured up to a great height (of more than 20000km), thus providing valuable information on the topside electron content of the ionosphere and plasmasphere;
- Sufficiently high frequencies are used, so that ionospheric absorption and effects of the geomagnetic field on the radio signals are small;

At the RMI - Dourbes Geophysics centre, a GPS receiver is collocated with the digital ionosonde. Using the GPS signals on two coherent carrier frequencies ( $L_1/L_2 = 1575.42/1227.6$ [MHz]), the TEC computation procedure (Warnant, 1996) is based on the 'geometry-free' combinations of GPS code ( $P_{p,GF}^i$ ) and phase ( $F_{p,GF}^i$ ) measurements:

$$P_{p,GF}^i = P_{p,L1}^i - P_{p,L2}^i, \quad F_{p,GF}^i = F_{p,L1}^i - (f_{L1} / f_{L2}) F_{p,L2}^i$$

where  $P_p^i$  is the code measurement made by receiver  $p$  on  $i$ -th satellite,  $F_p^i$  is the carrier phase measurement made by receiver  $p$  on the  $i$ -th satellite, and  $f_{L1}, f_{L2}$  – the frequencies on the L1,L2 carriers respectively. Rewritten as functions of TEC, the above equations read:

$$P_{p,GF}^i = -1.05 \times 10^{-17} TEC_p^i + (D_p - D^i) \quad (3.1)$$

$$P_{p,GF}^i - \lambda_{L1} F_{p,GF}^i = (D_p - D^i) - \lambda_{L1} N_{p,GF}^i \quad (3.2)$$

where  $N_p^i$  is the phase ambiguity,  $TEC_p^i$  is the slant electron content (along the  $i$ -th satellite raypath) in TECU,  $D^i, D_p$  are the  $i$ -th satellite and receiver  $p$  differential group delays. The ambiguity is eliminated by the following combination of 'geometry-free' code and phase measurements:

$$P_{p,GF}^i - \lambda_{L1} F_{p,GF}^i = (D_p - D^i) - \lambda_{L1} N_{p,GF}^i$$

where  $\lambda_{L1}$  is the L1 carrier wavelength. The formula requires the estimation of the receiver and satellite group delays, which estimation is obtained from Eq.(3.1) after modelling TEC by means of a simple polynomial depending on latitude and local time. The conversion to vertical TEC is performed by assuming that the ionosphere is a layer of infinitesimal thickness located at a 'mean ionospheric' height of 350 km and using simple cosine function of the zenith angle at the 'ionospheric point' (the point on the raypath at the mean ionospheric height). Finally, the TEC value is calculated from Eq.(3.2).

The RMI - Dourbes Geophysics Centre is capable of producing high-quality GPS TEC values every 15 minutes. Measurements have been conducted regularly since July 1994 and a large TEC database has been created for the best part of the current solar-activity cycle.

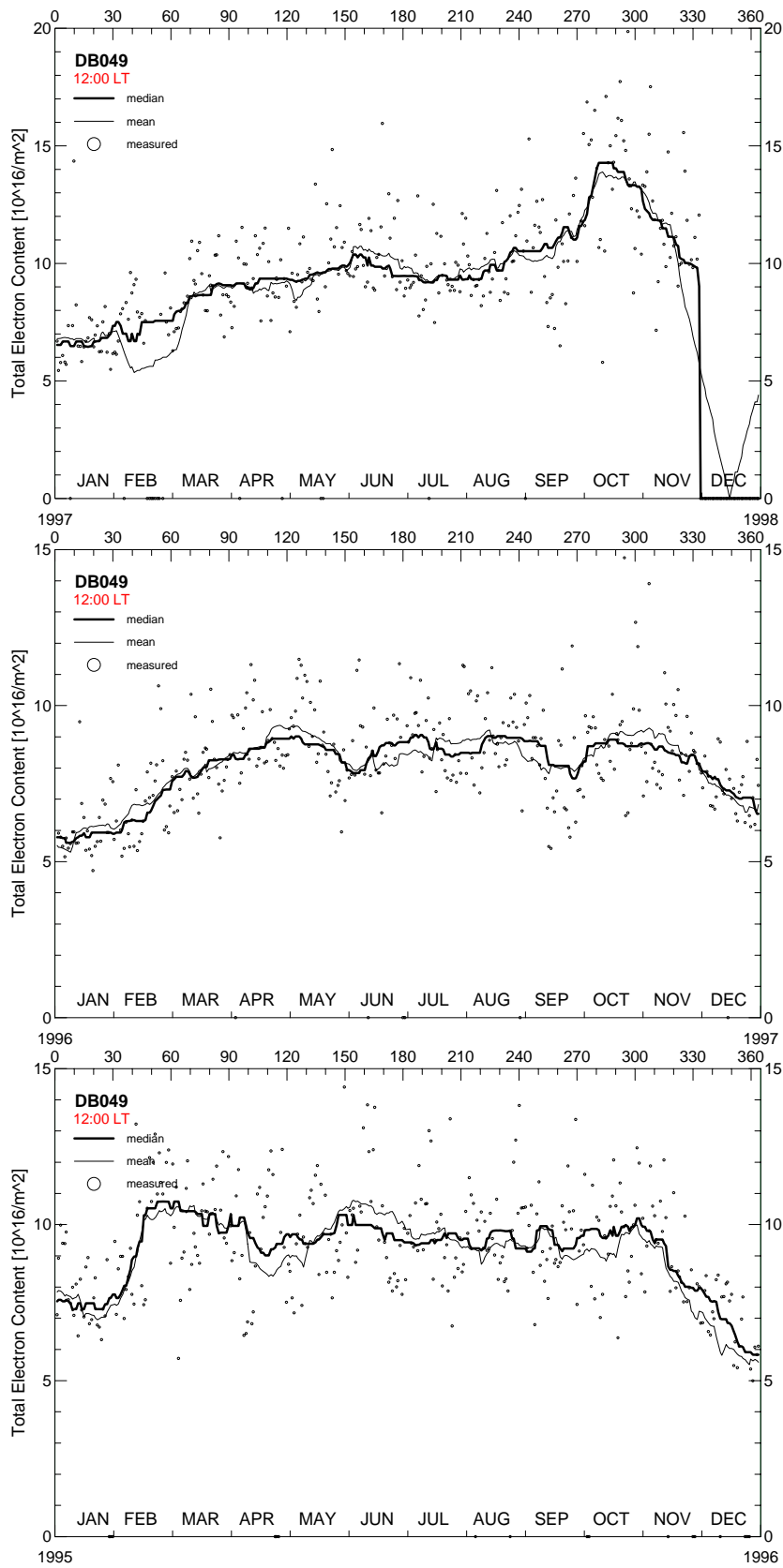


**Fig. 3-3A** Daytime (12:00LT) GPS-based TEC measurements for Dourbes (4.6°E,50.1°N).

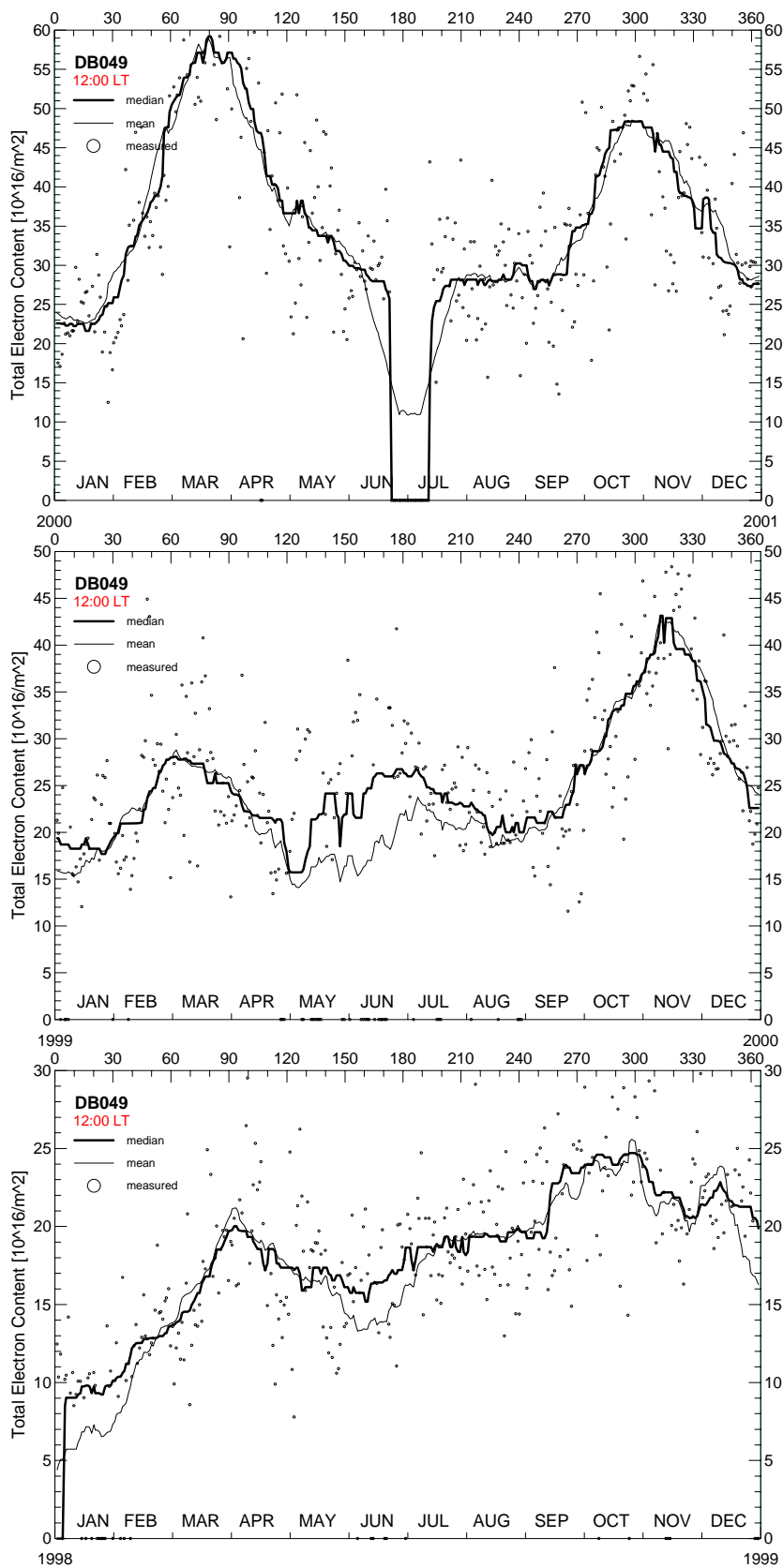


**Fig. 3-3B** Daytime (12:00LT) GPS-based TEC measurements for Dourbes (4.6°E,50.1°N).

### 3.3 Geomagnetic observations

From the beginning, the best measurements of the geomagnetic induction was the goal of the designers. The observatory building was erected without any ferromagnetic material even for the external painting. Double-core fluxgate magnetometers are used for measurements. This type of magnetometers are robust, have reliable electronics, and are capable of recording not only the field variations but its full strength as well.

The main idea behind a standard fluxgate magnetometer (**Fig.3-4**) is to analyse the signal coming from a sensor utilising non-linear magnetization properties of magnetic materials with high permeability. The fluxgate sensor consists of three parts– a bar core and two windings around it. The core is made of saturable material of high permeability (e.g. ferrite, permalloy, etc.). The first winding (excitation coil) is fed with alternating current (having frequency  $f$ ), so that saturation occurs. The second winding (pick-up coil) envelopes both the core and the excitation coil. If an external field exists, a signal is generated in the pick-up coil, having not only the frequency  $f$ , but other harmonics too. The second-order harmonic is sensitive to the field intensity and this fact can be used for measurements. It is possible to construct double-bar and ring-core fluxgate sensors. In the double-core sensor, the excitation coils are serially connected and oppositely (antiphase) excited; ring-current sensors are generalisation of the double-core sensors. The excitation of the sensor is produced by an oscillator. The output signal from the pick-up coil is amplified and passed to a phase-sensitive detector (PSD) referenced to the second harmonic of the excitation frequency. After low-pass filtering, a current (proportional to the output voltage) is fed back to the pick-up coil to oppose the detected field.

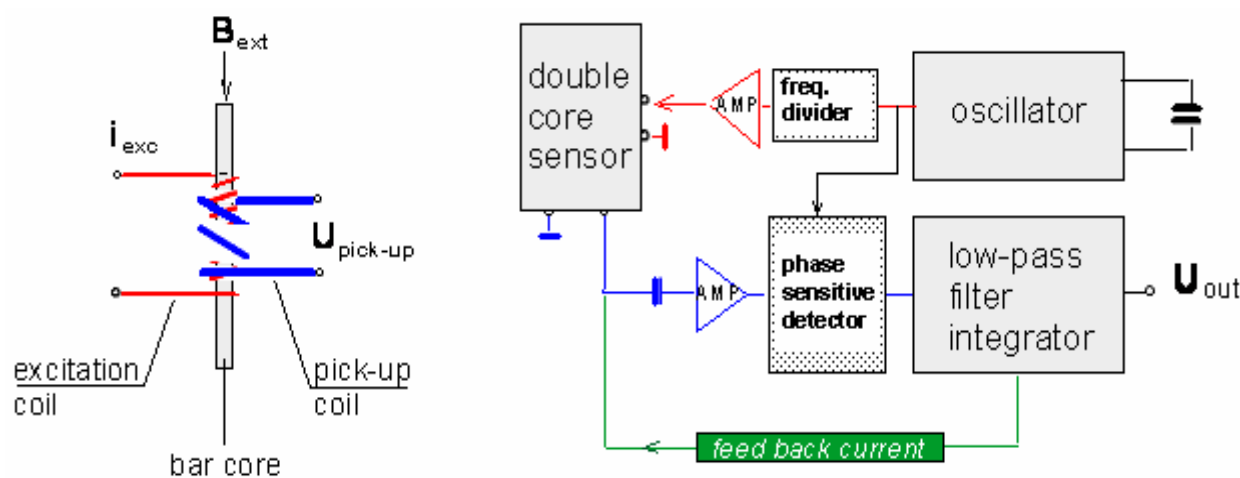


**Fig 3-4** Single-core sensor (left) and a block diagram of a fluxgate magnetometer with feedback (right).  
After Jankowski and Sucksdorff (1996).

Absolute declination, inclination and induction values are manually determined with Theodolite Diflux and Overhauser protons magnetometer respectively. Optical pumping Cesium magnetometer provides data each second. The precision level is of 0.1[nT] for the induction and of  $0.001^\circ$  for the angles. Data are sent each hour to the METEOSAT satellite in the INTERMAGNET format. The large data bank on magnetic support started in 1957. A team uses also cryogenic magnetometers in order to make Paleo- and Archeo-magnetic studies.

The horizontal component is deduced from measurements of the total field ( $B$ ) and inclination ( $I$ ), and their trigonometric relation  $H = B \cdot \cos I$ .

Local magnetic observations can be very helpful in many aspects. One particular advantage, concerning the present study, is the opportunity for near real-time detection of geomagnetic storm onset. Such detection can be performed by identifying the SSC using observations of the geomagnetic field's horizontal component variations. The apparent shape of SSC(H) is not a simple increase but rather manifests some variety. Morphological SSC studies (Matsushita, 1967) reveal that the shape of SSC(H) depends on local time and latitude, and can be sorted in the following major types: (i) a small negative impulse preceding the main positive impulse (such as the one observed at 06:50 in **Fig 3-5**); (ii) a main positive impulse alone; (iii) an increase (lasting up to about six minutes) followed by a decrease to a level lower than the initial pre-SSC level. However, the SSC detection is not always easy, particularly when performed on a real-time basis. A similar abrupt disturbance without succeeding large changes, called 'sudden impulse', can be mistaken for a SSC.

The SSC and the initial phase of a geomagnetic storm are caused by a compression exerted on the sunlit side of the magnetosphere by a the plasma cloud ejected from the Sun during a solar flare. Interesting phenomena accompanying the SSC are the sudden increases of cosmic noise absorption, bursts of bremsstrahlung X rays, and commencements of geomagnetic micropulsations and ionospheric oscillations. On the one hand, such phenomena indicate that SSC is not simply due to distortion of the magnetosphere, but is also due to hydromagnetic waves and charged particles incoming toward the ionosphere. On the variety of associated phenomena prove the importance of various-type observations of the geomagnetic disturbances.

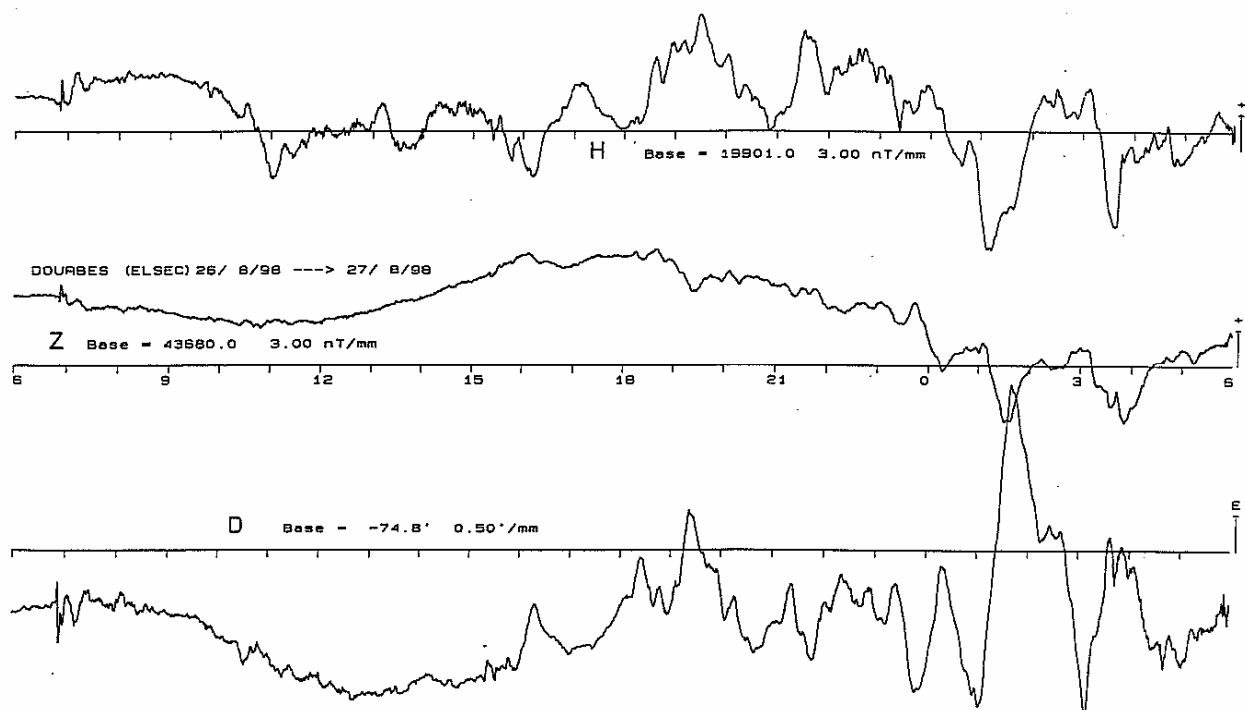


**Fig 3-5** The ELSEC magnetogram recorded at the Dourbes Geophysics Centre on 26/8/1998. The variations of the horizontal component (H) are given on the top, the vertical component (Z) is in the middle, and the declination (D) is provided at the bottom.

### 3.4 Cosmic rays

The interplanetary space is continuously traversed by very energetic nuclear particles called cosmic rays (Akasofu and Chapman, 1972). The origin of the cosmic rays is not definitely determined. Some certainly originate from the Sun and other stars but others are believed to be associated with various energetic processes in the galaxy. Cosmic rays consist mostly of protons (~94%) and helium nuclei (~5.5%), with few nuclei of heavier elements (galactic component of the cosmic rays).

The particles have a broad energy range, from less than 1 GeV ( $10^9$ eV) to more than  $10^{11}$  GeV ( $10^{20}$ eV). In interplanetary space, the cosmic ray flux is in the order of  $0.6 \text{ particles cm}^{-2}\text{s}^{-1}$ , the energy flux is  $5 \text{ GeV cm}^{-2}\text{s}^{-1}$ , and the space density – approximately  $0.8 \times 10^{-10} \text{ particles cm}^{-3}$ .

Over the vast distances of interstellar space, galactic cosmic rays are accelerated to speeds approaching that of light. Since the velocity of galactic cosmic rays approaches the speed of light, the mass of the particles rises sharply with their velocity. In accordance with Einstein's relation between energy and mass, the energy of the particle thus also increases. The high energy of galactic cosmic rays means that they also have a very high penetrating power for many kinds of materials.

Another important aspect of the cosmic rays are the secondary cosmic rays. Near the Earth the motion of the cosmic rays is influenced by the geomagnetic field. When penetrating deep into the atmosphere, the cosmic rays collide with the atmospheric constituents. Protons with energies of about 0.1 GeV isotropically scatter the products of the collisions, such as protons,  $\alpha$ -particles, and neutrons. The paths of these products appear as radial lines from the collision point, forming a 'star'. If the energy of the protons is of higher order (several GeV), then  $\pi$  mesons (types  $\pi^0$ ,  $\pi^-$ ,  $\pi^+$ ) are also produced, which are scattered forward and their paths appear as a 'shower'. When the energy of the incident protons is more than  $10^3$  GeV, the products are scattered into a very narrow cone called a 'jet'. The produced protons collide with new atmospheric particles producing similar reactions. The  $\pi^-$  and  $\pi^+$  mesons decay into muons ( $\mu$ ) and neutrinos ( $\nu$ ), while  $\pi^0$  decay into  $\gamma$  rays, which further decay into electron pairs ( $e^+$ ,  $e^-$ ) emitting bremsstrahlung rays, and so on. The generated many new rays/particles permeate the atmosphere and can reach even the ground level. If protective measures are not taken, they can be a considerable hazard to the aircraft/rocket crews. Curiously, the number of the above product particles at 10-12 km is about 1000 times greater than at an altitude of 25 km.

Interesting phenomenon is the observed eleven-year cycle variation of the cosmic rays. Because the solar activity varies significantly during the sunspot cycle, it is reasonable to expect that the interplanetary irregularities will also vary during the cycle, affecting the lower-energy cosmic rays much more than the higher-energy ones. Forbush showed that the cosmic ray intensity varies regularly and inversely to the sunspot cycle, with the ray flux most pronouncedly decreased at high solar activity.

At the RMI Geophysics Centre at Dourbes, a 9NM-64 neutrons monitor provides measurements of the secondary neutron component of the cosmic rays on the ground. After pressure correction this component follows faithfully the primary cosmic rays intensity. One could detect the proton events above the site (due to energetic solar flares) and the Forbush decreases (due to the occurrences of strong solar winds). A large data bank of the hourly intensities exists since 1967.



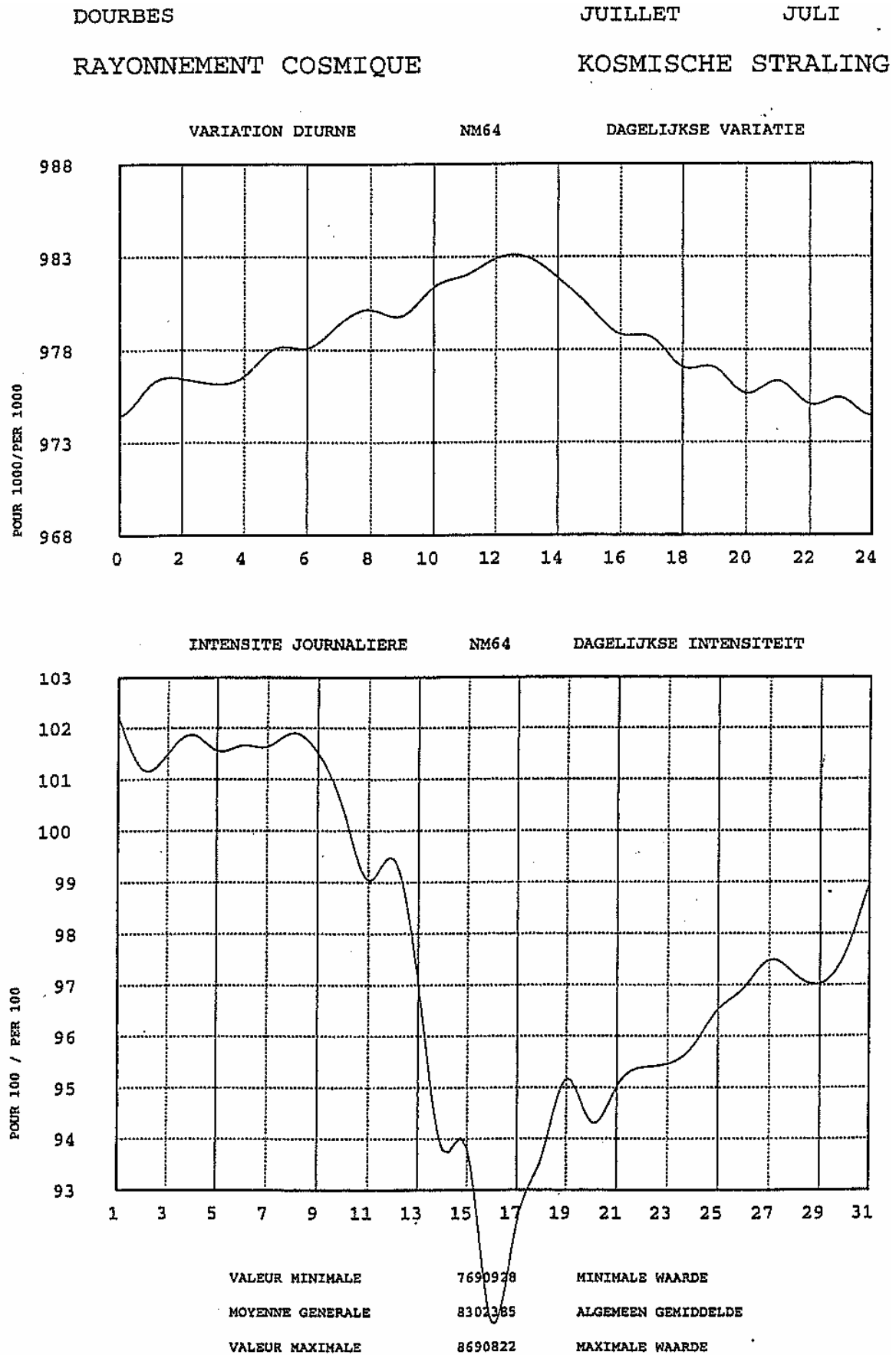


**Fig 3-6** The cosmic-ray measurements recorded at the Dourbes Geophysics Centre in July 2000.

*This page intentionally left blank.*

## 4. CASE STUDIES OF STORMS

In a broad sense, the ‘ionospheric storm’ is defined as the whole spectrum of disturbances that appear in the ionosphere immediately following a geomagnetic storm commencement (Dieminger et al., 1995). The mechanisms accounting for the storm effects are the composition changes, neutral winds, electric fields, etc. The individual event studies of the geomagnetic storms and their effect on the ionosphere-plasmasphere behaviour is regarded as a powerful instrument deepening our understanding of the inter-related processes of energy and momentum transfer and couplings in the solar-terrestrial system. During ionospheric storms the ionospheric processes are intensified and a phenomenon, normally occurring over a long period, is experienced (observed) during relatively short time period.

There are two major topics of interest in the ionospheric storm studies – the neutral winds effect on the ionosphere and electro-dynamic mechanism (Dieminger et al., 1995).

The global manifestation of the neutral wind effect starts at high latitudes where the perturbations in the interplanetary medium and the magnetosphere yield increased energetic particle precipitation, convection electric fields and associated Joule heating. The Joule heating raises the temperature of the thermosphere at auroral latitudes resulting in enhanced equatorward winds and traveling ionospheric disturbances in all local time sectors. On the night-side the pole-to-equator wind field is enhanced. On the day-side, the equatorward wind counteract (and often overpower) the solar-driven poleward winds. As a result, the day-time F-region experiences upward motion due to increased  $([N_2]+[O_2])/[O]$  density ratio. This contributes to the observed ‘positive phase’ usually observed on the first day of the storm.

The large-scale structure of the Earth's plasma environment is determined by electrodynamic processes of magnetospheric and solar wind origin. For example, the electrodynamic drift can redistribute plasma to regions of either high or low chemical loss. Moreover, the  $\mathbf{E} \times \mathbf{B}$  effect of the electric fields mapped down the geomagnetic field lines during storms is instantaneous. Unanswered questions are: the exact interplay of processes during the positive phase, the degree to which magnetospheric convection effect can penetrate to midlatitudes, coupling of atmospheric regions and processes, etc.

Geomagnetic storms and their effects on the ionosphere-plasmasphere system are predominantly investigated using magnetic, ionosonde, and GPS-based measurements, which are all available at the RMI-Dourbes Geophysics Centre.

The geomagnetic activity characterisation is based on a daily evaluation of the geomagnetic disturbances with three major sets of indices in use (Chapters 1 and 2). First, the K indices, which are calculated at all latitudes but proved to be appropriate mainly at sub-auroral latitudes. Second, the Dst index, calculated at low latitudes, which describes the ring current behaviour. Third, the AU, AL, AE indices, calculated at auroral latitudes, providing information on the maxima of the auroral electrojet intensity. For the purpose of this study, the first two indices will be used.

The ionosonde measurements still remain the most reliable and wide-spread type of measurements. For storm studies, very important are not only the critical frequency ( $f_oF_2$ ) measurements but the peak density ( $N_mF_2$ ) itself, the peak height value ( $h_mF_2$ ), the propagation factor  $M(3000)F_2$ , and also the F1- and E-layers characteristics. Some of the reasons are:

- The  $f_oF_2$  values respond quickly to the storm, and together with TEC measurements can provide a crucial information on the slab thickness.
- The  $N_mF_2$  values will be used for calculating the slab thickness  $\tau$ , where  $\tau[\text{km}] = 806.405 \text{TEC}[10^{16} \text{m}^{-2}] / f_oF_2^2[\text{MHz}]$ . This parameter can provide vital information on the dynamic forces such as thermospheric winds and electromagnetic drifts, all playing important roles during the ionospheric disturbance periods.
- The  $h_mF_2$  will give more information on the profile and the F2 layer respond to the storm, particularly in connection to the uplifting process.

No storm studies seem possible nowadays without the TEC value, especially with the introduction of the GPS system providing excellent opportunities for continuous high resolution temporal and spatial observations on a global scale. While there are still problems regarding equipment calibration, they can be overcome, to finally provide accuracy of 2-3 TEC units and relative changes detectable to 0.01 TEC unit levels.

Here, the TEC measurements are used together with the RMI-Dourbes local ionosonde and geomagnetic measurements. It is interesting also to compare the total electron content with the slab thickness because both have absolutely different meaning. To enhance the observed storm-time perturbations, it is sometimes useful to work with the relative deviations of TEC in reference to its 'typical' behaviour. It has been found that, for the reference curve, the TEC median value is preferable to the mean value.

Three are the most important periodicities in storm occurrence. First, there is a 27-day periodicity due to the Sun's rotation period. Second, there is a 6-month periodicity because the magnetic storms are much more frequent during equinoxes. Third, there is an 11-year periodicity as the frequency of the storms follows the sunspot cycle. Annual periodicity is also reported but it has a different morphology (Parkinson and Hutton, 1989).

Three major storms are investigated in detail – the storms on 10 January 1997, 15-17 July 2000, and 31 March – 2 April 2001. The study is focused on the most important questions in the storm research and on the opportunities offered by the comprehensive database of the RMI-Dourbes Centre.

## 4.1 The storm on 10 January 1997

The first geomagnetic storm presented here is that on 10 January 1997. It has been well documented on a global scale because of the pre-observed and announced large coronal mass ejection on 6 January 1997.

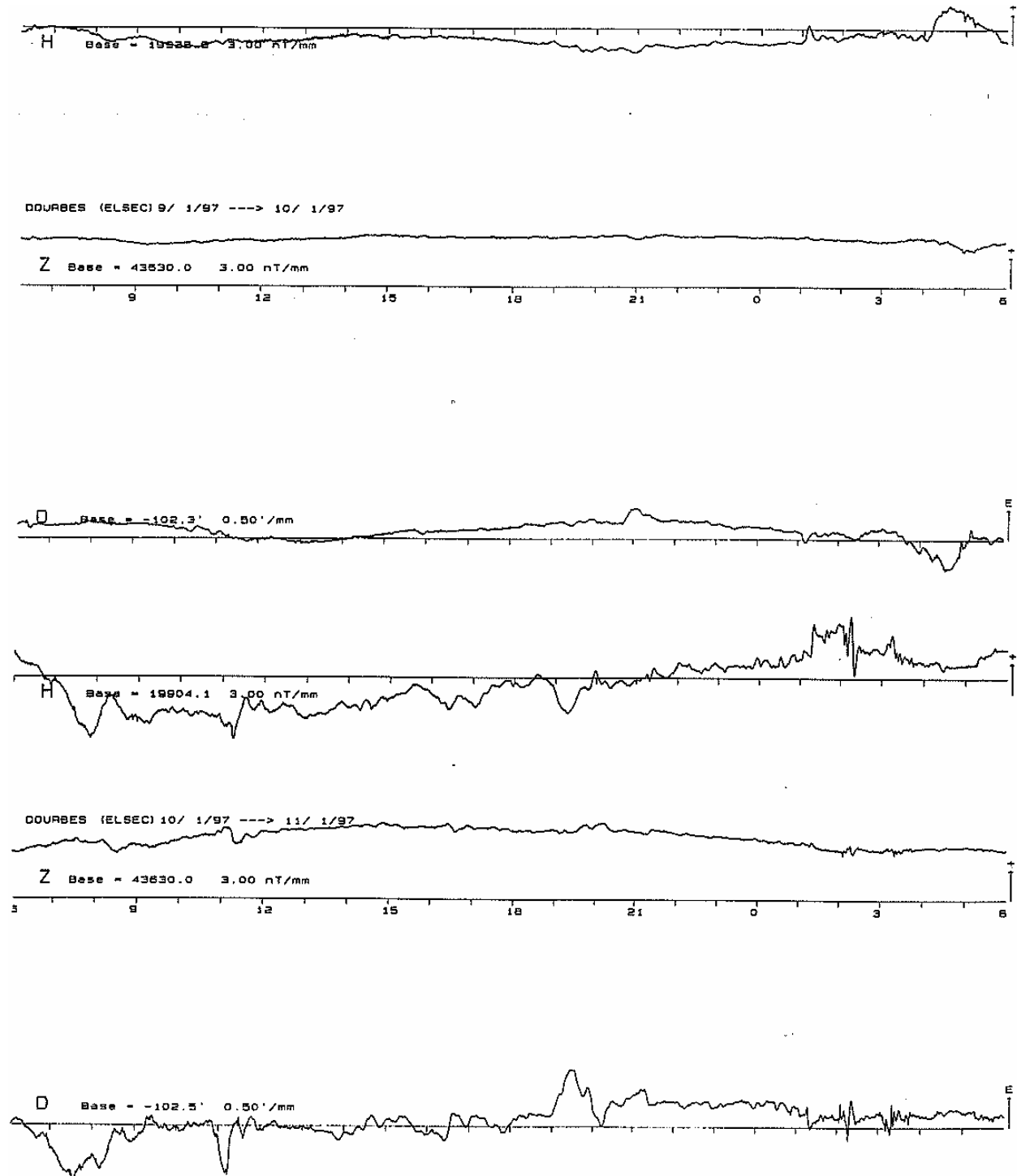


Fig.4-1 The ELSEC magnetogram at the Dourbes Geophysics Centre during 10-11/01/1997 geomagnetic storm.

This storm is characterised by a pronounced positive response from both TEC and foF2 parameters. The noon TEC values are more than 100% higher than the monthly median (Fig.4-2C). Several aspects of the ionospheric response can be investigated from Dourbes and it will be demonstrated on this particular storm. The basic storm features are summarised in Table 4-1 .

<i>Feature</i>	<i>Value</i>	<i>Comments</i>
<i>Storm onset (SSC)</i>	01:00 UT	01:00 UT , 10/01/1997
<i>Dst (min)</i>	-78 nT	09:00 UT , 10/01/1997
<i>Total storm period ( Dst ≤ -50nT )</i>	10 h	08:00UT (10/1/1997) – 17:00UT (10/1/1997)
<i>Initial plus main phase ( SSC → Dst(min) )</i>	8 h	01:00UT (10/1/1997) – 09:00UT (10/1/1997)
<i>Main phase ( -50 nT → Dst(min) )</i>	1 h	08:00UT (10/1/1997) – 09:00UT (10/1/1997)
<i>Recovery phase ( Dst(min) → -50 nT )</i>	9 h	09:00UT (10/1/1997) – 18:00UT (10/1/1997)

**Table 4-1** Summary of the 10/1/1997 storm characteristics.

The positive storm phase is generally accepted (Szuszczewicz et al., 1998; Foerster and Jakowski, 2000) to be induced by the strong equatorward thermospheric winds in the expansion phases, reducing the ion loss and effectively increasing the ion production in the day-time hemisphere. The most significant consequence is the plasma uplifting effect – the strong meridional winds push the F2-layer plasma upward, leading to reduced F2-layer peak density and increased hmF2 and TEC. This effect can be easily detected from measurements through the slab thickness shape parameter  $\tau$  ; increasing slab thickness (e.g. rising TEC accompanied by constant or decreasing foF2) indicates plasma uplifting. A clear demonstration of this process is detected in the 09:00-1100 UT period when TEC is rising, foF2 is almost unchanged, and hmF2 also increases (Fig.4-2C and Fig.4-2D). The wind-induced uplifting takes place along the geomagnetic field lines, and is therefore most efficient near the 45° geomagnetic inclination. Situated at 50.1°N, the Dourbes Geophysics Centre provides an excellent database for investigating the effect.

Since the positive phase observation is initiated at night, the positive cause-effect description given above cannot be applied for the increased night-time densities. Instead, it should be attributed to the downward fluxes. The plasma fluxes from the plasmasphere are due to the compression of the geomagnetic field during the onset phase of the storm (Rishbeth et al., 1987; Foerster and Jakowski, 2000) and/or inter-hemispheric flows. Such plasmaspheric fluxes can be easily detected: e.g. a high slab thickness value during night-time is certainly an indication of an enhanced plasma influx from above. This is exactly the situation observed near 02:00UT (Fig. 4-2D).

The next effect of interest is associated with the generated convection electric field. The sharp decrease of the slab thickness after 02:00UT shows the reaction of this field. The observed enhancement of foF2 (02:00-03:00UT) is explained with the plasmasphere compression due to the electric field. There is no unique explanation for the decrease; a possible explanation is the occurrence of zonal disturbance electric fields. A westward electric field moves the plasma from higher to lower L-shells with smaller volumes. Thus, the plasma pressure in the flux tubes is increased, causing an enhanced plasma flux from the plasmasphere down to F2 region altitudes. An eastward electric field results in the opposite effect of plasma decompression so that the plasmaspheric flux decreases (Mikhailov and Foerster, 1999).

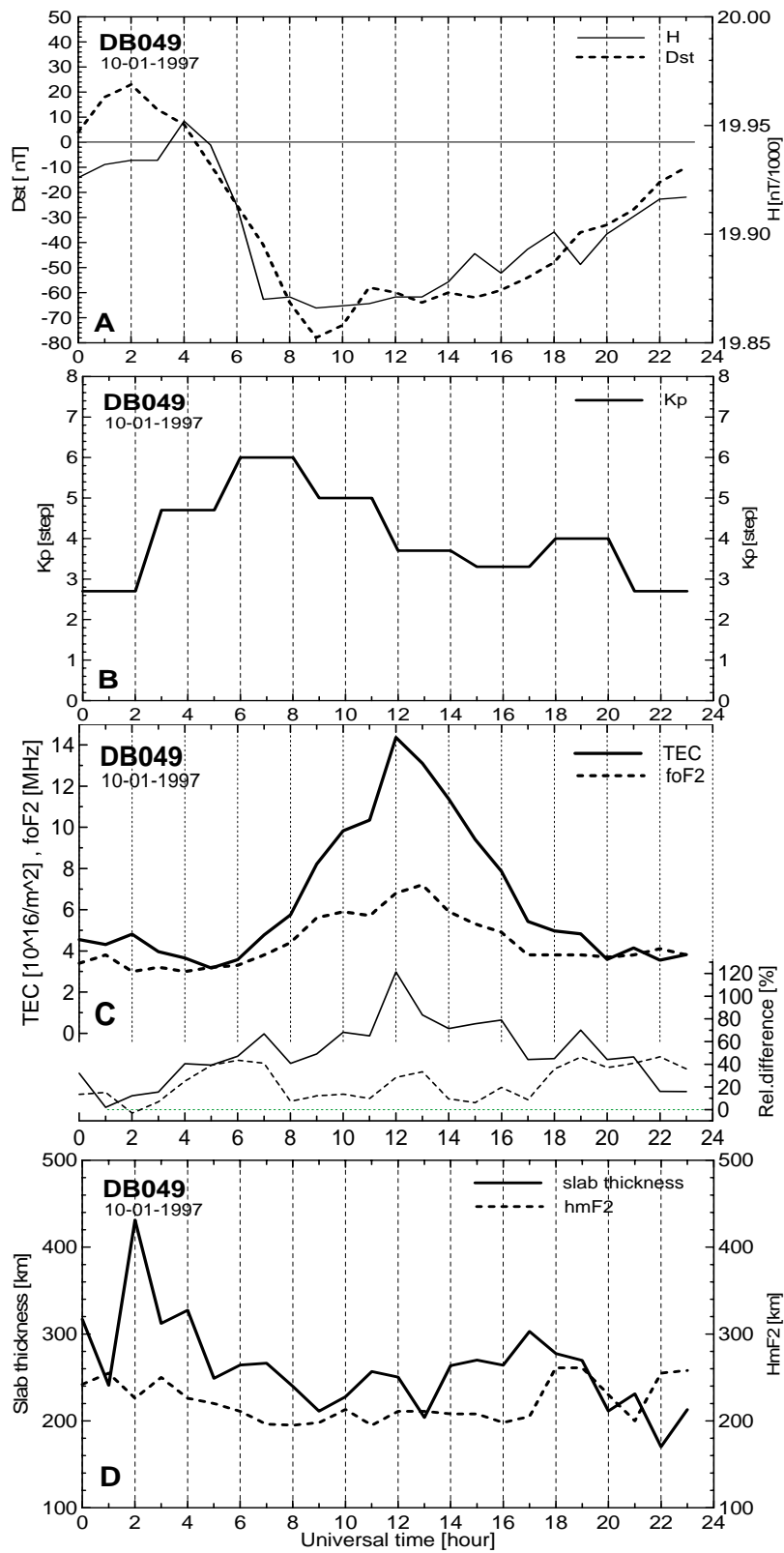


**Fig. 4-2** Ionosphere-plasmasphere response to the 10/01/1997 geomagnetic storm, as observed at the Dourbes station (DB049) site.

## 4.2 The storm on 15-17 July 2000

Another first-class geomagnetic storm was observed during the summer period 15-17 July 2000. The SSC is recorded at 1440 UT (Fig.4-3 and Fig.4-4A) and follows a disturbed period starting approximately 24 hours earlier (Fig. 4-3).

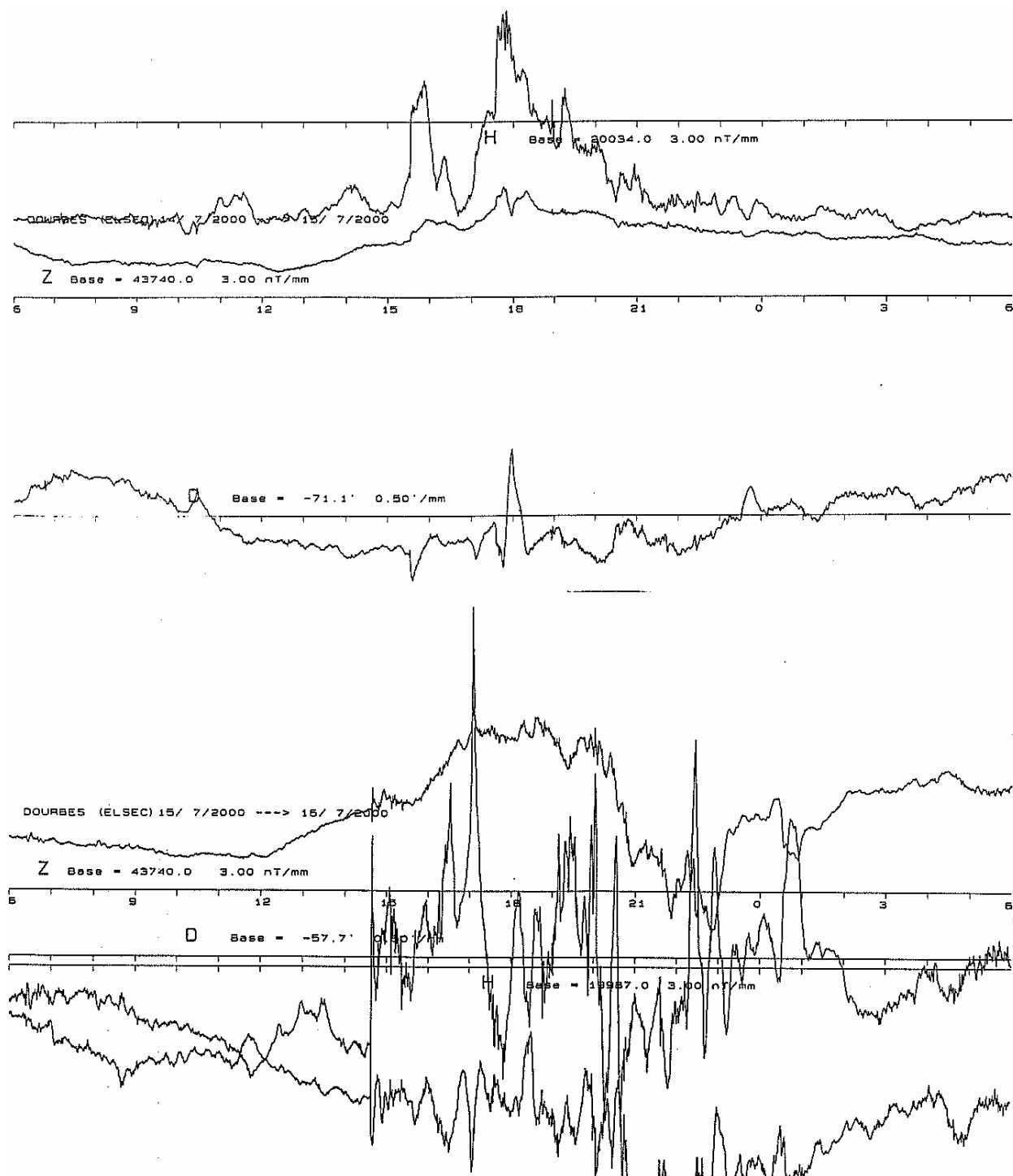


Fig. 4-3 The ELSEC magnetogram at the Dourbes Geophysics Centre during 15-17/07/2000 geomagnetic storm.



It is a severe storm showing a pronounced negative response in both the TEC and foF2 values. The total storm period is estimated to be about 49 hours; 4 hours for the main phase and 45 hours for the recovery phase. The main phase of the storm is observed in the evening hours of 15 July (from 1700UT until 2100UT, when very low Dst value of  $-300\text{nT}$  is detected. Other details of the important storm characteristics are given in Table 4-2 .

<i>Feature</i>	<i>Value</i>	<i>Comments</i>
<i>Storm onset (SSC)</i>	14:35 UT	14:35UT , 15/7/2000
<i>Dst (min)</i>	-300 nT	21:00 UT , 15/7/2000
<i>Total storm period ( Dst <math>\leq</math> -50nT )</i>	49 hours	17:00UT (15/7/2000) – 18:00UT (17/7/2000)
<i>Initial plus main phase ( SSC <math>\rightarrow</math> Dst(min) )</i>	6.5 hours	14:35UT (15/7/2000) – 18:00UT (15/7/2000)
<i>Main phase ( -50 nT <math>\rightarrow</math> Dst(min) )</i>	4 hours	17:00UT (15/7/2000) – 21:00UT (15/7/2000)
<i>Recovery phase ( Dst(min) <math>\rightarrow</math> -50 nT )</i>	45 hours	21:00UT (15/7/2000) – 18:00UT (17/7/2000)

**Table 4-2** Summary of the 15 July – 17 July 2000 storm characteristics.

The most intense negative response (in terms of depth of depletion) occurred in the early hours of the recovery phase, i.e. between 2100UT on 15/07/2001 and 0900UT on 16/07/2001. Around 0300UT on 16/7/2000, the relative differences increase to more than  $-80\%$  for TEC and  $-50\%$  for the critical frequency.

At high latitudes, the negative phase is attributed to the increased molecular concentrations of the thermosphere, enhancing the recombination processes and reducing the electron density. The standard explanation for a negative phase at middle and low latitudes (Szuszcwicz et al., 1998) is the enhanced equatorward wind system advecting the modified thermospheric composition to lower latitudes. This equatorward penetration is deeper at night-time, and theoretically, the corotation, coriolis forces, and zonal winds transport the modified thermospheric composition also to the day-time hemisphere and maintain the negative storm phase. Elements, which contribute to complicating this picture, involve: penetrating electric fields of magnetospheric origin, dynamo-driven fields, vertical and horizontal interactions between the wind system, thermospheric composition, ionospheric plasma, storm intensity, storm onset time (and associated local times in different longitude sectors), variations in pre-storm conditions, evolution of the controlling interplanetary-magnetospheric inputs, etc.

In contrast to the negative response of foF2 and TEC, the F2-layer peak height is, during all stages of the storm, either equal or higher than the undisturbed (quiet-time background) values (Fig.4-5). The situation however, is complicated because of the observed G conditions, which will be discussed below.

The hmF2 storm behaviour is a controversial issue. In this storm, the elevated hmF2 values do not result in positive storm responses. Thus, results here supports the suggestion (Szuszcwicz et al., 1998) that increased heights can cause positive or negative NmF2 phase responses, depending on the dominant influences. On the one hand, increased hmF2 and reduced chemical loss rates leads to increased NmF2 values. On the other hand, the increased height (during night) enhances the losses to the plasmasphere, resulting in substantial NmF2 reduction.

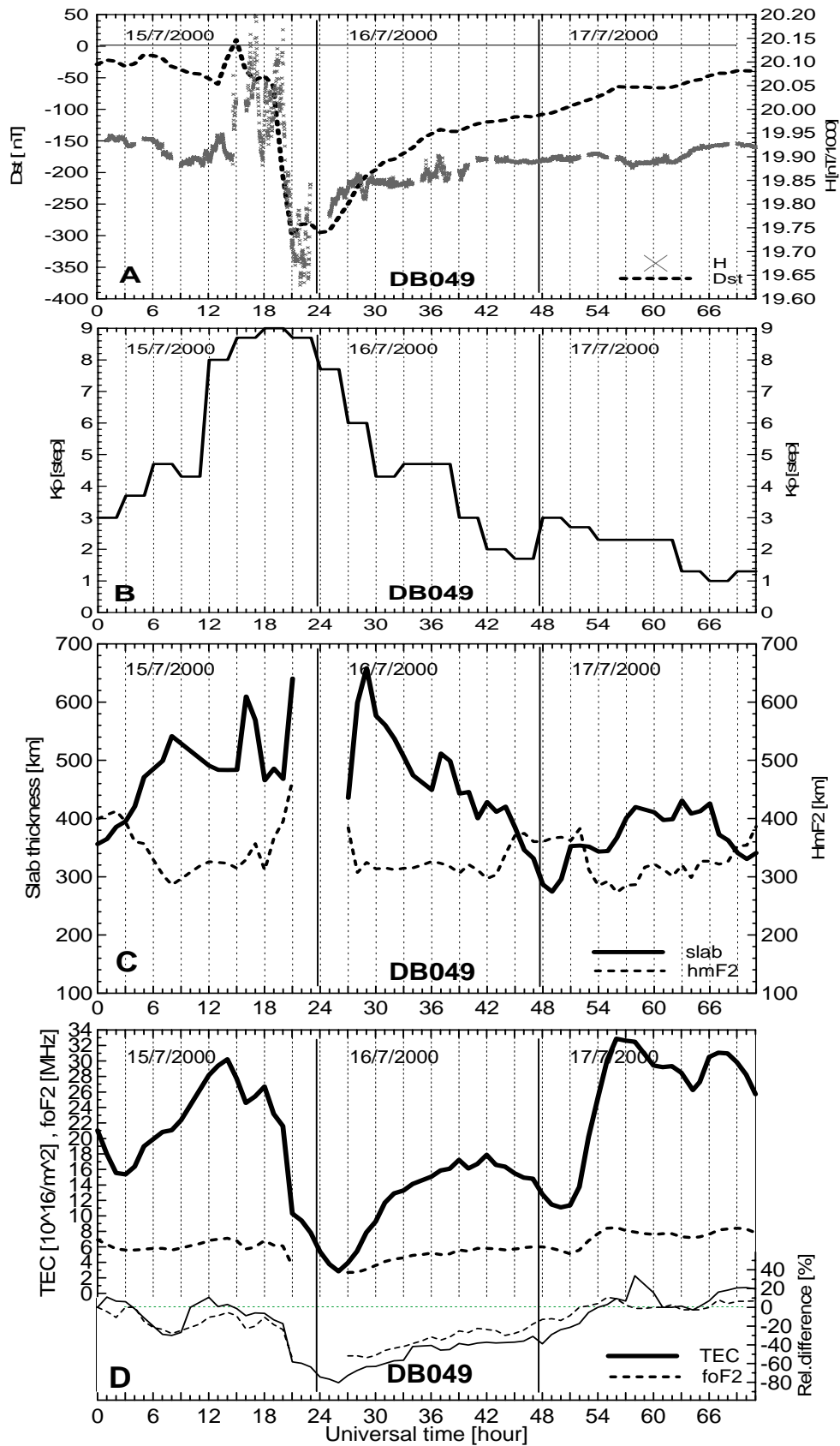
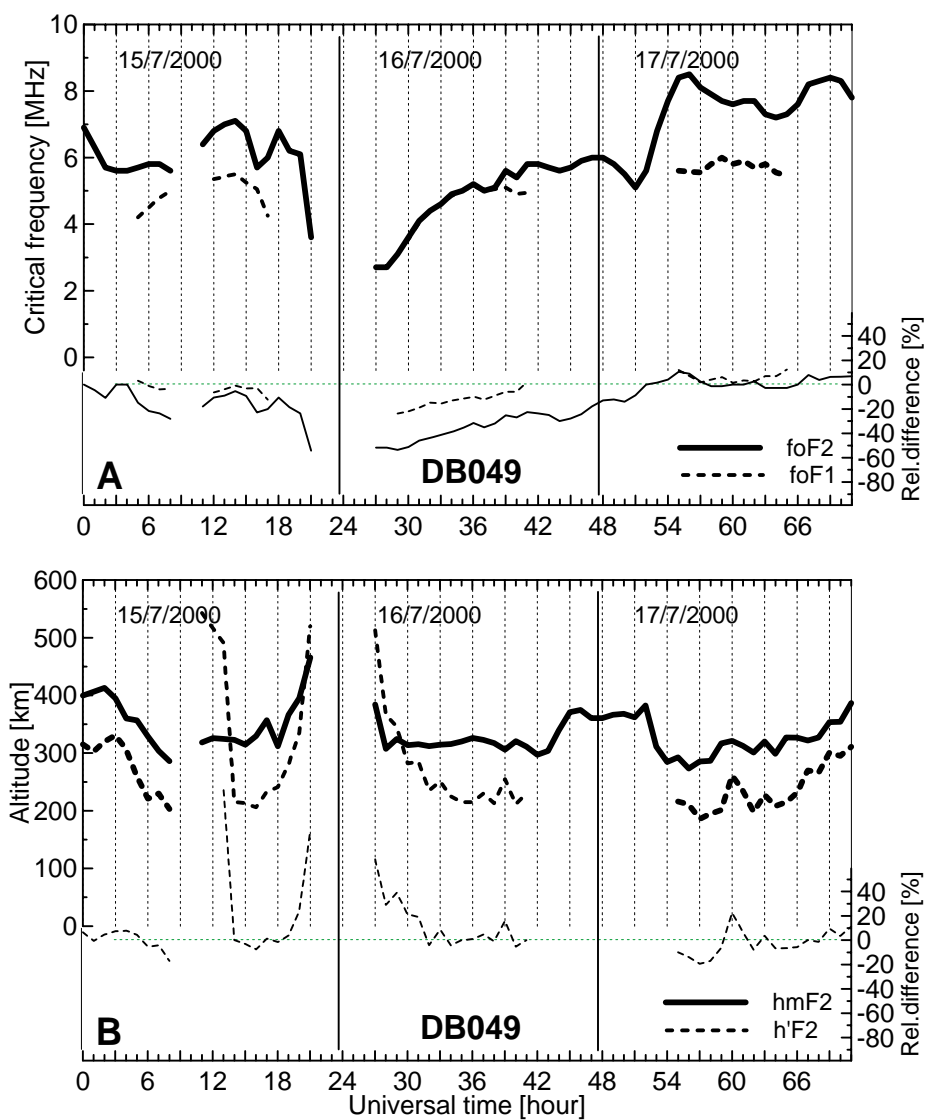


Fig.4-4 Ionosphere-plasmasphere response to the 15-17 July 2000 geomagnetic storm, as observed at the site of the Dourbes station (DB049).

This storm is interesting with revealing another phenomenon, the so-called ‘ionogram G condition’. Under G conditions, a measurement is influenced or impossible because the ionization density of the layer is too small to deduce the measurement value accurately. Such conditions occur during ionospheric disturbances associated with geomagnetic storms. Then, the electron density in the F2 layer becomes equal to or lower than the electron density in the F1 layer. In result, foF2 is expressed by the value of foF1 with the descriptive letter G. This is exactly the case on 16 July 2002 (Fig.4-5A): foF2 is equal to foF1 during the day, except for a few hours (1500-1700LT) in the afternoon.

However, it is important to separate the G condition from two other confusing cases. In the first case, the F2 trace disappears due to either interference (descriptive letter S) or attenuation (descriptive letter R). In the other case, the F2 trace cannot be recorded because of its extremely high virtual height ( $h'F2$ ) exceeding the height range limit (descriptive letter W). Such extremes happened from 2100UT on 15 July 2000 ( $h'F2 = 520\text{km}$ ) until 0300UT on 16 July 2000 ( $h'F2 = 513\text{km}$ ) when  $h'F2$  was consistently higher than the ionosonde’s height range limit (Fig.4-5B).

In all of the above cases, the automatic ionogram scaling may fail to properly identify the foF2 and hmF2 values, may not produce electron density profiles, or may deliver profiles which can be quite different from the real ones. The associated ITEC (ionosonde-based TEC) calculations, derived from such erratic profiles, can be very misleading. If available, concurrent GPS-based TEC measurements can be extremely useful. On the one hand, such TEC measurements provide opportunities for identification and possibly correction of ionosonde measurements under the above G ( and / or W ) conditions. On the other hand, the TEC values can be used to deduce the electron density profiles using the novel reconstruction method described in the following Chapter 7.



**Fig. 4-5** The critical frequencies and peak heights during the 15-17 July 2000 geomagnetic storm, as observed at the site of the Dourbes station (DB049).

### 4.3 The storm on 31 March 2001

The last storm considered here occurred in the equinox period 31 March – 2 April 2001. It started also during night, at around 00:30UT and demonstrated strong perturbations in the geomagnetic field components (Fig.4-6).

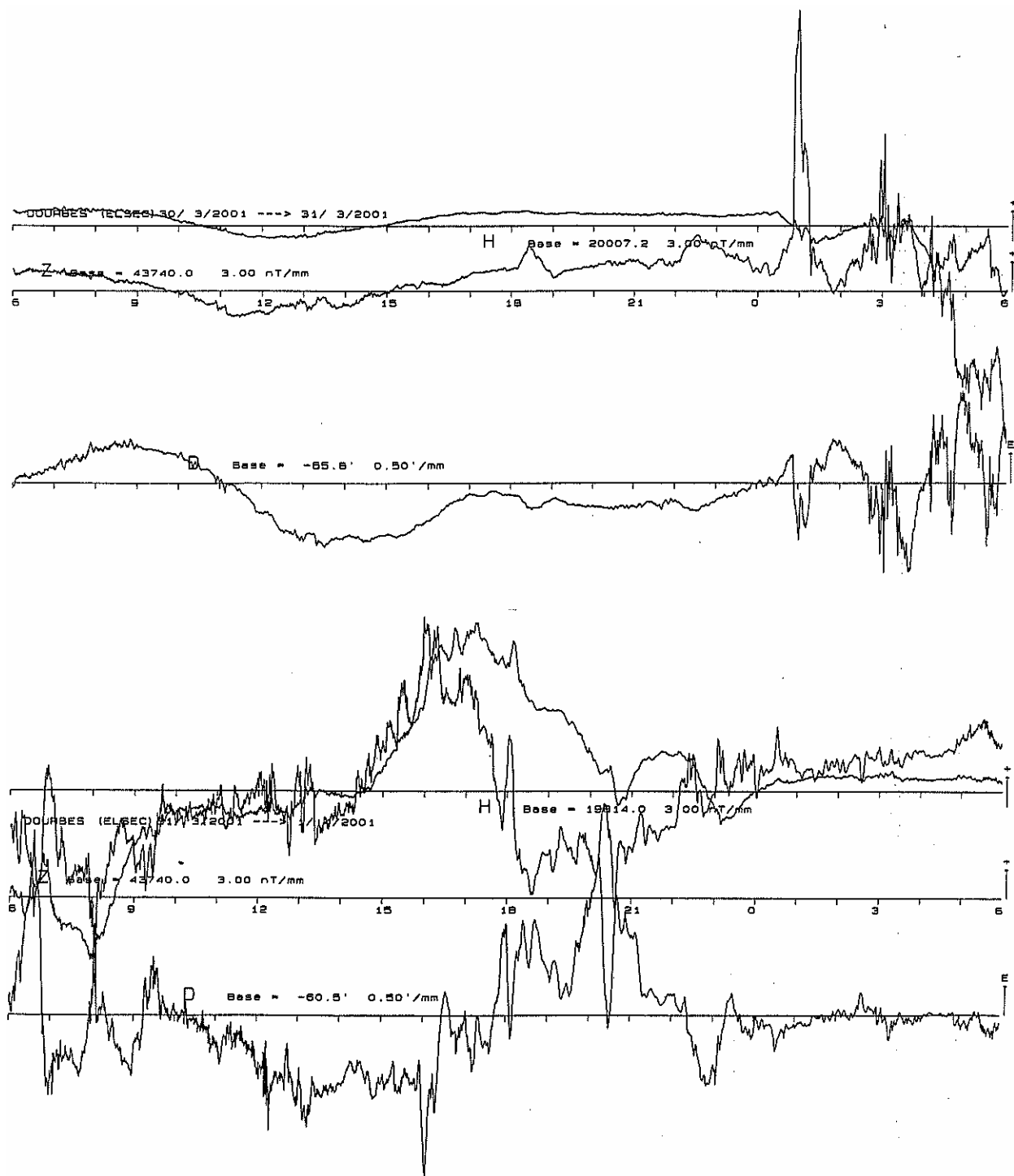


**Fig. 4-6** The ELSEC magnetogram at the Dourbes Geophysics Centre during 31/03-2/04/2001 geomagnetic storm.

Observed are also occurrences of irregular short-period fluctuations which is common for severe

magnetic storms. Such fluctuations, having a wide period spectrum from minutes to hours, are detected at all latitudes, but are stronger at higher latitudes. In extreme cases, it is almost impossible to reliably determine the main storm field at polar latitudes.

<i>Feature</i>	<i>Value</i>	<i>Comments</i>
<i>Storm onset (SSC)</i>	00:30 UT	00:30UT (31/3/2001)
<i>Dst (min)</i>	-358 nT	08:00 UT (31/3/2001)
<i>Total storm period ( Dst ≤ -50nT )</i>	57.0 h	05:00UT (31/3/2001) – 15:00UT (02/4/2001)
<i>Initial plus main phase ( SSC → Dst(min) )</i>	7.5 h	00:30UT (31/3/2001) – 08:00UT (31/3/2001)
<i>Main phase ( -50 nT → Dst(min) )</i>	3.0 h	05:00UT (31/3/2001) – 08:00UT (31/3/2001)
<i>Recovery phase ( Dst(min) → -50 nT )</i>	54.0 h	08:00UT (31/3/2001) – 15:00UT (02/4/2001)

**Table 4-3** Summary of the 31 March – 2 April 2001 storm characteristics.

This storm is clearly defined as ‘severe’, considering the Kp maximum of 9 (Fig.4-7B) and the other storm characteristics (Table 4-3). An extremely sharp decrease of Dst is observed, reaching the absolute minimum value of  $-358$  nT at 0800UT on 31/3/2001. Strong negative ionospheric storm effects are observed in the measurements. The effects are best demonstrated on the GPS TEC measurements (Fig.4-7C and Fig4-7D) which values reach 65-70% below the TEC monthly medians.

The F2-layer critical frequency and peak height (Fig 4.7D) decrease also. Moreover, as in the storm during 15-17 July 2000, G conditions are detected again for several hours during daytime on 31 March 2001. Again, the hmF2 has values which are typical for hmF1, e.g. the recorded hmF2 values in the period 0900-1200UT are well below 200km. Also, the ionosonde observations fail for quiet a long period, from 1800UT on 31/03/2001 until 0400UT on 1/04/2001. This can be attributed to the follow-up severe storm event (Kp = 8.3 and Dst (min) =  $-283/285$ nT at around 2000UT on 31/3/2001).

The ionosonde-TEC, obtained during 31 March, is largely unrealistic and different (both in absolute value and diurnal behaviour) from the GPS TEC. This fact comes to strengthen the importance of having several independent and concurrent measurements when investigating complex geomagnetic storms and their effects. It is also preferable to calculate the storm-time ITEC from edited ionograms only.

Another interesting phenomenon, observed also in this storm, is the strong positive phase happening later (after about 1500UT on 1/04/2001) during the recovery phase, when the TEC relative differences rise quickly above the zero mark and on several occasions exceed +50%. Such positive phase can be attributed to downwelling in the recovery phase (Szuszcwicz et al., 1998), resulting in diminished loss rates and consecutive increase in the overall plasma production. This phenomenon occurs with greater intensity during daytime in the presence of solar ionizing radiation; theoretically, it is also possible to happen in the night-time hemisphere.

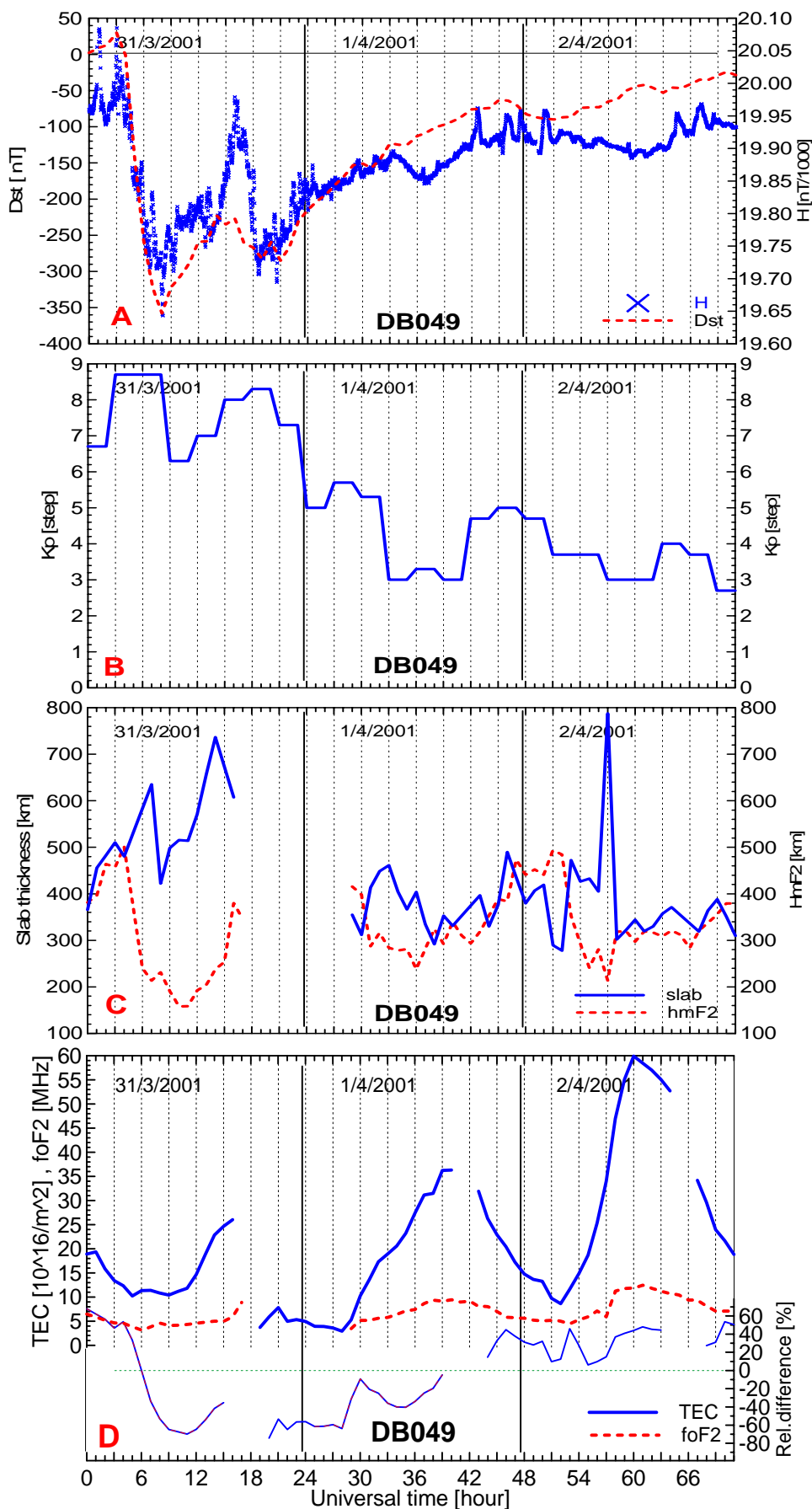


**Fig 4-7** Ionosphere-plasmasphere response to the 31 March - 2 April 2001 geomagnetic storm, as observed at the site of the Dourbes station (DB049).

## 4.4 **Discussion**

This report revealed the importance of several types of measurements in the storm studies carried out at a given location – the ionosonde digital observations, geomagnetic observations with emphasis on the variations of the field's horizontal component (H), the concurrent GPS-based TEC measurements, etc. There are also two other issues of significance – the necessity of higher time-resolution measurements and the global approach to the storm effects investigation.

It is of crucial importance to have higher time-resolution data (more frequent measurements) during storm times. For example if we work with hourly data, the above peak would be observed in 11:00, 12:00, 13:00 UT, hence the time delay would be 120 min resulting in a different wind velocity estimate. At the Dourbes Geophysics Centre we are able to provide 15 min sampling rate for GPS TEC and even better rate for the digital ionosonde. Thus, the TEC peak is observed at 12:30UT; which ensures better estimation of the propagation velocity.

The ionospheric storms can be much better investigated on a global scale. For the purpose, the RMI and the Royal Observatory of Belgium (ROB) jointly upgrade the existing GPS TEC measurements to provide the TEC values at practically every point in the European region. The propagation velocity of the perturbation is one of the important storm characteristics that can be investigated in this way. Some authors estimate this velocity in the order of 400-900[ms<sup>-1</sup>]. Theoretically, due to the reduced ion drag on the night side, the propagation should be much faster than on the day side. It is possible to estimate the time-delayed ionospheric reaction using simultaneous GPS TEC and ionosonde data. For example, if we observe the exact time of the day-time TEC peak at various geomagnetic latitudes near 0°E, we find that the peak is observed at 65°N in 11:30UT, at 50°N (Dourbes) in 12:30, at 35°N in 13:00UT. Thus, it obviously takes about 90 minutes for the plasma uplifting to move from 65°N to 35°N, which corresponds to a wind velocity of approximately 600 [ms<sup>-1</sup>].



## 5. **SYNTHETIC INDEX OF LOCAL RESPONSE TO MAGNETIC ACTIVITY**

The response of a given ionosphere characteristic  $F$  (like  $f_oF_2$ ,  $M3000F_2$ , or  $TEC$ ) is better analysed through the relative deviation,  $Fr = (F - F_{med})/F_{med}$ , of the actual observed characteristic from its median value,  $F_{med}$ . It strongly correlates to the geomagnetic indices (e.g.  $A_p$  and  $K_p$ ) in a highly non-linear fashion. For developing geomagnetically-correlated short-term forecasting methods, a new synthetic index is required (Muhtarov et al., 2001; Stankov et al., 2001; and the references therein).

This new synthetic index is actually a function showing the  $Fr$  relation to the geomagnetic index (say  $K_p$ ) used for the forecast. However, the new synthetic index (function) demonstrates strong seasonal and spatial variability and should be determined for each measurement site separately. At Dourbes, there are two types of measurements that can be used for the purpose – ionosonde ( $f_oF_2$ ) and GPS-based  $TEC$  measurements.

## 5.1 Index based on foF2 measurements

The project success required developing new ad-hoc methodology integrating the facilities of the DGS-256 digisonde and Artist4 (the processing software) in order to feed a near real-time processing to infer short term development of the ionospheric behaviour.

The synthetic index has been first deduced from foF2 measurements carried out at Dourbes over the period July 1957 to June 1989. It is calculated in the following manner. All values of the foF2 relative deviations in a given month of the year are sorted according to the hourly values of the planetary index Kp, which planetary index is recorded in step values of 0.00, 0.33, 0.67, 1.00, 1.33, ..., 8.67 and 9.00. Then, for each level of Kp and each month, the basic statistics are calculated – average, standard deviation, data number, etc. The results are presented in **Fig.5-1**, for the months of January, April, July, September (the top four panels) and a contour plot of the annual behaviour of the averages (bottom panel).

The first important observation made is the distribution of the zero value of the foF2 relative deviation, i.e. when  $foF2_{meas}=foF2_{med}$ . This is the value representing the ‘average’ magnetically quiet conditions. It is supported by the fact that the majority of the observations cluster at and around the median, which can be seen on the plots in **Fig.5-1**. It becomes obvious from the bottom contour plot that  $Fr=0$  is observed for  $Kp=2.67$  except for the winter months when  $Fr$  varies between the higher values of 3.00 and 4.00. Considering the definition of a quiet magnetic activity ( $0 < Kp < 4$ ), it follows that even within this interval a trend exists in the observations of  $Fr$ : generally positive response for  $Kp < 2.67$  and negative response for  $Kp > 2.67$ . The response of foF2 under intense geomagnetic activity ( $Kp > 4$ ) is negative, i.e. measurements are generally below their monthly medians. The decrease is particularly strong near the equinoxes (April and September) when the decrease reaches 25-30% during strong geomagnetic storms ( $Kp > 7$ ). On the other hand, the maximum positive values of  $Fr$  are also observed during April and September for small values of  $Kp$ .

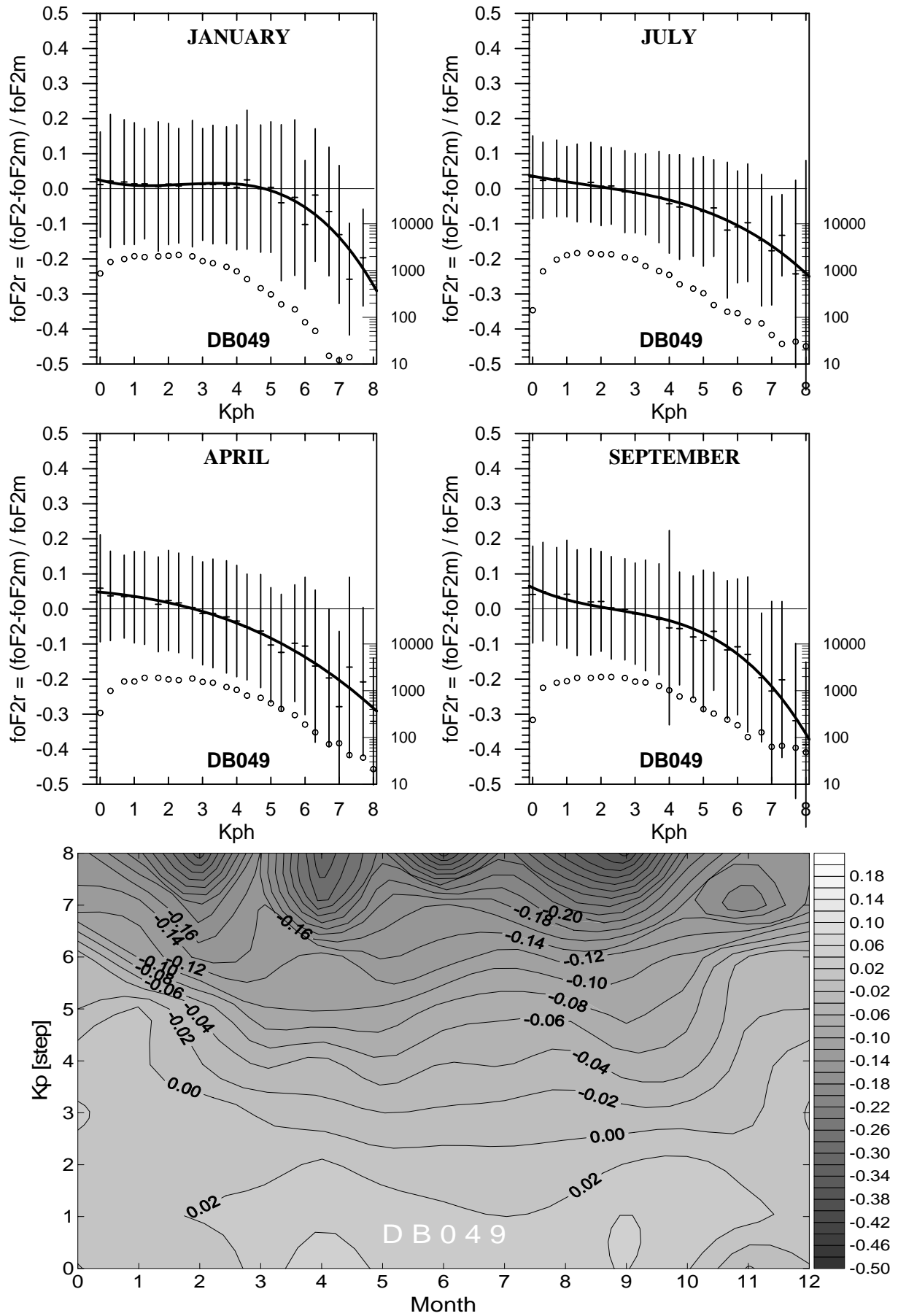


**Fig.5-1** The foF2-based synthetic geomagnetic index obtained for ionosonde station DB049 (1957–1989). The circles represent the data number, the vertical bars – the standard deviations (doubled). The averages (dashes) are approximated by 3-rd degree polynomials (solid lines)

## 5.2 Index based on GPS TEC measurements

It is interesting to compare the critical frequency response with the response of the GPS-based Total Electron Content (TEC). The TEC time series available at Dourbes (July 1994 – October 2001) is not so long as the foF2 series, and the data scattering is rather large, but some important differences are already detected. The TEC relative deviations have been sorted in the same way as the foF2 deviations and the results are provided in **Fig.5-2** using the same layout.

For the GPS-based TEC measurements, our calculations show that the TEC response is generally stronger and much more complex than the foF2-based observations. First, the ‘quiet’ behaviour,  $TEC_r = 0$ , is detected at lower Kp values of around 2.00 (a sign for a stronger response to the geomagnetic activity). Second, it is obvious (**Fig.5-2**), that for quiet magnetic conditions ( $K_p < 4$ ) the dependence of the relative TEC on Kph is similar to that of foF2. On the other hand, for higher values of the index the relative TEC stops decreasing and in many cases increases significantly particularly during winter months. It is clear at this stage that in November and December the increase of  $TEC_r$  during storms can be as much as 20-25%. There are indications that such an increase can be expected during January and even February but the data are rather scarce to draw proper conclusions. A pronounced decrease is observed during the April and September months for values of  $K_p > 4$ , although not as strong as in the foF2 case.

More measurement data and further analysis are required for better evaluating the GPS TEC – based response to the stronger geomagnetic activity.

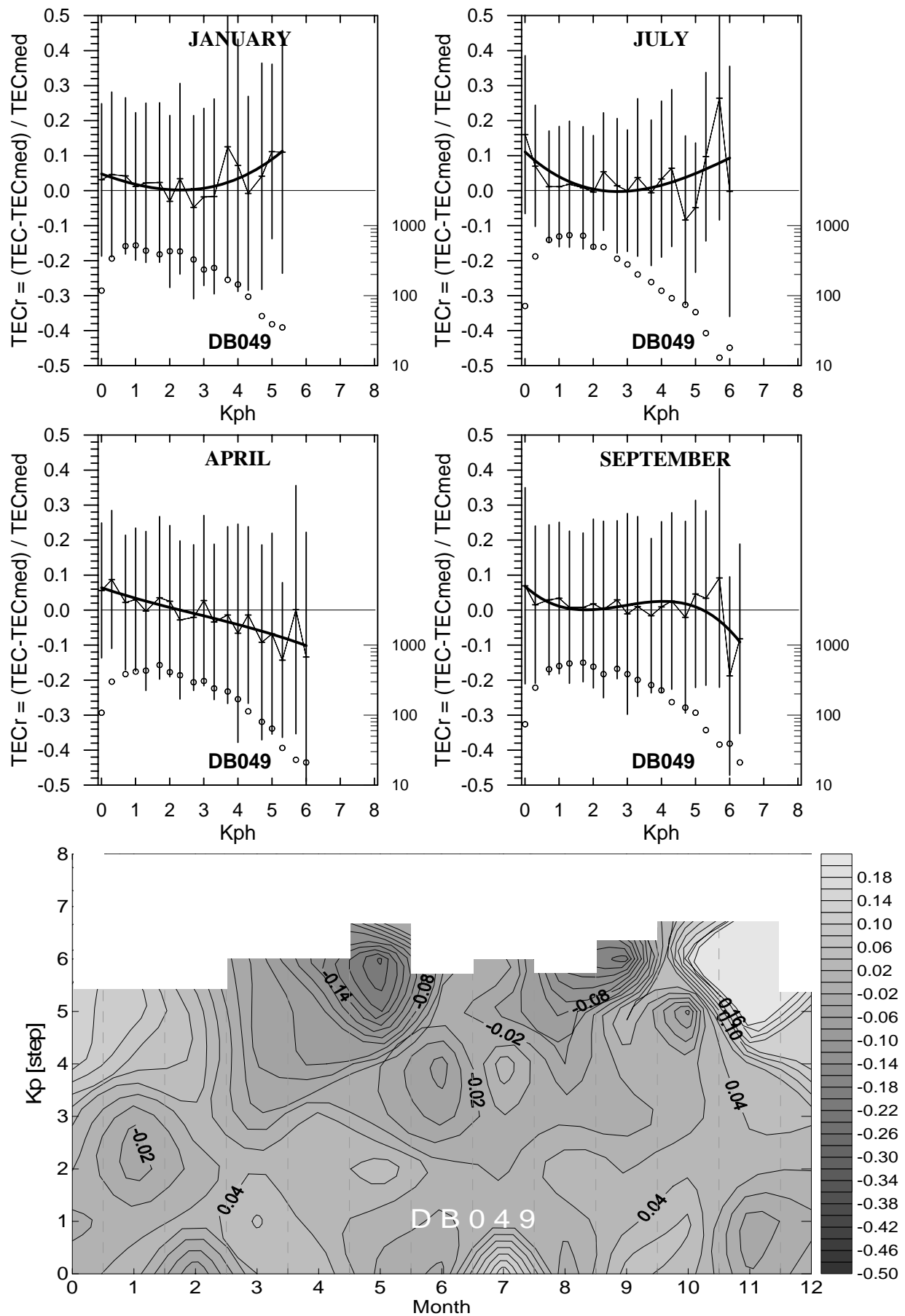


**Fig.5-2** The TEC-based synthetic geomagnetic index obtained for the site of station DB049 (1994–2001). The circles represent the data number, the vertical bars – the standard deviations (doubled). The averages (dashes) are approximated by 3-rd degree polynomials (solid lines)

*This page intentionally left blank.*

## 6. **A NEW METHOD FOR TEC FORECASTING BASED ON GPS MEASUREMENTS**

The Total Electron Content (TEC) is a robust characteristic for investigation of the ionosphere-plasmasphere behaviour under both quiet and disturbed conditions. Instantaneous maps of TEC and other ionospheric characteristics are used mostly in the management and optimisation of the high-frequency radio and remote sensing systems, for satellite navigation, development and evaluation of ionosphere-plasmasphere models, etc. Therefore, a TEC short-term forecasting model, based on regular and reliable Global Positioning System (GPS) observations, can be utilized to improve the telecommunication and navigation practice and could be considered in various space-weather issues. Various approaches have been used to model and predict the TEC: empirical, theoretical, neural networks. Recently, auto- and cross-correlation procedures have been developed (Muhtarov and Kutiev, 1999; Kutiev et al., 1999; Muhtarov et al., 2001; Kutiev and Muhtarov, 2001) for predicting the critical frequency and proving that a short-term forecast should be bound to the geomagnetic activity.

The main idea in the proposed forecasting method is to consider the TEC temporal behaviour as composed of a periodic component and a random component. The periodic component represents the average (annual, diurnal) non-disturbed variation (traditionally represented by monthly medians), while the random component represents the perturbations inflicted on the TEC behaviour due to the strong changes in solar/geomagnetic activity. The method consists of two major components: (i) Extrapolation of the TEC monthly median values for up to 15 days ahead. The procedure uses Fourier series approximation based on actual data from the past 12 months and autocorrelation adjustment over the past 30 days of data. (ii) Forecast of the relative deviations of the measured TEC from its median values for up to 24 hours ahead. This forecast depends on the Kp index and is adjusted to the current conditions through an autocorrelation procedure.

Presented are some preliminary results from developing this new method for the single-site TEC forecast based on GPS measurements of the content and on solar/geomagnetic activity indices. If such a forecast is made at several locations in a given area, instantaneous maps can be constructed for the whole region.

#### *Data base:*

Two basic types of measurements are required for the method - GPS-derived TEC and solar-geomagnetic activity data. The development database was built on the GPS TEC time-series data acquired at RMI Geophysics Centre at Dourbes in 1994-2001, covering low, rising and top solar activity. The ionosphere-plasmasphere system existence and variability is mostly determined by the solar and geomagnetic activity. A proper choice of indices is required for the TEC forecasting purposes.

#### *Dependence on solar activity:*

The index chosen to represent the solar activity is F10.7. To better analyse the annual behaviour, the TEC 31-day running median values are normalised to the linear approximation of the TEC variations for the current year. The TEC response to the solar activity is rather complex ( **Fig.6-1** and **Fig.6-2** ). First, the TEC is strongly bound to the solar activity and its variability is significantly increasing with rising solar activity. Second, the summer maximum observed at low solar activity (LSA) is eroded at high solar activity (HSA), while two equinox maxima appear to strongly dominate the annual profile. During day-time, the summer peak, observed at LSA, is gradually disappearing at higher solar activity. Night-time, the same happens to the LSA winter peak, which also gives way to two peaks observed near the HSA equinoxes.

#### *Dependence on geomagnetic activity:*

Many indices have been developed during the years for expressing the geomagnetic activity: the Kp and Ap planetary indices, the storm Dst index, the sub-storm index PC, etc. The Kp and Ap indices are probably the most suitable for reference when carrying out preliminary correlative studies with other related geophysical phenomena. A three-day forecast of the Ap index is issued by the NOAA Space Environment Center in Boulder USA, equipping the TEC forecasting method with one of the key input parameters. The daily Ap is nominally assigned to the 12:00LT hour and the hourly Ap values (denoted Aph) are obtained by linear interpolation. The Aph values are then converted to Kph through the established empirical relation  $Kp=1.739\ln(0.423A_p)$ .

The relative deviation,  $F_r = (F-F_{med})/F_{med}$ , of a given ionospheric parameter  $F$  (e.g. foF2, M3000F2, or TEC) from its median value,  $F_{med}$ , depends on the Kp index in a non-linear fashion. A similar study (Muhtarov et al., 2001) on foF2 shows that the average dependence of the foF2 relative deviations on the Kp index has a parabolic form. However, the analysis of the TEC data reveals that, while the dependence of the relative TEC on Kph is similar to that of



foF2 under quiet conditions ( $K_{ph} < 4$ ), the dependence under disturbed conditions is quite complex (see **Chapter 5**). Of course, the TEC time series is not so long as the foF2 series, and the data scattering is rather large, so further analysis is required. To linearise the dependence, a new ‘synthetic’ index is utilised, which is a polynomial approximation of the TEC average relative deviation depending on the hourly index  $K_{ph}$ .

It has been proved that the cross-correlation between the relative deviation of the critical frequency and the geomagnetic index  $K_p$  is much higher when using the squared  $K_p$  (i.e.  $K_p^2$ ) than when using  $K_p$  itself (Muhtarov et al., 2001). Also, the ionosphere reaction to the geomagnetic forcing is delayed (Kutiev and Muhtarov, 2001), so it is reasonable to describe this reaction as a dynamic relaxation process (i.e. exponentially decreasing magnitude) developing from a given initial stage. Thus, instead of using the  $K_p$  index, another index  $K_m$  is introduced (named modified  $K_p$ ) which is defined as a solution of the following ordinary differential equation of first order:

$$T \frac{dK_m(t)}{dt} + K_m(t) = K_p^2(t)$$

The left-hand side of this equation describes the relaxation of  $K_m$  with a time constant  $T$ , while the term on the right-hand side represents the perturbation imposed on the pure relaxation of  $K_m$ . Practically, the time constant  $T$  is a measure of the delayed reaction of the ionosphere to the geomagnetically-induced perturbations, and it is found that  $T$  is highly variable ( $T \approx 18h$ ). By adjusting the time constant, the  $K_m$  function can be obtained very close to the function describing the relative deviation of a parameter.

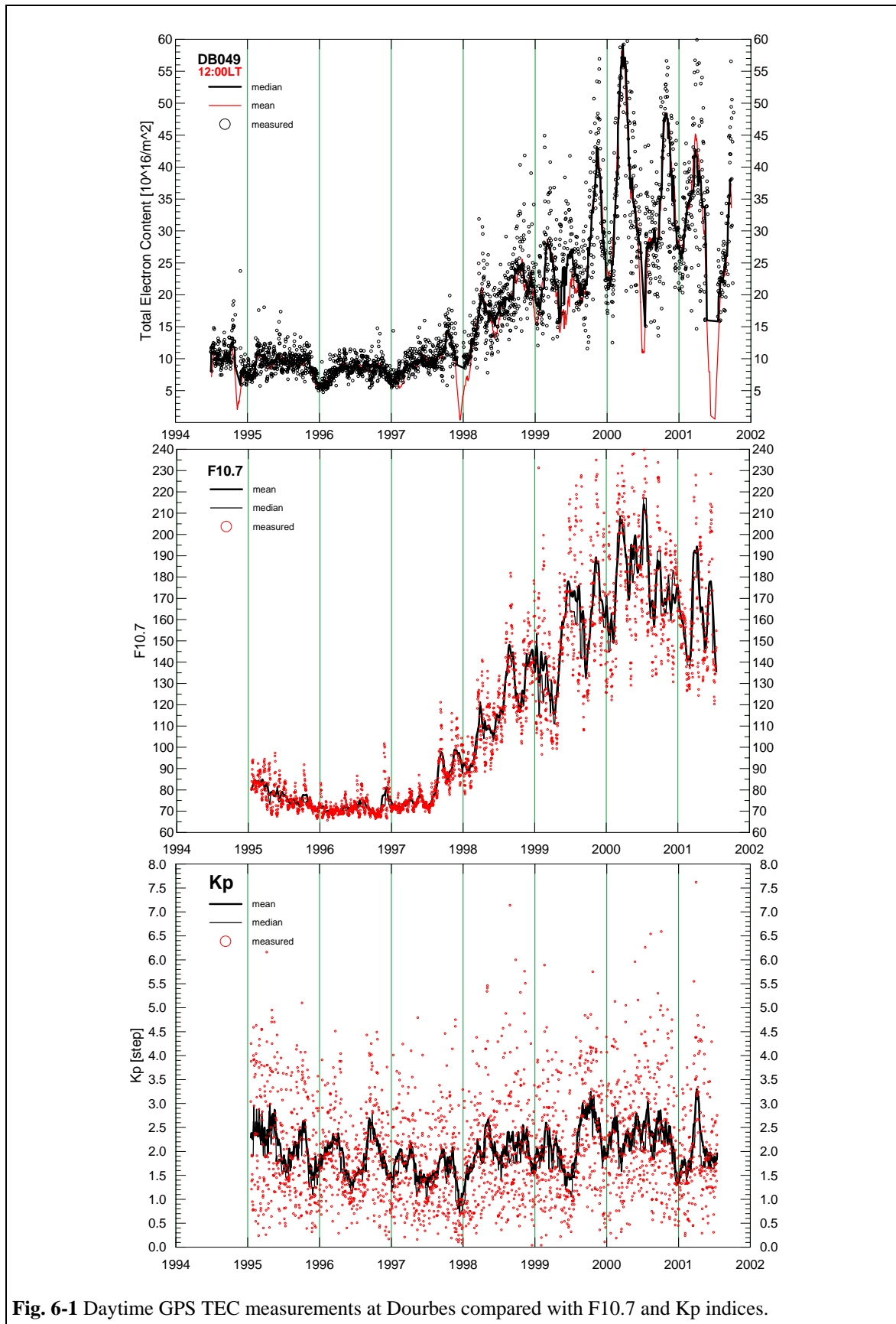


**Fig. 6-1** Daytime GPS TEC measurements at Dourbes compared with F10.7 and Kp indices.

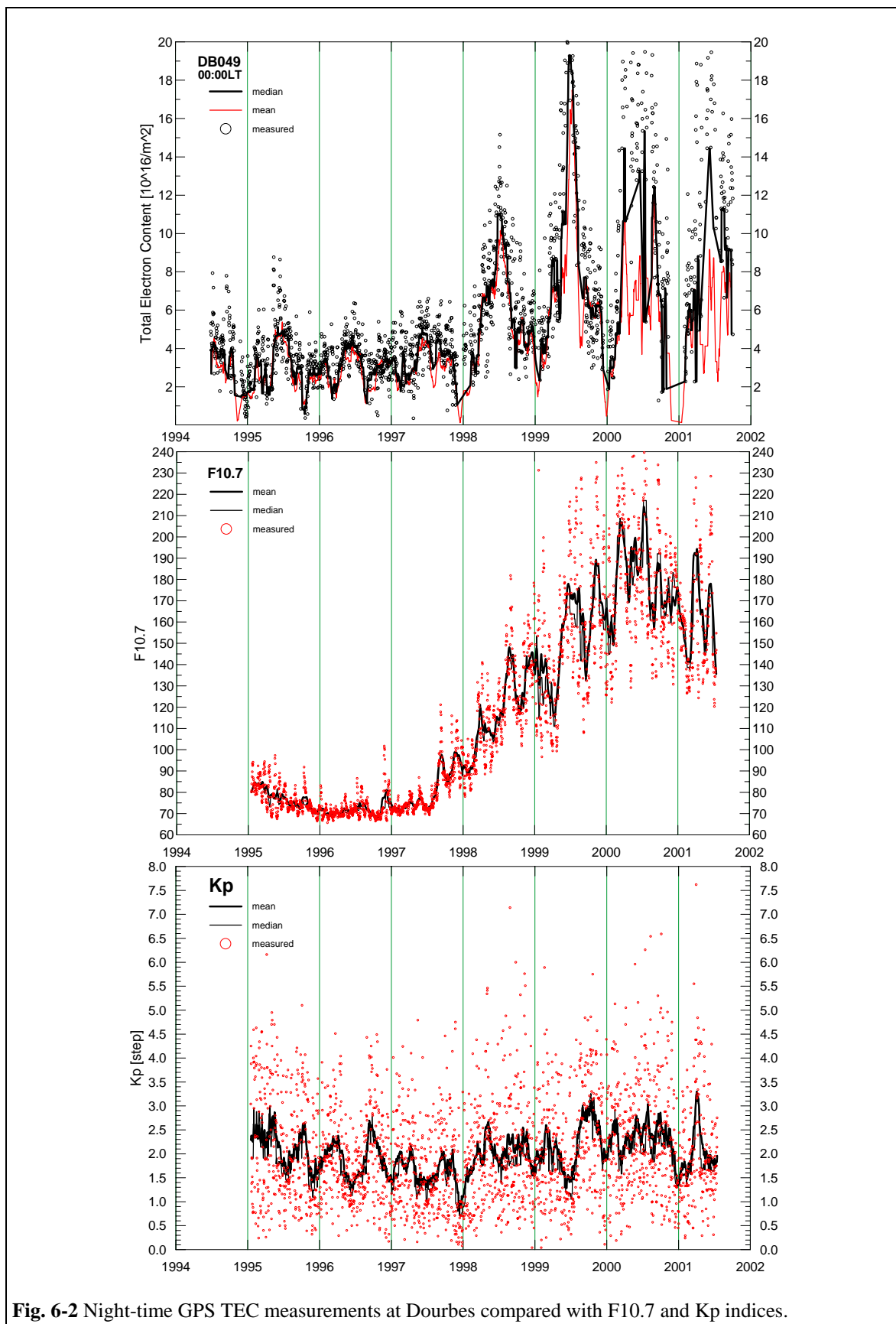


Fig. 6-2 Night-time GPS TEC measurements at Dourbes compared with F10.7 and Kp indices.

## 6.1 Monthly-median forecast

The monthly-median extrapolation procedure uses Fourier series approximation based on actual data from the past 12 months. The reasons we base the forecast on the monthly median are: i) the smooth annual variability of the TEC median value for a given hour, and ii) the similar pattern exhibited by the TEC measurements at all stations.

The TEC median value for each hour of the day is separately approximated using the following Fourier series decomposition:

$$TEC(d;h) = \frac{1}{2}a_0(h) + \sum_{i=1}^{n_{max}} \left[ a_i(h) \cos\left(i \frac{2\pi}{360} d\right) + b_i(h) \sin\left(i \frac{2\pi}{360} d\right) \right]$$

where  $d$  is the day of the year,  $h$  is the local time, and  $n_{max}$  is the number of the harmonic with the highest frequency.

The procedure can be used for both interpolation and prediction purposes. If a one-day long gap is placed at the end of the data period, then the method will implicitly extrapolate the values within the imposed gap and will thus offer prediction values up to the length of the gap. In this case less data is required (30 days) to make a reliable one-day prediction. It is justified because the diurnal variations are much more stable than the annual. Both types of extrapolations (annual and diurnal) are used here and the resulting prediction is the average of both values for a given hour.

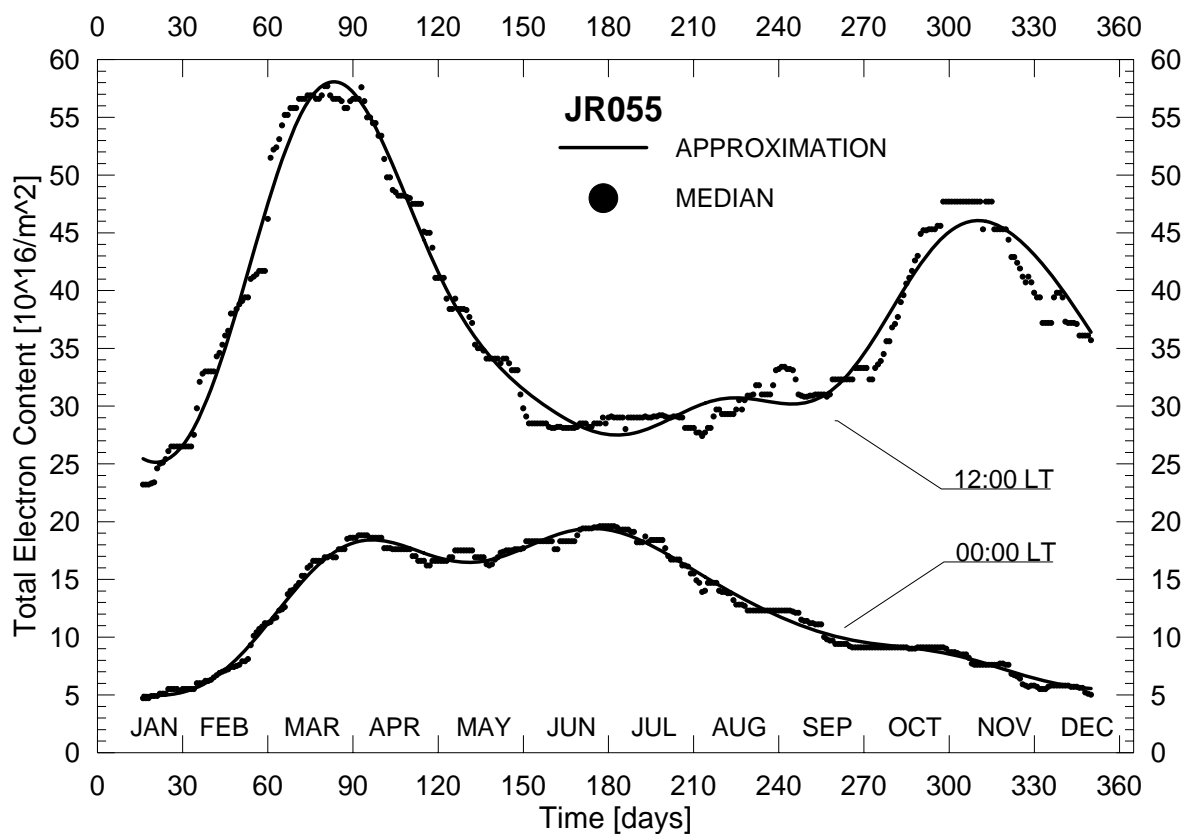


**Fig.6-3** The approximated TEC 31-day running medians at 00:00LT (below) and 12:00 LT (above) during year 2000.

### Adjustment of the monthly median forecast:

The monthly-median extrapolation procedure is improved by an auto-correlation adjustment based on data from the last 30 days. This procedure relies on the diurnal rather than the annual behaviour of TEC. In the presented adjustment procedure, instead of the parameter's absolute value, the relative deviation from its median is used,  $F_r = (\text{TEC} - \text{TEC}_{\text{med}}) / \text{TEC}_{\text{med}}$ . This function contains no periodic components and can be regarded as a steady-state random process over the considered period of time. Having measurements of  $F_r$  at times  $t_i$  ( $i=1,2,\dots,n$ ), the aim is to predict the values of  $F$  at future moments  $t_{n+1}, t_{n+2}, \dots, t_{n+k}$  where  $(t_n, t_{n+k})$  is the length of the prediction period. For the purpose, a regression model (Muhtarov and Kutiev, 1999) is used :

$$F(t_{n+1}) = F_m + \sum_{i=1}^n \beta_i (F(t_i) - F_m)$$

where  $F_m$  is the sample's median. The weight coefficients are determined from the following system:

$$\sum_{i=1}^n \beta_i r_{FF}(t_i - t_j) = r_{FF}(t_{n+1} - t_j), \quad j = 1, 2, \dots, n$$

where  $r_{FF}$  is the auto-correlation function of  $F$ . Practically, the real  $r_{FF}$  is unknown, so the normalised empirical auto-correlation function is used instead:

$$\rho_{FF}(\tau) = \frac{\sum F_i F_{j(i)}}{\sqrt{(\sum F_i^2)(\sum F_{j(i)}^2)}}$$

where the summation is performed over the pairs of  $F(t)$  having a same time difference  $\tau$ . It is implicitly assumed that the empirical mean is zero, which is justified for series of several days. Also, because the empirical auto-correlation function is only an estimate of the true auto-correlation function, the accuracy of that estimate depends on the size of the data sample, which should be much larger than the number of the unknown coefficients.

Exemplary results are given in **Fig.6-4**. In the top panel, the averaged values of the diurnal and annual extrapolation is given, and this approximation is further adjusted by the auto-correlation procedure using the last 30 days of data. In the middle panel, the relative error of the forecast, i.e.  $(\text{TEC}_{\text{forc}} - \text{TEC}_{\text{med}}) / \text{TEC}_{\text{med}}$ , is plotted for each hour of the testing period of 30 days. The averaged values (within each hour of the day) of the relative and absolute relative errors are given in the bottom panel. The relative errors are larger during night (reaching occasionally 10%) but in the rest of the time are varying between 1 and 3%.

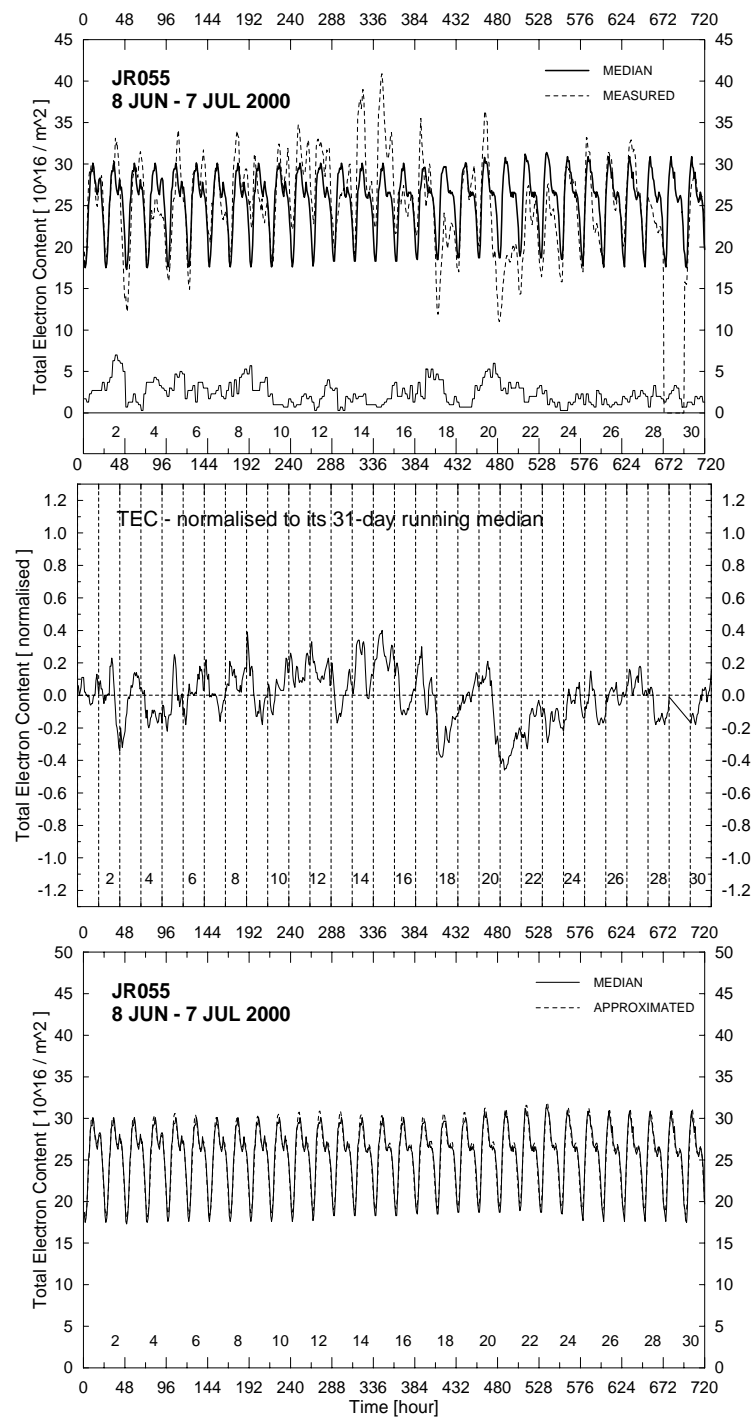


**Fig.6-4** TEC running medians, relative deviations from medians, and autocorrelation approximation during June/July 2000 for station JR055

## 6.2 Geomagnetically-correlated short-term forecast

The TEC short-term forecast is improved by introducing cross-correlation between the TEC relative deviation from its median value and the modified index Km. Thus, the following regression formula (Muhtarov et al., 2001) is used for predicting the relative deviation:

$$F_{n+1} = F_m + \sum_{i=1}^n \beta_i (F_i - F_m) + \sum_{i=1}^{n+1} \beta_i (G_i - G_m)$$

where  $G(t)$  is the geomagnetic function (approximation of the modified geomagnetic index Km). The weight coefficients are determined from the following system:

$$\sum_{i=1}^n \beta_i \rho_{FF}(\tau_{ij}) + \frac{\sigma_G}{\sigma_F} \sum_{i=1}^{n+1} \gamma_i \rho_{FG}(\tau_{ij}) = \rho_{FF}(\tau_{n+1,j}) \quad j = 1, \dots, n$$

$$\sum_{i=1}^n \beta_i \rho_{GF}(\tau_{ij}) + \frac{\sigma_G}{\sigma_F} \sum_{i=1}^{n+1} \gamma_i \rho_{GG}(\tau_{ij}) = \rho_{GF}(\tau_{n+1,j}) \quad j = 1, \dots, n+1$$

The auto-correlation functions depend on the time shift,  $\tau_{ij}=t_i-t_j$ , only. Here,  $\rho_{FG}$  (note that  $\rho_{FG}=\rho_{GF}$ ) is the cross-correlation function between  $F(t)$  and  $G(t)$ , defined

$$\rho_{FG}(\tau) = \frac{\sum F_i G_{j(i)}}{\sqrt{(\sum F_i^2)(\sum G_{j(i)}^2)}}$$

where again the summation is performed over the pairs of  $F(t)$  having the same time difference  $\tau$  in the data sample. The  $F$  and  $G$  auto-correlation functions are  $\rho_{FF}$  and  $\rho_{GG}$ , and the corresponding standard deviations are :

$$\sigma_F = \sqrt{\frac{1}{n} \sum_{i=1}^n F(t_i) - \left( \frac{1}{n} \sum_{i=1}^n F(t_i) \right)^2}$$

$$\sigma_G = \sqrt{\frac{1}{n+1} \sum_{i=1}^{n+1} G(t_i) - \left( \frac{1}{n+1} \sum_{i=1}^{n+1} G(t_i) \right)^2}$$

Statistical sufficiency of the auto-correlation functions is ensured by using parametric expressions. The auto-correlation function of  $G$  decreases exponentially with increasing the time difference,  $\tau$ , which leads us to the conclusion that this auto-correlation function has the following form:

$$R_{GG}(\tau) = G_{mean} + \sigma_G^2 \exp(-|\tau|/T_G)$$

known in the signal-processing theory as ‘random telegraphic wave’. The auto-correlation is symmetrical with respect to  $\tau=0$  and decreases with a time constant  $T_G$ .

In resume, the geomagnetically-correlated forecasting procedure works as follows. First, the TEC data, from the 30-day period prior to the date of forecast, are assembled and the TEC hourly medians are calculated. Second, all TEC relative deviations from the median value are computed. Third, the Kph index is obtained over the whole data period including the day of the prediction. Next, all values  $G_i$  of the geomagnetic function are derived. Further, based on the available data from the 30-day period, the cross- and auto-correlation functions of  $F$  and  $G$  are determined together with the weighting coefficients. Finally, the required 24 values of  $F_r$  for the forecasted day are obtained using the regression formula.



### 6.3 Results and discussion

The TEC hourly time series is considered as a sum of two components - periodic and random. The periodic component is non-random and describes the TEC mean behaviour (represented here by the 31-day running medians). On the other hand, the random component describes the TEC fluctuations supposedly inflicted by the geomagnetic field disturbances. These fluctuations are supposed to be a manifestation of a stationary stochastic process. The stationarity hypothesis implies that the mean  $E\{n(t)\}$  and the product moment  $E\{n(t)n(t+\tau)\}$  are independent on  $t$ , where  $E$  denotes the mathematical expectation. Such interpretation suggests that the TEC median behaviour is the signal, and the fluctuations are noise.

The method has been tested for 24-hour median predictions; exemplary test results are provided in **Fig.6-5** for high solar activity. The first prediction hour is 00:00 LT and the last 23:00 LT of the same day. In the top panel, the averaged values of the diurnal and annual extrapolation is given. In the bottom panel, the absolute and real values of the relative error (averaged within each hour of the day) are plotted. The relative errors are larger during night (reaching occasionally 10%) but in the rest of the time are varying between 1 and 3%.

Basic sources of errors in this forecasting method are: the insufficiency of data measurements within a certain area, inevitable data smoothing inherent in the mathematical formulation, unknown and unstable relationship between the ionospheric characteristic and the solar-geomagnetic activity, etc.

The results of the geomagnetically-correlated short-term prediction of ionospheric parameters are presented and discussed elsewhere (Muhtarov et al., 2001) and will not be repeated here.

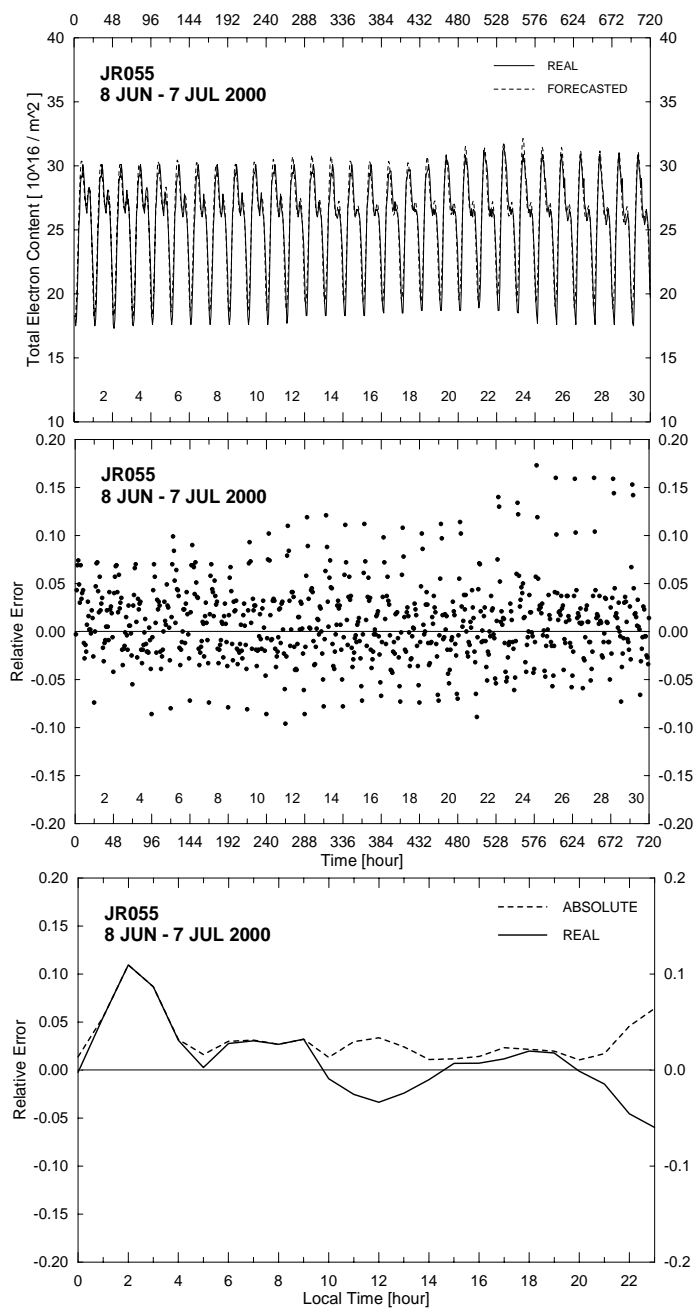


**Fig.6-5** Averaged 24-hour extrapolation of TEC 31-day medians during June/July 2000 for station JR055 (top panel). The relative error of the forecast is plotted in the middle panel for each hour. The real (solid line) and absolute (dashed line) relative errors are in the bottom panel.

## 7. A NEW METHOD FOR RECONSTRUCTION OF THE ELECTRON DENSITY PROFILE

Given the electron density profile (i.e. the altitude distribution of the electron density), it is relatively easy to calculate the corresponding vertical total electron content (TEC) using quadrature formulae. The purpose of this paper is to present a method for solving the inverse problem - deducing the electron density profile from the total electron content.

The GPS-measured TEC delivers the basic *quantitative* information about the sought electron profile. Additional information about the *shape* of the electron profile is also required, e.g. maximum density and height of the E and F layers, the curvature of the topside profile near the  $O^+ - H^+$  (upper) transition level (UTL), etc. (**Fig.7-1**).

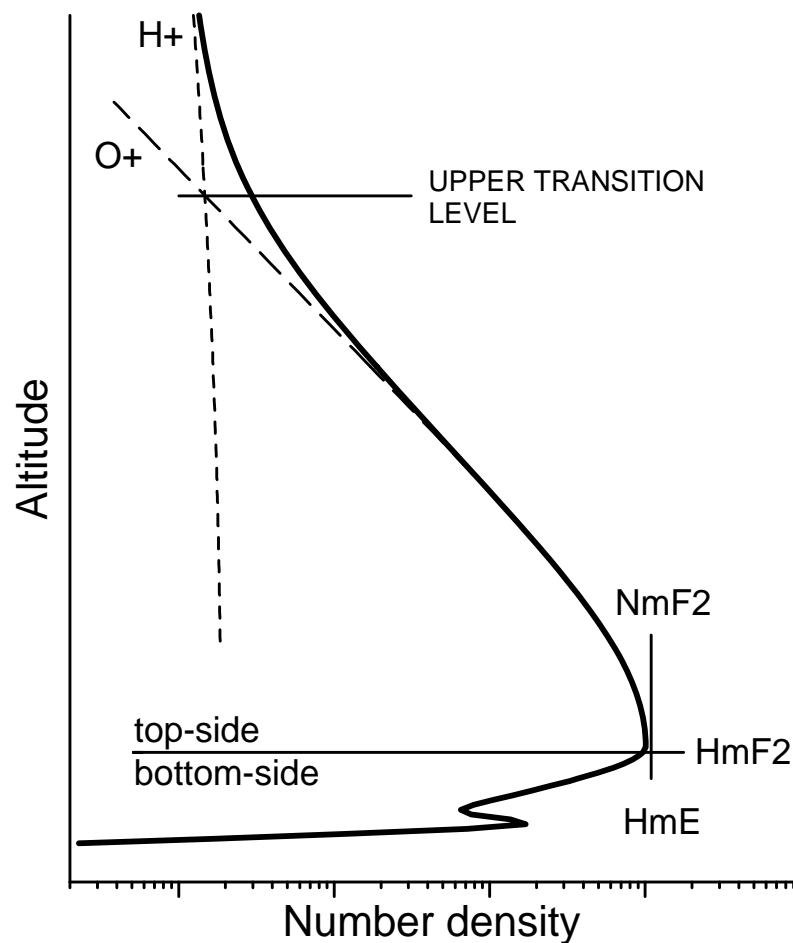


**Fig.7-1** A two-scale electron density profile (solid line):  
the topside part obtained after summing up the O<sup>+</sup> (long dashes) and H<sup>+</sup> (short dashes) ion densities.

While the ionosonde measurements are sufficient for determination of the bottom-side parameters of the profile, they do not provide information about the topside part of the profile. Even if we know the F layer peak density and height, we cannot determine the topside electron distribution because the plasma scale height is unknown. The upper transition level (if available) is the reference point we need to calculate the plasma scale height. Then, assuming an adequate topside density distribution law we can tie the profile to the F layer peak height and the O<sup>+</sup> - H<sup>+</sup> transition height. We still have to observe the fulfillment of the most important quantitative requirement - the calculated TEC ( the sum total of the integrated bottom-side and top-side electron density ) should equal the measured TEC.

## 7.1 Mathematical formulation

The total electron content is split into a bottom-side,  $TEC_b$ , and a topside,  $TEC_t$ , contents:

$$TEC = TEC_b + TEC_t = \int_0^{h_m} N_e(h) dh + \int_{h_m}^{\infty} N_e(h) dh$$

where  $N_e(h)$  is the electron density at height  $h$  and  $h_m$  is the F2 peak height.

The *bottom-side* electron profile and corresponding *bottom-side* electron content are reliably calculated from foF2, M<sub>3000</sub>F2 and foE using established methods and models (Dudeney 1978, Dudeney 1983, Di Giovanni and Radicella 1990).

This study is focused on the determination of the *topside* electron profile, presented as a sum of its major constituent oxygen and hydrogen ion density profiles. Further, the individual (oxygen and hydrogen) ion density distributions are approximated by the hyperbolic secant function in the following manner:

$$N_i(h) = N_i(h_m) \operatorname{sech}^2\left(\frac{h-h_m}{2H_i}\right) \quad (1)$$

where  $N_i(h)$  is the ion ( $O^+$  or  $H^+$ ) density at height  $h$ ,  $H_i$  is the ion scale height, and  $\operatorname{sech}(h) = 1/\cosh(h)$ ,  $\cosh(h) = 0.5(\exp(h) + \exp(-h))$ . Therefore, the following formula is proposed for calculation of the topside electron density profile:

$$N_e(h) = N_{O^+}(h_m) \operatorname{sech}^2\left(\frac{h-h_m}{2H_{O^+}}\right) + N_{H^+}(h_m) \operatorname{sech}^2\left(\frac{h-h_m}{32H_{O^+}}\right), \quad h > h_m \quad (2)$$

where  $H_{O^+}$  is the  $O^+$  scale height. The first term on the right represents the  $O^+$  vertical distribution, while the second term represents that of  $H^+$ . If we consider an isotropic ionosphere and plasmasphere (constant electron temperature), then the scale heights of  $O^+$  and  $H^+$  along the magnetic field lines will have a ratio 1:16. Here we neglect the fact that  $H^+$  has a maximum above the transition height and assume that  $H^+$  decreases exponentially from the level of  $h_m$ . This is true at altitudes well above the transition height.  $N_{O^+}(h_m)$  and the virtual quantity  $N_{H^+}(h_m)$  are the respective densities at the height of the F2 peak. To obtain the profile on the vertical direction,  $z$ , we use the simple conversion  $dz = \sin I ds$ , where  $ds$  is the differential element along the field lines,  $I$  is the inclination. If we ignore the displacement of the geographic and magnetic poles, then  $dz = \sin[\arctg(2tg\varphi)]ds$ , where  $\varphi$  is the latitude (Chapman, 1963). Denoting  $V = \sin[\arctg(2tg\varphi)]$ , equation (2) takes the form

$$N_e(h) = N_{O^+}(h_m) \operatorname{sech}^2\left(\frac{h-h_m}{2H_{O^+}}\right) + N_{H^+}(h_m) \operatorname{sech}^2\left(\frac{h-h_m}{32VH_{O^+}}\right), \quad h > h_m \quad (3)$$

There are three unknown variables in the proposed formula - the oxygen and hydrogen ion densities at the peak height, i.e.  $N_{O^+}(h_m)$  and  $N_{H^+}(h_m)$ , and the oxygen ion scale height  $H_{O^+}$ . These unknowns are determined in the following way.

After integrating  $N_e(h)$  from  $h_m$  to infinity, the above 'reconstruction' formula (3) becomes

$$\int_{h_m}^{\infty} N_e(h) dh = \int_{h_m}^{\infty} N_{O^+}(h_m) \operatorname{sech}^2\left(\frac{h-h_m}{2H_{O^+}}\right) dh + \int_{h_m}^{\infty} N_{H^+}(h_m) \operatorname{sech}^2\left(\frac{h-h_m}{32VH_{O^+}}\right) dh \quad (4)$$

hence

$$TEC_t = 2H_{O^+} N_{O^+}(h_m) + 32VH_{O^+} N_{H^+}(h_m) \quad (5)$$

Denoting,  $N_{O^+}(h_m) + N_{H^+}(h_m) = N_m F2$ , we get from equation (5) the following expressions for the peak densities:

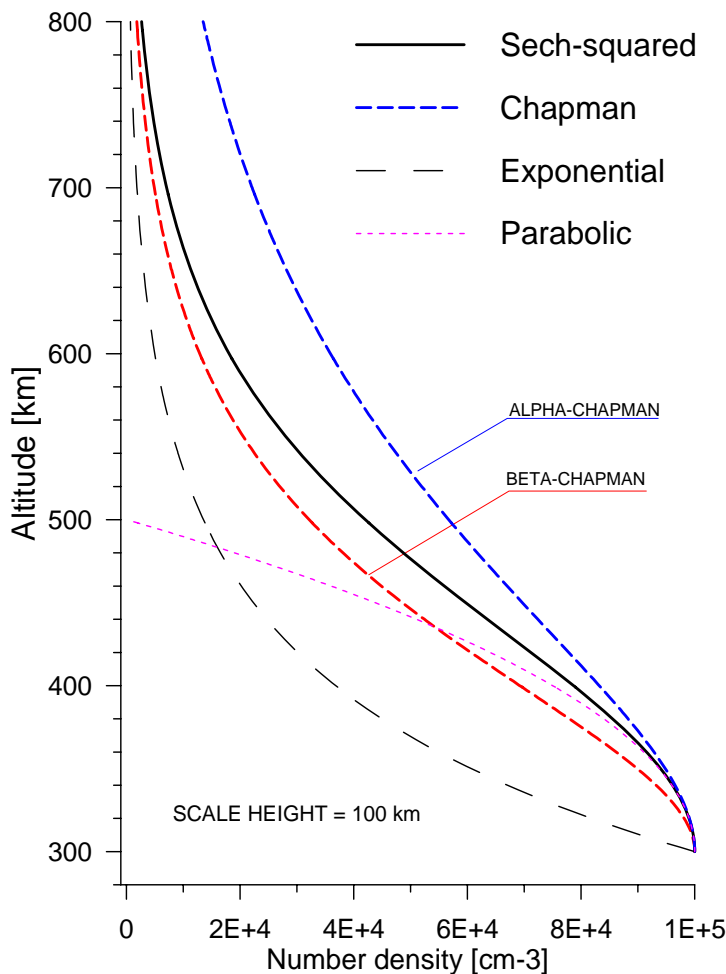
$$N_{O^+}(h_m) = \frac{16V}{(16V-1)} N_m - \frac{1}{2(16V-1)H_{O^+}} TEC_t \tag{6}$$

$$N_{H^+}(h_m) = \frac{1}{2(16V-1)H_{O^+}} TEC_t - \frac{1}{16V-1} N_m \tag{7}$$

Considering the assumed type of the topside profile (1), and expressions (6) and (7), the following equation is constructed, denoting the fact that the hydrogen and oxygen ion densities are equal at the  $O^+-H^+$  transition level:

$$\left( \frac{16V}{(16V-1)} N_m - \frac{1}{2(16V-1)H_{O^+}} TEC_t \right) \operatorname{sech}^2 \left( \frac{h_{tr} - h_m}{2H_{O^+}} \right) - \left( \frac{1}{2(16V-1)H_{O^+}} TEC_t - \frac{1}{16V-1} N_m \right) \operatorname{sech}^2 \left( \frac{h_{tr} - h_m}{32VH_{O^+}} \right) = 0$$

The upper transition level,  $h_{tr}$ , is determined from a model (Stankov, 1994; Kutiev et al. 1994). The only unknown variable in the above transcendental equation is the oxygen ion scale height, which is obtained after numerically solving the equation.



Several analytical models of the ionospheric F-region are traditionally used for numerical modelling and radio propagation work. Some of them can be very useful for the above profile reconstruction: Exponential, Sech-squared, Chapman, and Parabolic layers. These layers produce different (in shape) top-side density profiles which is demonstrated in Fig.7-2 for given scale height ( 100 km ), maximum density (  $1.0 \times 10^5$  [cm<sup>-3</sup>] ), and height of the peak density (300km). No estimation is made so far of how good these models perform as profile reconstruction tools, particularly using GPS TEC.

The research presented here aims at investigating the opportunity of using the Exponential and Chapman layers in addition to the Sech-squared layer, and comparing the results with independent data such as satellite in-situ measurements of the ion densities.

**Fig.7-2** Comparison between vertical electron density profiles obtained with basic analytical models for a given scale height of 100km.

The *Sech-squared* (Epstein) layer is defined as:

$$N_i(h) = N_i(h_m) \operatorname{sech}^2\left(\frac{h-h_m}{2H_i}\right) \quad (2)$$

where  $N_i(h)$  is the ion ( $O^+$  or  $H^+$ ) density at height  $h$ ,  $H_i$  is the ion scale height, and  $\operatorname{sech}(h) = 1/\cosh(h)$ ,  $\cosh(x) = 0.5(\exp(x) + \exp(-x))$ . The integrals in formula (1) are solved by applying the following three successive substitutions:

$$\begin{aligned} x &= \left(\frac{h-h_m}{2H}\right); \lim_{h \rightarrow h_c} x = \frac{h_c-h_m}{2H}, \lim_{h \rightarrow h_m} x = 0 \\ y &= 2x; \lim_{x \rightarrow x_c} y = \frac{h_c-h_m}{H}, \lim_{x \rightarrow x_m} y = 0 \\ z &= \exp(y); \lim_{y \rightarrow y_c} z = \exp\left(\frac{h_c-h_m}{H}\right), \lim_{y \rightarrow y_m} z = 1 \end{aligned}$$

Thus, for the oxygen ion the solution is found by the following sequence:

$$\int_{h_m}^{h_c} N(h)dh = HN_m \int_{x_m}^{x_c} \frac{4e^{2x}}{(1+e^{2x})^2} dx = 4HN_m \int_{y_m}^{y_c} \frac{e^y}{(1+e^y)^2} dy = 4HN_m \int_{z_m}^{z_c} \frac{1}{(1+z)^2} dz = 2HN_m$$

for  $h_c \gg h_m$ , and the topside electron content becomes:

$$TEC_t = 2H_{O^+} N_{O^+}(h_m) + 2H_{H^+} N_{H^+}(h_m) \quad (3)$$

Considering the fact, that at the upper transition level  $h_{tr}$  the oxygen and hydrogen ion densities are equal, the transcendental equation then reads (Stankov et al. 2002):

$$\begin{aligned} &\left( \frac{16V}{(16V-1)} N_m - \frac{1}{2(16V-1)H_{O^+}} TEC_t \right) \operatorname{sech}^2\left(\frac{h_{tr}-h_m}{2H_{O^+}}\right) - \\ &- \left( \frac{1}{2(16V-1)H_{O^+}} TEC_t - \frac{1}{(16V-1)} N_m \right) \exp\left(-\frac{h_{tr}-h_m}{32VH_{O^+}}\right) = 0 \end{aligned}$$

The only unknown variable in the above transcendental equation is the oxygen ion scale height, which is obtained after numerically solving the equation. It is assumed that the ionosphere is isotropic, therefore the  $H^+$  scale height will be 16 times larger than the  $O^+$  scale height. The correction factor  $V$  represents the change from magnetic field line direction to vertical direction (Stankov et al., 2002).

The *Exponential* layer is defined as:

$$N_i(h) = N_i(h_m) \exp\left(-\frac{h-h_m}{H_i}\right) \quad (4)$$

where  $N_i(h)$  is the density at height  $h$ ,  $H_i$  (positive) is the ion scale height. For the oxygen ion the solution, obtained similarly as for the Sech-squared layer, is given by

$$\int_{h_m}^{h_c} N_{O^+}(h) dh = H_{O^+} N_{O^+}(h_m) \quad , \quad h_c \gg h_m.$$

The corresponding equation for obtaining the scale height is now:

$$\left(\frac{16V}{(16V-1)} N_m - \frac{1}{(16V-1) H_{O^+}} TEC_t\right) \exp\left(-\frac{h_{tr}-h_m}{H_{O^+}}\right) - \left(\frac{1}{(16V-1) H_{O^+}} TEC_t - \frac{1}{(16V-1)} N_m\right) \exp\left(-\frac{h_{tr}-h_m}{16V H_{O^+}}\right) = 0$$

The general form of the *Chapman* layer is

$$N(h) = N(h_m) \exp\left\{c \left[1 - \frac{h-h_m}{H} - \exp\left(-\frac{h-h_m}{H}\right)\right]\right\} \quad (5)$$

where  $h_m$  is the peak density height and  $H$  is the scale height,  $c$  is the type coefficient. This model has two distinct formulations – the so-called  $\alpha$ -Chapman layer ( $c = 0.5$ ) and  $\beta$ -Chapman layer ( $c = 1$ ), depending on assumptions related to the electron recombination theory (Hargreaves, 1992). The  $\alpha$ -Chapman layer assumes that the electrons recombine directly with positive ions and that no negative ions are present, i.e.  $X^+ + e \rightarrow X$ , and the lost rate is then  $L = \alpha N^2$ , where  $\alpha$  is the recombination coefficient. In the  $\beta$ -Chapman formulation, the assumption is that the electron loss is through attachment to neutral particles, i.e.  $X + e \rightarrow X^-$ , with linear loss rate  $L = \beta N$ , where  $\beta$  is the attachment coefficient. As height increases, the behaviour changes from  $\alpha$  to  $\beta$  type at a height where  $\beta = \alpha N$ .

For the  $\alpha$ -*Chapman* layer, the density at a given height is

$$N(h) = N(h_m) \exp\left\{\frac{1}{2} \left[1 - \frac{h-h_m}{H} - \exp\left(-\frac{h-h_m}{H}\right)\right]\right\} \quad (6)$$

The topside electron content is (Stankov, 2002):

$$TEC_t = 2.821 H_{O^+} N_{O^+}(h_m) + 2.821 H_{H^+} N_{H^+}(h_m) \quad (7)$$

and the equation for determining the  $O^+$  scale height is:



$$\left( \frac{16V}{(16V-1)} N_m - \frac{1}{2.821(16V-1)H_{O^+}} TEC_t \right) \exp \frac{1}{2} \left( 1 - \frac{h_{tr} - h_m}{H_{O^+}} - \exp \left( -\frac{h_{tr} - h_m}{H_{O^+}} \right) \right) -$$

$$- \left( \frac{1}{2.821(16V-1)H_{O^+}} TEC_t - \frac{1}{(16V-1)} N_m \right) \exp \frac{1}{2} \left( 1 - \frac{h_{tr} - h_m}{16VH_{O^+}} - \exp \left( -\frac{h_{tr} - h_m}{16VH_{O^+}} \right) \right) = 0$$

Similarly, for the  $\beta$ -Chapman layer the density at a given height is

$$N(h) = N(h_m) \exp \left\{ 1 - \frac{h - h_m}{H} - \exp \left( -\frac{h - h_m}{H} \right) \right\} \quad (8)$$

The topside electron content is (Stankov, 2002):

$$TEC_t = 1.718 H_{O^+} N_{O^+}(h_m) + 1.718 H_{H^+} N_{H^+}(h_m) \quad (9)$$

and the equation for determining the  $O^+$  scale height is:

$$\left( \frac{16V}{(16V-1)} N_m - \frac{1}{1.718(16V-1)H_{O^+}} TEC_t \right) \exp \left( 1 - \frac{h_{tr} - h_m}{H_{O^+}} - \exp \left( -\frac{h_{tr} - h_m}{H_{O^+}} \right) \right) -$$

$$- \left( \frac{1}{1.718(16V-1)H_{O^+}} TEC_t - \frac{1}{(16V-1)} N_m \right) \exp \left( 1 - \frac{h_{tr} - h_m}{16VH_{O^+}} - \exp \left( -\frac{h_{tr} - h_m}{16VH_{O^+}} \right) \right) = 0$$

Note that, the height  $h_c$  is practically infinity in the case of GPS measurements since the electron density above the mean height of the plasmapause contributes a negligible quantity to the integrated electron content.

The topside profiles produced by the above models tend to asymptotically approach the Exponential profile at great altitudes ( $h \gg hmF2$ ). The approaching 'speed' is different for different layers and the  $\alpha$ -Chapman is obviously the slowest (**Fig.7-2**).

The Parabolic layer is defined as  $N(h) = N(h_m) \left\{ 1 - \left( (h - h_m) / 2H \right)^2 \right\}$ , where typical values of  $H$  for the F2 region lie in the range 25 to 50 km (Dieminger et al., 1995). This layer is suitable for modelling the profile near  $hmF2$  and is helpful when extracting information from the satellite data. It is also good for constructing composite ionospheric models. However, as a reconstruction tool, used separately, it is certainly not appropriate.

### Bottom-side electron profile

The information about the bottom-side part of the profile and the electron peak density and peak height is taken from ionosonde measurements; required ionosonde parameters are the F2-layer critical frequency ( $f_oF2$ ), the propagation factor ( $M_{3000}F2$ ), and the E-layer critical frequency ( $f_oE$ ). The F2-layer peak height is estimated using the expression (Dudeney 1983):

$$hmF2 = -176 + 1470 \frac{M_{3000}F2 \left\{ (0.0196 M_{3000}F2^2 + 1) / (1.296 M_{3000}F2^2 - 1) \right\}^{1/2}}{M_{3000}F2 - 0.012 + 0.253 / (f_oF2 / f_oE - 1.215)}$$

The bottom-side thickness,  $B_{bot}$ , is calculated by (Di Giovanni and Radicella, 1990)  $B_{bot} = 0.385 N_m F2 (dN / dh)_{max}^{-1}$ , where  $(dN / dh)_{max}$  is the value of the gradient of  $N_e(h)$  at the base of the F2 layer, and it is determined by the following formula:

$$(dN / dh)_{max} [10^9 m^{-3} km^{-1}] = \exp\left(-3.467 + 0.857 \ln(f_oF2 [MHz])^2 + 2.02 \ln(M_{3000}F2)\right)$$

When F2 and E layers are both present in the ionograms, the bottom-side profile is constructed as a sum of two identical Epstein layers (Rawer, 1988):

$$N(h) = 4 N_m \exp((h - h_m) / B_{bot}) \left( (1 + \exp((h - h_m) / B_{bot}))^{-2} \right),$$

where  $N_m$  and  $h_m$  are the (F2- or E-) layer's peak density and peak height respectively. The electron density distribution at D region heights is not modelled in detail.

### Upper transition level

The relative abundance of hydrogen ions is a significant factor affecting the topside electron density profile, hence the  $O^+H^+$  transition level,  $h_{tr}$ , can be successfully utilized as a reference point. This transition level is particularly useful because: a) it is always above the F layer peak height; b) it can be determined independently (from satellite measurements). The level, is determined from a model based on satellite in-situ measurements of the individual  $O^+$  and  $H^+$  ion densities (Table 7-0). In this model (Stankov, 1994; Kutiev et al., 1994), the transition level is approximated by a multi-variable polynomial, providing convenience when referencing the level with respect to solar activity, season, local time, longitude and latitude:

$$P(C, N; X) = \sum_{i_1=1}^{n_1} \sum_{i_2=1}^{n_2} \sum_{i_3=1}^{n_3} \sum_{i_4=1}^{n_4} \sum_{i_5=1}^{n_5} C(i_1, i_2, \dots, i_5) \cdot g_1(i_1, x_1) \cdot g_2(i_2, x_2) \dots g_5(i_5, x_5)$$

where  $C = \{ C(i_1, i_2, \dots, i_5), i_m = 1, \dots, n_m \}$  are the coefficients and  $\{ g_m(i_m, x_m) \}_{i_m=1}^{n_m}$  is a system of linearly independent functions on the domain of the  $m^{\text{th}}$  parameter  $x_m$ , e.g. algebraic basis  $(1, x, x^2, \dots, x^{n_m})$ , trigonometric basis  $(1, \sin x, \cos x, \dots, \sin n_m x, \cos n_m x)$ , etc. The method of least-squares fit is applied for determining the coefficients.

Model values of the  $O^+He^+$  transition level (Stankov, 1999; Stankov, 2000) can also be implemented in the reconstruction procedure. However, new formulae have to be deduced to include two more unknowns – the  $He^+$  scale height ( $H_{He^+}$ ) and maximum density ( $N_{H^+}(h_m)$ ).

Dec. solstice 00:00 LT (R=50)							June solstice 00:00 LT (R=50)								
MLat	0	60	Long		180	240	300	MLat	0	60	Long		180	240	300
60	754	754	754	754	754	754	754	60	824	824	824	824	824	824	824
50	740	735	741	741	751	745	50	765	770	765	771	775	780	780	
40	705	720	724	720	705	705	40	725	730	730	735	739	739		
30	645	650	653	646	645	645	30	714	726	732	730	727	726		
20	625	627	628	632	625	625	20	718	714	714	712	710	714		
10	715	715	715	713	711	709	10	749	745	745	745	745	745		
0	765	765	765	765	765	765	0	766	762	762	762	762	762		
-10	750	750	750	750	754	750	-10	750	748	754	754	754	752		
-20	724	722	720	724	728	724	-20	690	690	690	692	693	697		
-30	715	713	710	709	702	709	-30	635	635	635	640	643	636		
-40	730	735	739	739	725	730	-40	670	670	670	685	689	685		
-50	775	781	785	790	775	780	-50	725	719	716	709	715	715		
-60	824	824	824	824	824	824	-60	754	754	754	754	754	754		

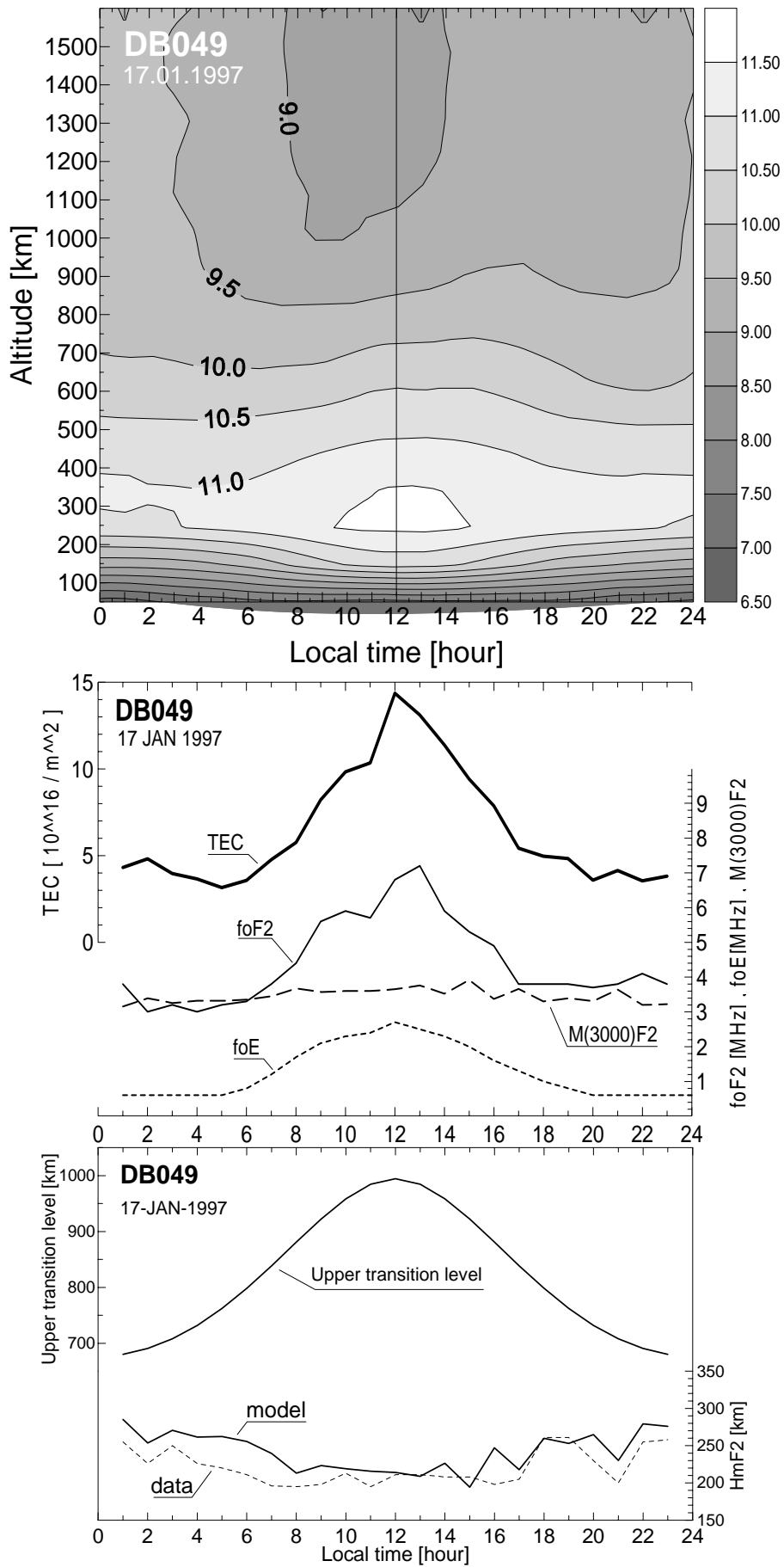
Dec. solstice 00:00 LT (R=100)							June solstice 00:00 LT (R=100)								
MLat	0	60	Long		180	240	300	MLat	0	60	Long		180	240	300
60	910	910	910	910	910	910	60	1100	1100	1100	1100	1100	1100	1100	
50	880	900	900	908	916	917	50	922	912	902	922	942	932		
40	721	729	731	736	736	738	40	950	940	930	940	950	950		
30	672	679	682	685	685	689	30	1011	991	981	976	971	991		
20	667	660	660	653	653	660	20	1040	1030	1030	1025	1020	1030		
10	687	680	680	680	680	680	10	1049	1039	1039	1039	1039	1039		
0	1000	1000	1000	1000	1000	1000	0	1050	1040	1040	1040	1040	1040		
-10	1080	1090	1090	1090	1090	1090	-10	1028	978	948	948	948	988		
-20	1050	1050	1050	1070	1070	1070	-20	686	686	686	726	766	726		
-30	1000	1000	1000	1020	1030	1030	-30	660	660	660	695	730	690		
-40	970	970	970	1030	1040	1040	-40	731	731	731	811	881	811		
-50	1060	1060	1060	1070	1080	1080	-50	998	898	848	938	998	998		
-60	1100	1100	1100	1100	1100	1100	-60	1100	1100	1100	1100	1100	1100		

12:00 LT				
MLat	R=100	R=100	R=50	R=50
	JUN	DEC	JUN	DEC
60	1430	1363	1200	1100
50	1420	1293	1189	1092
40	1380	1224	1152	1061
30	1300	1200	1085	1002
20	1250	1190	995	973
10	1200	1170	950	948
0	1150	1150	940	936
-10	1170	1200	949	945
-20	1180	1250	978	962
-30	1200	1330	1014	1011
-40	1220	1380	1070	1100
-50	1293	1420	1095	1175
-60	1363	1430	1100	1200

**Table 7-0** The O<sup>+</sup>-H<sup>+</sup> transition level model : a part of the in-situ measurement database ( Kutiev et al., 1994).

The procedure is demonstrated and tested on actual GPS TEC and digital ionosonde data obtained at the RMI Geophysics Centre. The input values of the GPS TEC, vertical sounding measurements of foF<sub>2</sub>, M(3000)F<sub>2</sub> and foE, are given in the middle panel of **Fig.7-3**. The TEC and foF<sub>2</sub> show strongly-correlated diurnal behaviour; both quantities increase sharply in the early morning, reach their absolute maximum around noon, and then start gradually decreasing. Relatively high values are maintained throughout the afternoon, followed by a 10% increase in the early evening. After that, both TEC and foF<sub>2</sub> fall rapidly to their corresponding absolute minima observed at 0200-0300LT. In the bottom panel, the F<sub>2</sub>-peak-density and O<sup>+</sup>-H<sup>+</sup> ion transition level are also provided. The level, starting from 680 km at midnight, increases up to 1000 km at noon and then decreases in a symmetrical fashion during the second half of the day. The h<sub>m</sub>F<sub>2</sub> has highest values at midnight (around 400 km) and lowest values during day (varying between 300 and 330 km). The reconstructed electron density distribution is plotted in the top panel of **Fig.7-3**. Notice the detailed vertical distribution above the h<sub>m</sub>F<sub>2</sub>. It is easy to detect the changes in the calculated topside scale height and the resulting density distribution as they develop during this particular 24-hour period.



**Fig.7-3** Diurnal behaviour reconstruction: vertical electron density (log scale,  $m^{-3}$ ) (top panel), GPS TEC and ionosonde measurements (middle panel), upper transition level model (bottom panel).

## 7.2 Evaluation of analytical models used in electron profile reconstruction

Density profiles, obtained by the analytical models described in the previous section, will be compared with independent measurements. Relatively good altitude profiles of ion densities can be obtained from the Atmosphere Explorer - C (AE-C) satellite in-situ measurements (Kutiev and Stankov, 1994; Kutiev and Stankov, 1996; Stankov, 1996b; Stankov, 1996c). The satellite was launched on 13/12/1973 in an elliptical orbit (inclination  $68.1^\circ$ ) collecting a large data base of ionospheric and thermospheric densities, temperatures, winds, and emissions within the altitude range of 130 - 4300 km. After the first eight months, the mode was changed and the spacecraft was kept in a circular orbit for the rest of its lifetime (re-entry date 12/12/1978): from March 1975 to December 1976 at about 300 km height, and from December 1976 to December 1978 at about 400 km height.

The  $O^+$  and  $H^+$  ion density data used here are obtained during the first 16 months of the AE-C mission, from 16/12/1973 to 21/3/1975 when the solar activity was low,  $F_{10.7} \approx 85$  [ $W/m^2/Hz$ ]. The measurements are from both the Bennett and Magnetic ion-mass spectrometers. Three seasons are considered - winter, equinox, and summer, defined as 91 day periods centred on the 356, 81 and 264, 173 day of year respectively. Day-time and night-time conditions are investigated using data from variable local time ranges (windows) depending on the season. Larger day-time windows (08:00-17:00) are used for summer values and larger night-time windows (19:00-05:00) are applied on the winter data. Middle geomagnetic latitudes ( $20-50^\circ N$ ) and the Northern hemisphere will be only presented. Averaged profiles are provided in **Fig.7-4** and **Fig.7-5** for  $O^+$  and  $H^+$  densities.

In order to test the analytical models against the actual data, some basic density profile characteristics should be extracted from the averaged data. Particularly important for the unique determination of a profile are the F2-layer density maximum and height and also the  $O^+$ - $H^+$  transition level (UTL). These characteristics can be determined in the way described below.

The first important characteristics to extract are the density peaks and their heights for both the  $O^+$  and electron density profiles. If quality data is available the extraction is straightforward, otherwise, the parabolic layer can be used to fit the data near the F2-layer density maximum.

The next important parameter to be extracted from the data is the  $O^+$  ion scale height,  $H_{O^+}$ . The scale height is defined as the vertical distance in which the concentration changes by a factor of  $e$  ( $e \approx 2.718286$ ). This definition allows the extraction of the scale height from the average satellite measurements. The scale height varies with height but at this stage of developing the method it is assumed to be constant. Because of this assumption, it is important to deduce the scale height from the area immediately above  $H_m F_2$  which contributes most to the TEC value. The curvature of the  $O^+$  density profile does not allow the determination to begin from  $H_m F_2$  so it starts from an altitude  $h_m F_2 + h_e$ , where  $h_e$  is approximately the half thickness of the fitting parabola. Measurement data is in abundance in this region and the scattering is generally small.

The propagation factor  $M(3000)F_2$  is obtained after fitting the satellite data with Epstein layer functions. The E-layer critical frequency,  $f_oE$ , is set to zero during night and the day-time values are set to some plausible values for the season and local time at the corresponding latitude. For the purpose of this study the precise determination is not important as the bottom-side electron profile is fitted with the same Epstein layer that is used in the reconstruction technique.

The  $O^+$ - $H^+$  transition height is relatively easy to determine during night when  $O^+$  scale height is small. During daytime the data scattering is larger because of the strong latitude dependence on latitude. In such cases, a power approximation of the oxygen ion profile near the UTL area usually helps.

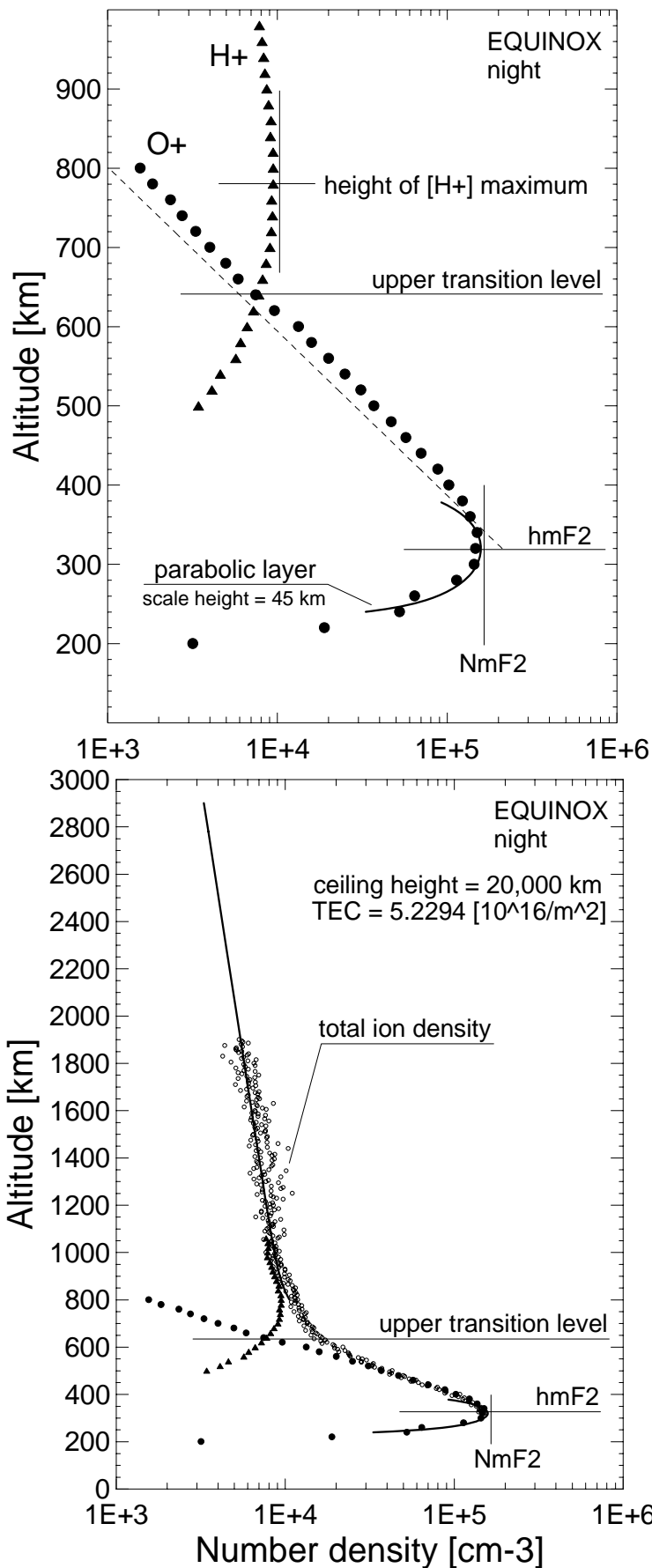


Fig.7-4 Basic profile characteristics deduced from satellite data: HmF2, NmF2, scale height, and upper transition level (top panel) and TEC value (bottom panel).

The last characteristic to determine is the total electron content value. This is done by integrating the satellite-data-based electron density profile. In all cases the electron profile has to be extrapolated to some large altitude. For the purpose, the hydrogen ion scale height is first deduced from the available data above the H<sup>+</sup> density peak and then Exponential layer is employed to simulate the distribution up to the ceiling height of 20000 km. The profile-based TEC value is numerically integrated. Averaged altitude profiles are given in Fig.7-4 and Fig.7-5 where the symbols represent ion density averaged over 20 km in altitude. The total ion density is given with open circles for averages over 5 km. For the case in Fig.7-4 , TEC is found to be approximately  $5.2294 \times 10^{16} [m^{-2}]$ .

There are two types of tests that have been carried out to evaluate the performance of the Exponential, Sech-squared and Chapman (both  $\alpha$  and  $\beta$  type) layers as reconstruction tools. First, the vertical distribution is obtained with fixed O<sup>+</sup> scale height, peak density and peak height. It aims at comparing the overall simulation ability of the profiler. Second, given a TEC value, fixed for given season and local time, the reconstruction is performed with each profiler and the results are estimated and compared. This task aims at determining the most suitable profiler from a reconstruction point of view.

### Comparison of height distributions obtained with a same scale height

The vertical density distribution produced with equal scale height (100km) has been already provided in **Fig.7-2** for the four profiles.

In order to determine which model gives better results for the  $O^+$  density profile, all input parameters has been extracted from the averaged  $O^+$  profiles obtained from AE-C data as described in the previous section. The required parameters are: the  $O^+$  peak height ( $h_m$ ), the peak density ( $N_{O^+}(h_m)$ ), and the scale height ( $H_{O^+}$ ). The retrieved parameters are listed in **Table 7-1** for the three seasons of interests (winter, equinox, summer), and for day-time and night-time conditions.

<b>AE-C data</b>	<b>WINTER</b>	<b>EQUINOX</b>	<b>SUMMER</b>
<i>F10.7 [W/m<sup>2</sup>/Hz]</i>	80.18	84.48	90.20
<i>dipole latitude [deg]</i>	20-50°N	20-50°N	20-50°N
<b>DAY-TIME</b>			
<i>local time [hour]</i>	0800-1600	0800-1630	0800-1700
<i>N<sub>O<sup>+</sup></sub>(h<sub>m</sub>) [cm<sup>-3</sup>]</i>	4.03×10 <sup>5</sup>	4.96×10 <sup>5</sup>	4.10×10 <sup>5</sup>
<i>h<sub>m</sub> [km]</i>	245	275	280
<i>H<sub>O<sup>+</sup></sub> [km]</i>	95	130	185
<b>NIGHT-TIME</b>			
<i>local time [hour]</i>	1900-0500	2000-0430	2000-0400
<i>N<sub>O<sup>+</sup></sub>(h<sub>m</sub>) [cm<sup>-3</sup>]</i>	1.20×10 <sup>5</sup>	1.58×10 <sup>5</sup>	3.00×10 <sup>5</sup>
<i>h<sub>m</sub> [km]</i>	275	320	320
<i>H<sub>O<sup>+</sup></sub> [km]</i>	90	90	110

**Table 7-1.** The basic  $O^+$  density profile characteristics extracted from AE-C data.

The vertical ion density distributions are given in **Fig.7-5**. Same scale height was used for each season and local time conditions. Only the Sech-squared and Exponential layers are given in the figure, as the Chapman profiles repeat (in relation to the above layers) the behaviour already presented in **Fig.7-2**. It is obvious that the different profilers produce quite different altitude distributions in the F-region and therefore they will produce significant differences in the corresponding values of the total electron content. The largest contribution for the TEC value comes from the region near the peak height and it is most important to compare the performance mainly in this region.

It seems that the Sech-squared model is more suitable for describing the night-time behaviour, while the day-time behaviour is better represented by the Exponential and  $\beta$ -Chapman. The latter ensures better simulation in the region near the peak. The sech-squared and  $\alpha$ -Chapman layers generally overestimate the day-time values. If the profiles are forced to pass through a given point, i.e. given density at a given height, then the shape changes as it will be seen below.

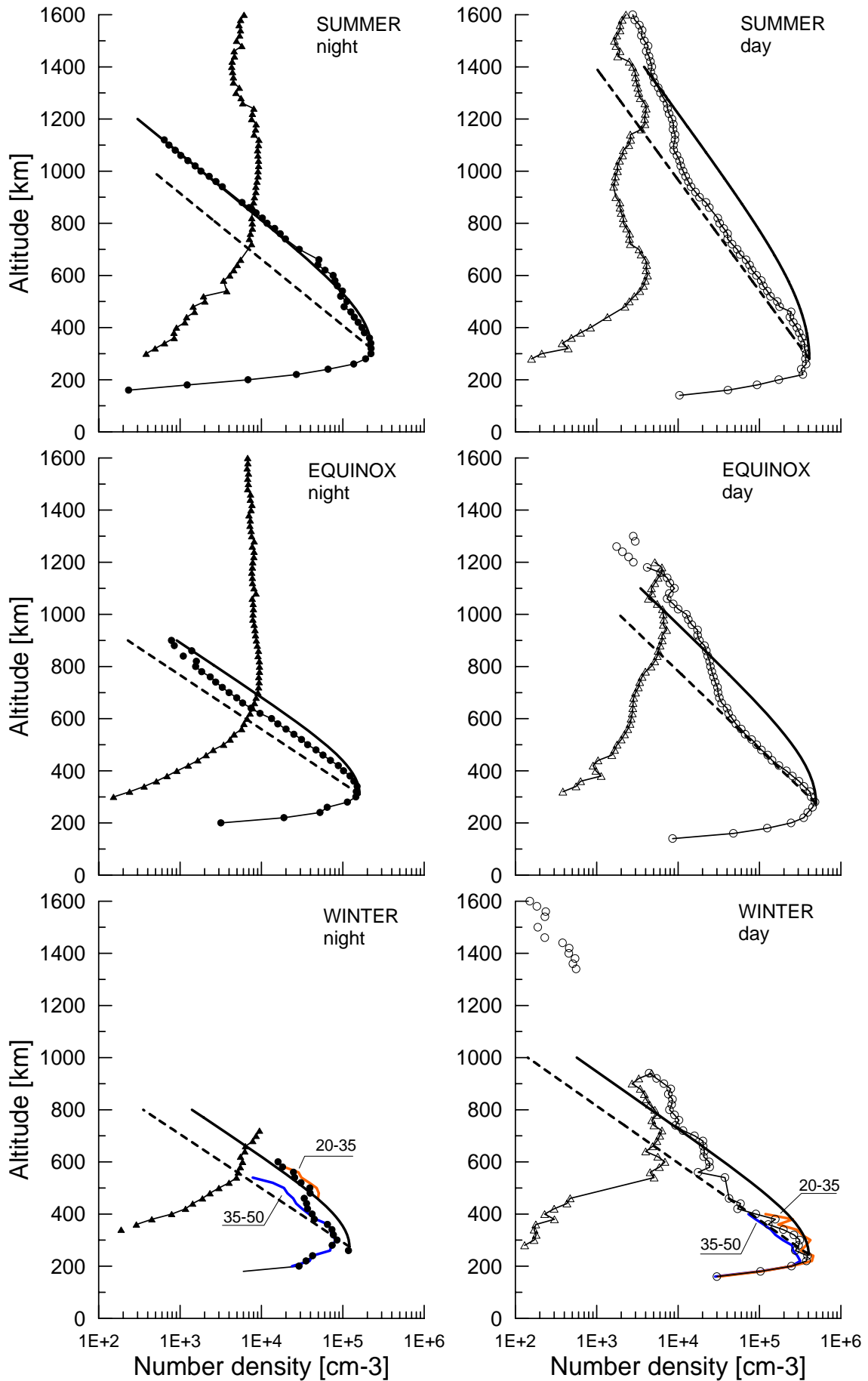


**Fig.7-5** Sech-squared (solid line) and exponential (dashed line) O<sup>+</sup> profiles compared with AE-C measurements of O<sup>+</sup> (circles) and H<sup>+</sup> (triangles) densities from the 20-50°N geomagnetic latitude range. For winter-time the averaged profiles from 20-35°N and 35-50°N are also given.



*Reconstruction using same TEC value*

The vertical ion and electron density distribution produced with equal scale height (100km) has been given in **Fig.7-2** for the four profiles. The largest values at all altitudes has been obtained with the  $\alpha$ -Chapman profiler and the smallest – with the exponential layer. In order to investigate the reconstruction quality of each profiler, it will be necessary to find out how the reconstructed profiles will look like for a fixed TEC and UTL values.

The results in the previous section suggest that in order to preserve the same TEC value, the calculated O+ scale height using the reconstruction method should be the largest if the Exponential layer is employed, and oppositely, it should be smallest if the  $\alpha$ -Chapman layer is used. In order to prove that, the method was tested for a fixed upper transition level and fixed TEC value of  $15.0 \times 10^{16}$  [m<sup>-2</sup>]. The results are given in **Fig.7-6** for UTL = 1500 km (top panel) and 1000 km (bottom panel).

As expected, the scale height, obtained via the exponential layer, is the highest:  $H_{O^+}=244$  km for UTL=1500km and  $H_{O^+}=194$ km for UTL=1000km, which in result yields much steeper electron density profile. Lowest scale height values are obtained with  $\alpha$ -Chapman: 94 and 78 km respectively. However, because of the profilers definitions and the different way of simulating the density distribution near the maximum height  $h_m$ , the reconstructed Chapman-like distributions both lie in-between the ‘boundary’ profiles obtained with the Exponential and Sech-squared profilers. Also, because of the differences at  $h_m$ , all reconstructed profiles intersect at a given altitude somewhere below UTL.

As a result of the differences in the calculated oxygen ion scale heights, significant differences are observed in the hydrogen ion density profiles – both in scale height and in absolute ion density values. This differences are increasing when increasing the upper transition level (**Fig.7-6**), which once again underline the importance of correct UTL values. The influence of the UTL on the scale-height calculations has been already analysed (Stankov et al. 2002) for the sech-squared profiler.

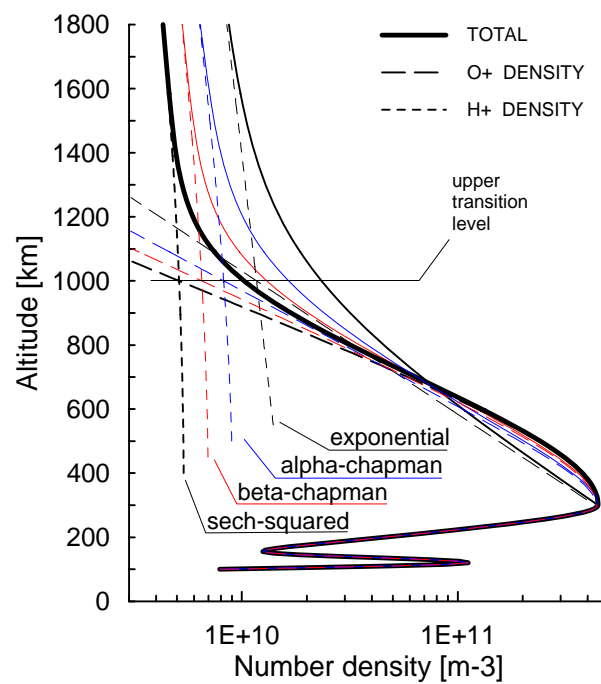
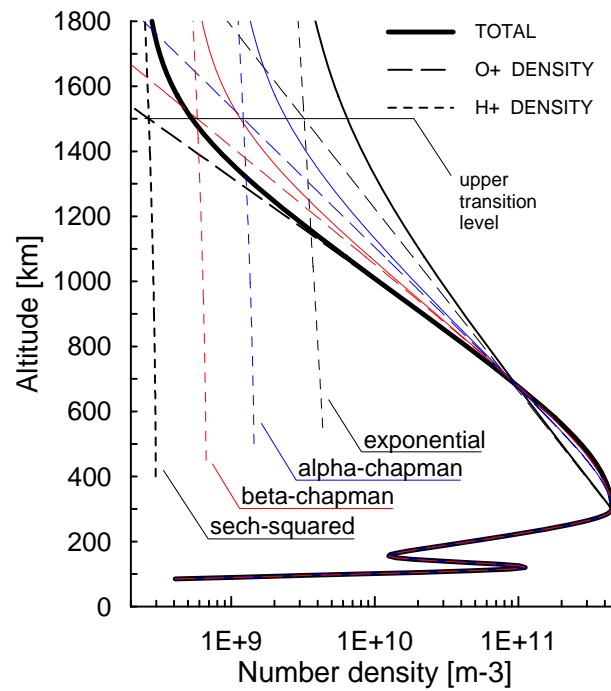


**Fig.7-6** Comparison between the vertical electron density profiles obtained with equal  $TEC = 15.0 \times 10^{16} \text{ [m}^{-2}\text{]}$  for  $UTL = 1500\text{km}$  (top) and  $UTL=1000\text{km}$  (bottom). The calculated  $O^+$  scale heights (for  $UTL=1500/1000$ ): Exponential = 244/194km, Sech-squared = 136/120km,  $\alpha$ -Chapman = 94/78km,  $\beta$ -Chapman = 157/135km.

The next step in the evaluation procedure is to deduce the density profiles using the reconstruction technique and evaluate them against averaged data profiles. The results for equinox night and day-time conditions will be discussed in more detail because the available data is more reliable.

#### *Night-time conditions*

This value and the other extracted profile characteristics (**Table 7-1**), are used to reconstruct the profiles for the four models under investigation. The results are presented in the top four panels of **Fig.7-7**. In order to better analyse the quality of the reconstruction, the relative errors are presented in the same figure for the oxygen and electron profiles. At first glance, it is obvious that no single profile is markedly better than the others when representing the altitude density distribution. The  $O^+$  profile is best modelled by the  $\alpha$ -Chapman layer at lower altitudes and equally good by the  $\beta$ -Chapman and Sech-squared profilers near the upper transition layer. The region above UTL (640km) is not so important in the case of the  $O^+$  profile. The situation is slightly different for the electron profile. Starting from HmF2, the Sech-squared and Chapman profilers demonstrate very good approximation up to about 400 km. From this altitude, up to the altitude of the ‘profile crossing’ point (560km), the Exponential layer is much better than the others. For the region above, the sech-squared layer and  $\beta$ -Chapman are the better choice. Overall, for night-time electron density distribution at equinox it is best if the Chapman profiles are used – the  $\alpha$  type at lower altitudes and  $\beta$  type for the region above the ‘profile crossing’ point. The calculated TEC is  $5.2294 \times 10^{16} [m^{-2}]$ .

#### *Day-time conditions*

The averaged  $O^+$  profiles show rather large variability in the scale height. It is mainly due to the strong altitude variations in the ion temperatures during day-time. Also, the density distribution, and consequently the  $O^+$ - $H^+$  TL, vary strongly in latitude direction, so the averaged profiles reflect these facts. In order to decrease the influence of the latitude dependence, the data has been extracted from a smaller latitude band (  $27.5^\circ - 42.5^\circ N$  ). The density scattering is still high and, the  $O^+$  and  $H^+$  profiles have been approximated. The  $O^+$  profile has been fitted (power approximation, standard deviation = 0.045) in the region from 640 to UTL (1330 km). Above the  $H^+$  profile maximum ( $\sim 1020$  km), the  $H^+$  density was again extrapolated using Exponential layer with scale height approximately 16 times larger than the  $O^+$  scale height near this altitude (1020 km). The electron density profile is calculated from the fitted  $O^+$  and  $H^+$  densities. All reconstructed profiles are given in the top four panels of **Fig.7-8**, and the relative errors using the fitted profiles are given at the bottom of the figure. During day-time, the Exponential layer is undoubtedly the best choice. It provides better overall results for the individual ion density profiles as well as for the total ion/electron density. The estimated day-time TEC value is much higher,  $12.3820 \times 10^{16} [m^{-2}]$ .

For summer conditions, the best options are the Sech-squared layer for night-time and the Exponential profiler for day-time conditions. During winter the data is scarce and highly scattered and is difficult to draw decisive conclusions. However, the winter values at least prove the necessity of a more detailed look on the reconstructed patterns in latitude direction. The results in **Fig.7-5** suggest that at lower latitudes the Sech-squared profiler provides better results at night and at higher latitudes – the Chapman profilers. The Exponential layer is again the best option for the day-time conditions.

Uncertainties in the evaluation procedure have been introduced via possible incorrect determination of TEC and also through the larger values of  $H^+$  density below the  $H^+$  peak because of the assumption for equal heights of the  $O^+$  and  $H^+$  density maxima. Additional studies are required for high-solar activity conditions.

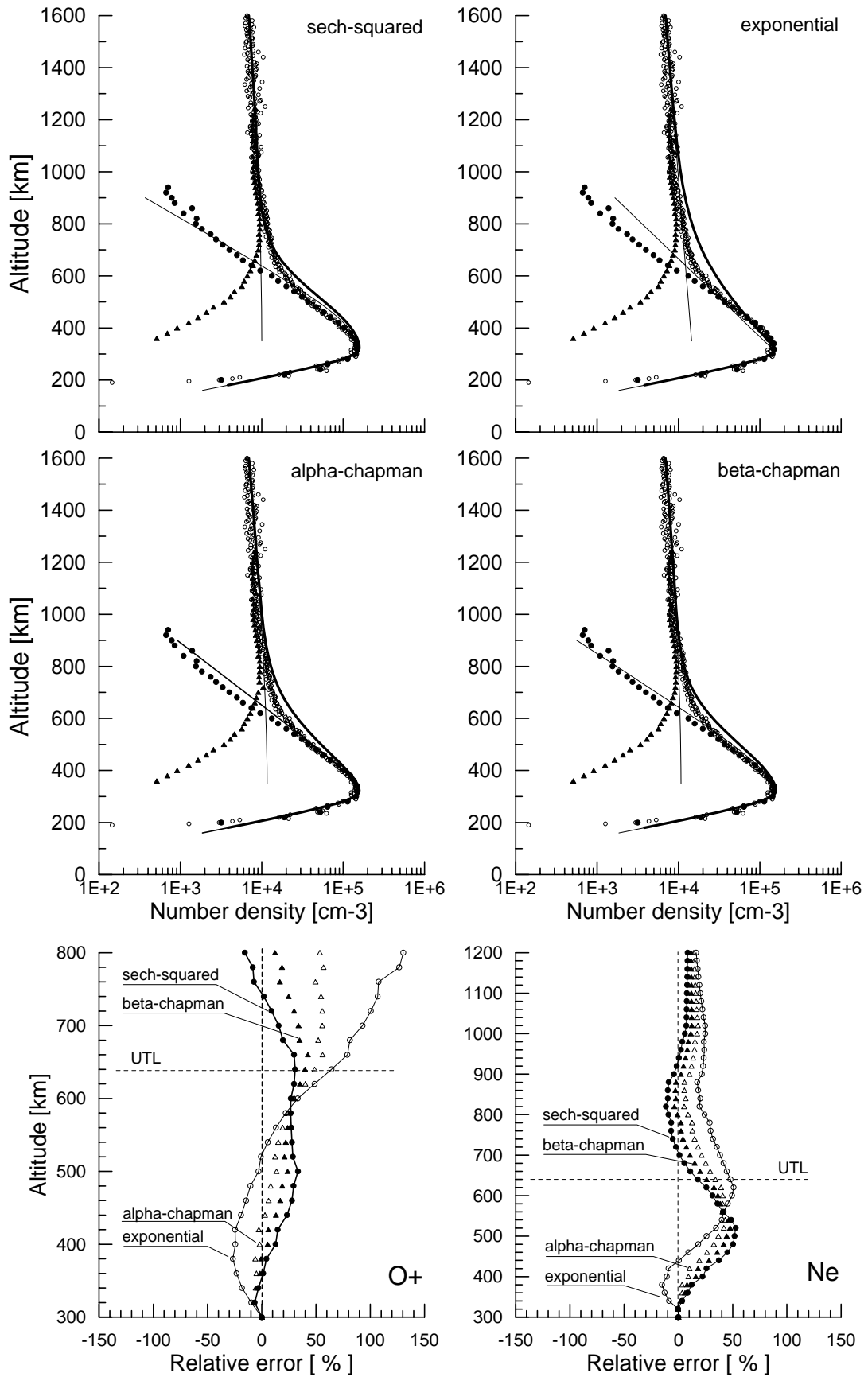


**Fig.7-7** Profile reconstruction (night-time) using Sech-squared, Exponential, and Chapman profilers; comparison with AE-C data,  $TEC = 5.2294 \times 10^{16} [m^{-2}]$ ,  $UTL = 640$  km.

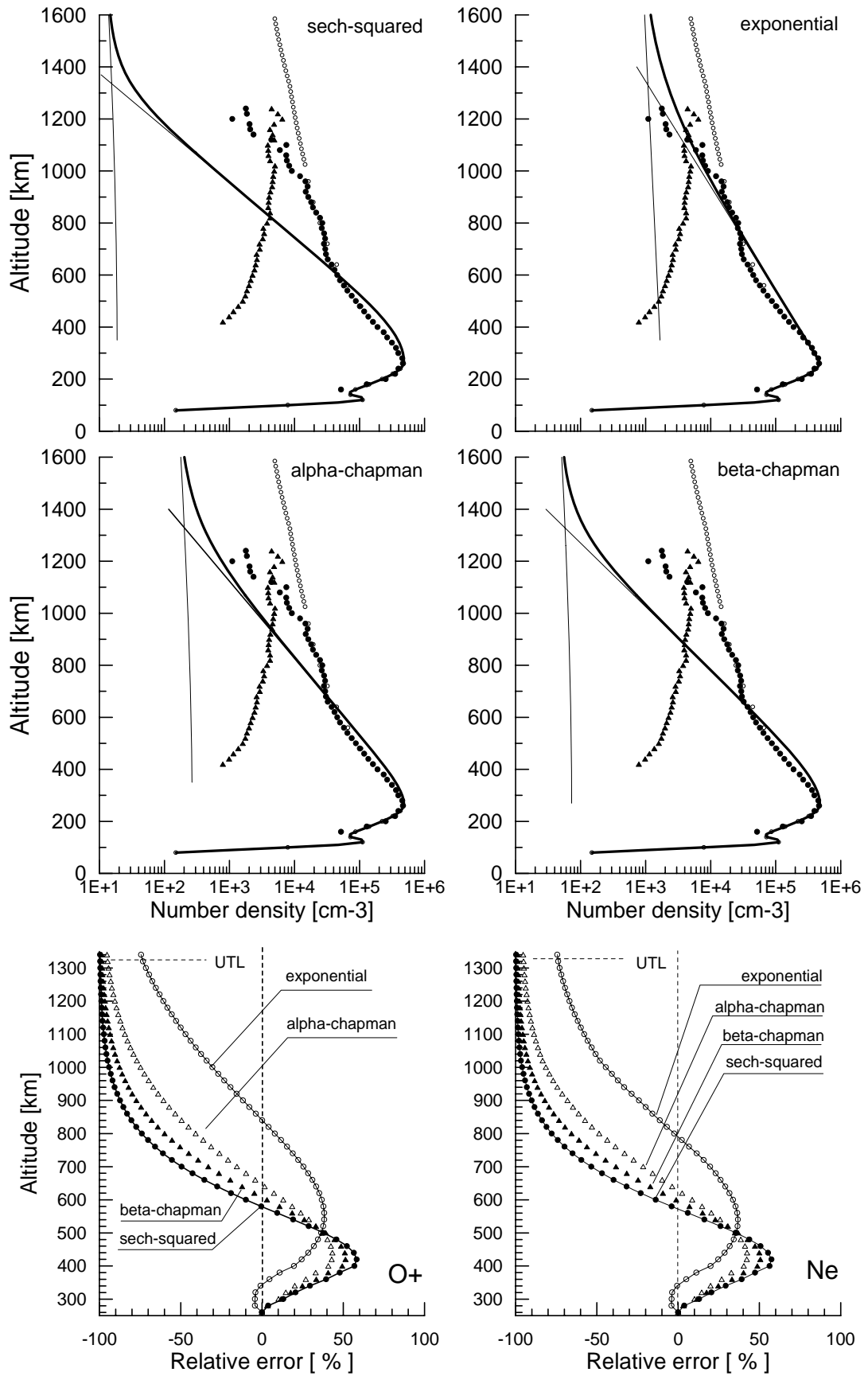


**Fig.7-8** Profile reconstruction (day-time) using Sech-squared, Exponential, and Chapman profilers; comparison with ion profiles fitted to the AE-C data,  $TEC = 12.3820 \times 10^{16} [m^{-2}]$ ,  $UTL = 1330$  km.

The reconstruction of the electron density height profile from TEC measurements, using UTL and ionosonde data, is a technique utilising different types of measurements to solve a long-lasting ionospheric physics problem. The performance of the most popular analytical ionospheric models (Chapman, Sech-squared, and Exponential) has been evaluated as they are important ingredients in the method of reconstructing the topside ion / electron density profiles. Particular care was undertaken on the calculation of the scale height in the upper ionosphere, from the F2-layer density peak height up to the  $O^+$ - $H^+$  transition level. The  $O^+$  ion scale height is the most important unknown parameter and it should be determined in the most precise way.

Follow the main conclusions:

- The Sech-squared, Exponential, and Chapman profilers can all be successfully used in the reconstruction technique. New formulae have been derived.
- No single profiler can sufficiently good represent the all spatial and temporal variations. The tests with different simple layers suggest that each of them simulate the topside ionosphere in a different manner in the upper ionosphere region, leading to significant differences that affect the TEC calculations. Differences are observed even in the altitude direction suggesting that a composite profiler should be considered.
- The density profiles produced by the Sech-squared and Chapman models tend to asymptotically approach the Exponential layer distribution at great altitudes.
- For day-time conditions, the Exponential layer is more suitable than the other profilers for modelling / reconstruction purposes.
- For night-time conditions, the Sech-squared and Chapman models guarantee better reconstruction results.
- The Parabolic layer is not suitable for reconstruction but is a very helpful tool for simulation and extraction of profile characteristics near the density maxima.
- There is a pronounced need for a high-quality ionosphere-plasmasphere temperature model which will help determining the topside scale heights much more precisely.
- The upper transition level plays a key role in the reconstruction procedure. Inaccurate values of the transition level, especially during day-time, may produce quite large errors in the topside distribution due to the high sensitivity of the  $H^+$  profile.

The reconstruction technique has the potential of a powerful research instrument and can be further improved when more measurements are available from various sources.

### 7.3 Operational model for real-time profile reconstruction

The real-time access to the top-side electron density distribution, reconstructed via the described method, widely opens the door to attacking many (old and new) problems of importance, such as the estimation and correction of the propagation delays in the Global Navigation Satellite System (GNSS), verification of empirical and theoretical ionosphere-plasmasphere models, operation of satellite augmentation systems, space weather effects on telecommunications, etc.

Presented is a new operational model for reconstruction of the ionosphere-plasmasphere vertical electron density distribution on a real-time basis. The core of such defined operational model is the novel reconstruction technique, which uses various-type of concurrent observations (GPS TEC, ionosonde, direct satellite) to reliably deduce the most adequate electron density height profile at a given location and for the time of observations. Details of this technique has been provided. Another important ingredient of the operational model is the procedure for operating the reconstruction. Apart from ‘managing’ the reconstruction, it also takes care of collecting, transferring and processing the measurement data in a fast and reliable way. Important issues in such ‘data assimilation’ procedure are data digitalization, network reliability, strict time control, etc. Details are also given further below. Tests have been already executed with actual measurements obtained at the Belgian Royal Meteorological Institute’s Geophysics Centre. Preliminary results are presented and discussed. The presented model can be upgraded for use on a global scale.

In general, the operational procedure (**Fig.7-9**) is a stand-by procedure: its execution is triggered by either a time control system or the arrival of new measurements. Thus, it relies heavily on regular influx of ionosonde, geomagnetic and TEC discrete measurement data. All types of observations should be synchronized and processed quickly, so representative results be obtained for a given location and a time. Highest flexibility, in terms of time resolution, is offered by the digital ionosonde – new measurement data are available within a delay of about 5 minutes. Longer delay is expected for receiving the GPS TEC value, because the TEC derivation procedure requires time and sufficient number of measurements. In practice, a TEC value can be obtained every 15 minutes, which is sufficient for most applications.

Several distinct stages are observed in the operational reconstruction procedure: transmission of measurement data and retrieval of input parameters, construction of the bottom- and top- side electron profile, backup and display of results. The data are transmitted using the File Transfer Protocol; the UTL values are provided by an empirical model incorporated into the reconstruction software. If the TEC value is not available on time, it is possible to use the ionosonde-based TEC value; the mean and standard deviations for low solar activity (LSA) are estimated at approximately 0.46 and 1.72 TECU (Warnant and Jodogne, 1998).

Analytical expressions are also available for hmF2. For the retrieval of the top-side electron profile, it is necessary to adopt a theoretical ‘profiler’ for the topside oxygen and hydrogen ion densities; in our case the Sech-squared layer is chosen. In the final stage of the procedure all results are stored and displayed. The next round of calculations can be triggered by either time control or arrival of new measurements.

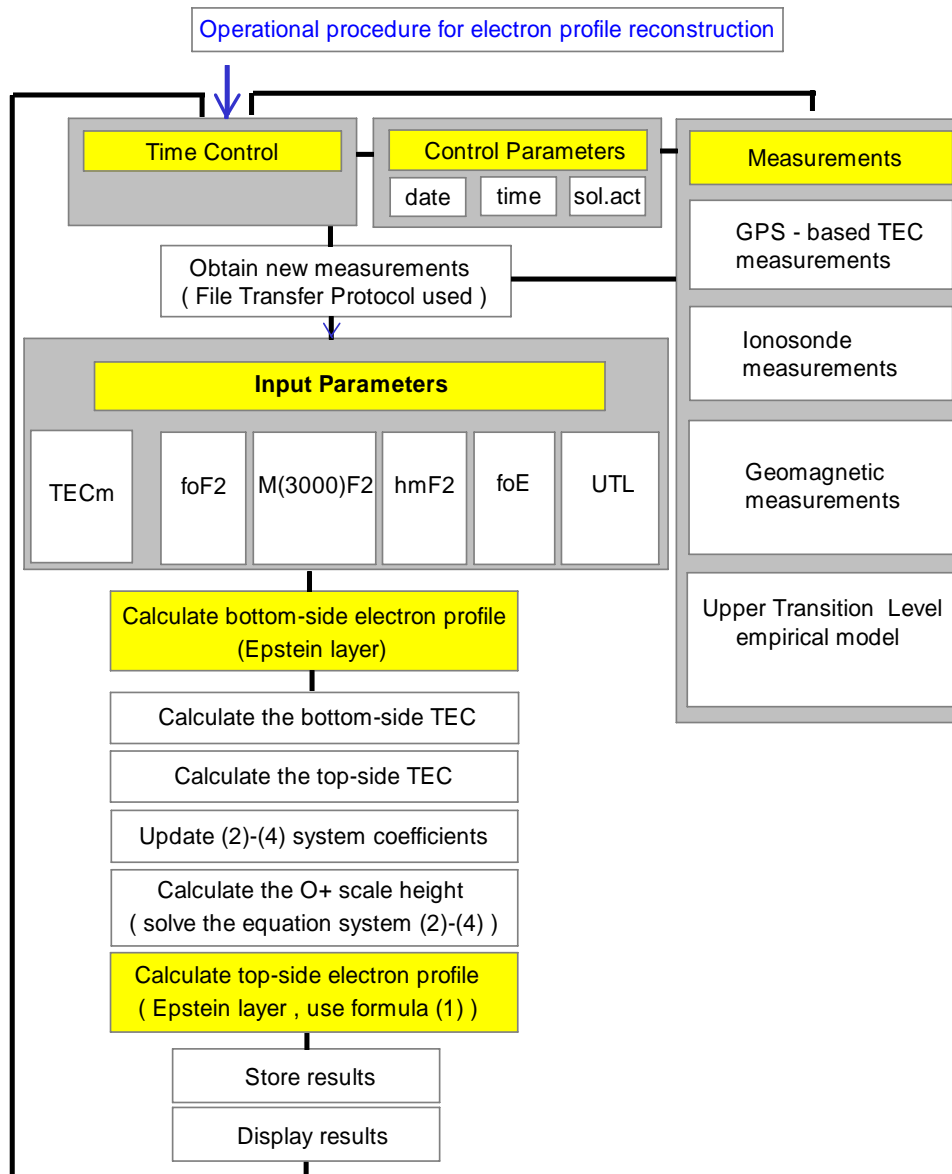


**Fig.7-9** Operational procedure for real-time reconstruction of the electron density distribution.



The new operational model, based on the presented procedure and reconstruction method, has been tested with actual hourly values of GPS TEC and ionosonde measurements acquired in real-time mode at the RMI Geophysics Centre. A trial run started at 00:00LT on 11 March 2002 and finished at 24:00LT on 17 March 2002. During this period, the solar activity was relatively high ( $176 < F10.7 < 185$ ) and geomagnetic activity conditions—quiet ( $A_p < 12$ ). Reconstructed electron profiles were ready for display well before the 15 minute time delay limit. Therefore, the model is capable of producing profiles every 15 minutes using new observations, which is a sufficiently good rate for most of the envisaged applications (storm investigation included). The results, obtained with the help of the Sech-squared profiler, are given in Fig.7-10(A,B,C,D,E). The reconstructed topside electron concentration is highly sensitive to the changes in the input parameters. For example, the sharp increase in the foF2 value near 06:00 LT on 11/03/2002 results in a sharp decrease in the slab thickness and depleted electron density above hmF2.

Considering the estimation results from Chapter 7.2, another test has been carried out on the actual data from 17 March 2002 (Fig.7-11). In this test, the Sech-squared layer was applied for night-time conditions only, while the Exponential profiler was used for the day-time hours, 07:00-19:00LT. The scale heights were calculated both ways: using Sech-squared profiler only and using Sech-squared layer for night-time and Exponential layer for daytime. The comparison of the  $O^+$  scale height calculations (Fig.7-11, bottom) confirms the previous test results, i.e. that the Exponential layer is preferable for day-time conditions. For example, at 10:00LT and 18:00LT, both  $O^+$  and  $H^+$  scale heights (deduced from Sech-squared profiler) fall below the night-time values, which is not justified considering the quiet geomagnetic conditions. The reconstruction has been executed again using the Exponential profiler for day-time conditions. The results of this run are provided for the period 11-13 March 2002 (Fig.7-12).

Local measurements of the geomagnetic field's horizontal component (H), delivered in real-time, are important for the operational reconstruction procedure. The Dst and Kp are not available operationally, so H can be used as a substitute on-line indicator of geo-magnetic storm activity. However, further investigations are required on the proper utilisation of this input parameter.

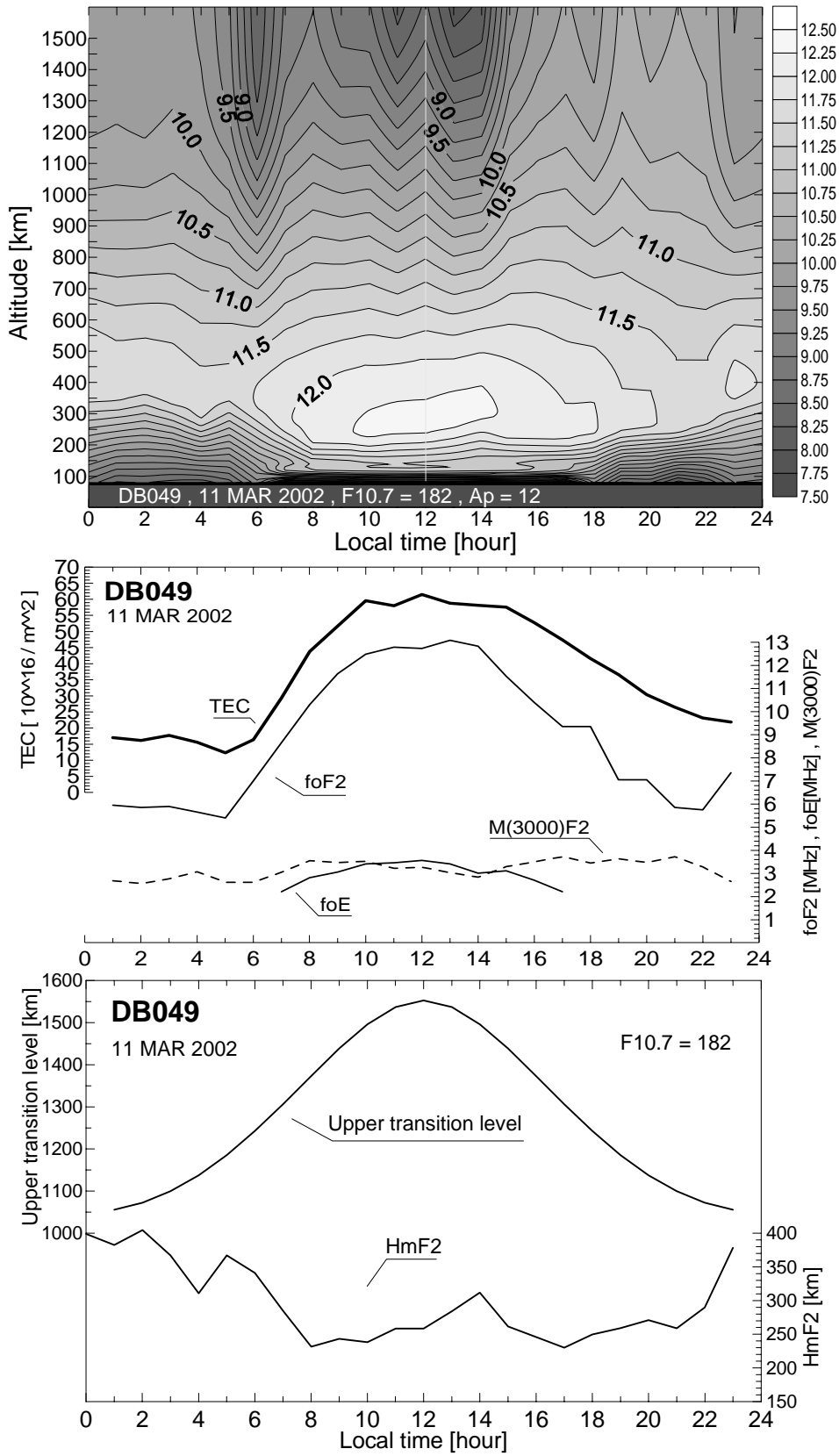


**Fig.7-10A** Operational reconstruction of vertical electron density (log scale,  $m^{-3}$ ) (top panel). The GPS TEC and ionosonde measurements are in the middle, upper transition level and hmF2 values are at the bottom.

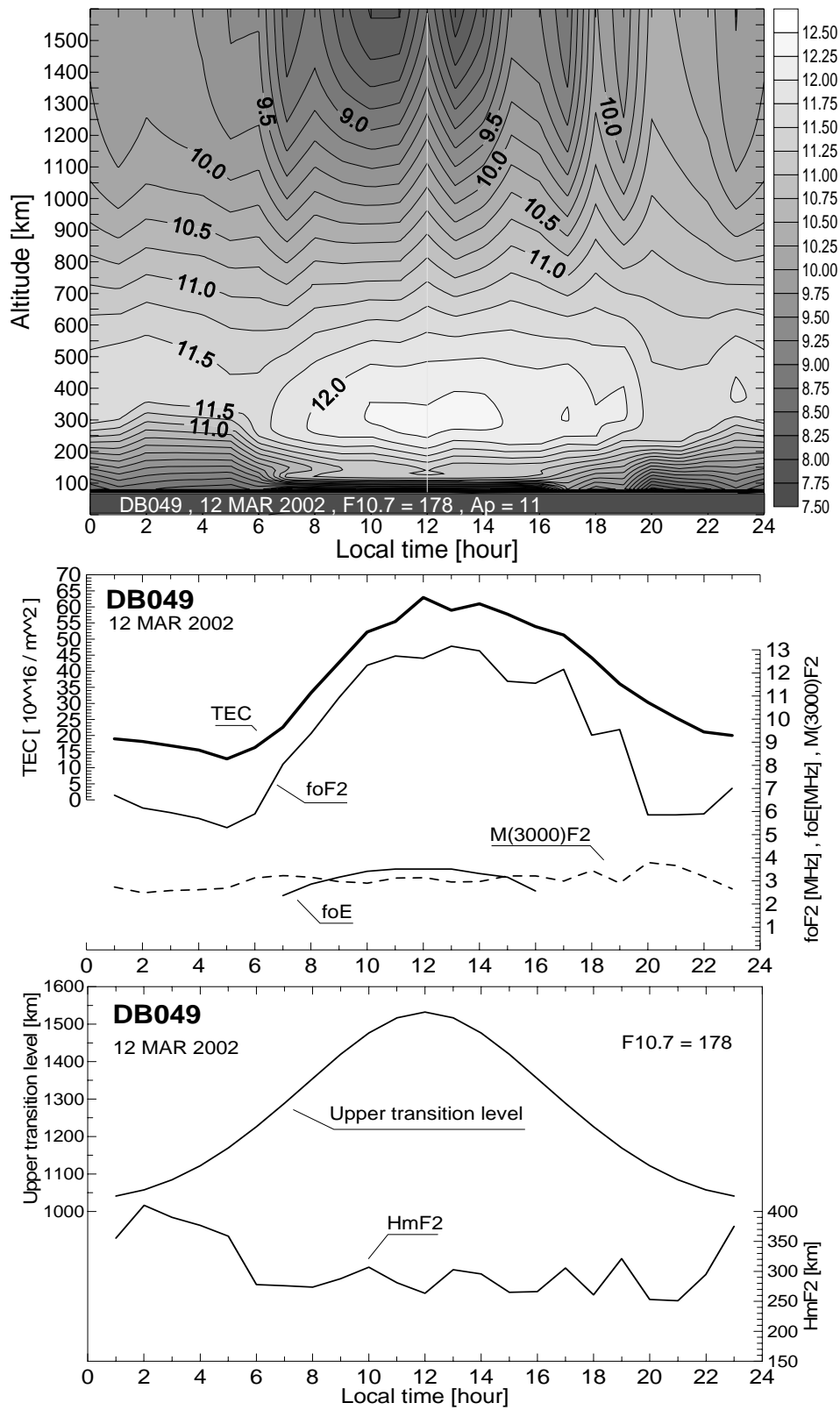


**Fig.7-10B** Operational reconstruction of vertical electron density (log scale,  $m^{-3}$ ) (top panel). The GPS TEC and ionosonde measurements are in the middle, upper transition level and hmF2 values are at the bottom.

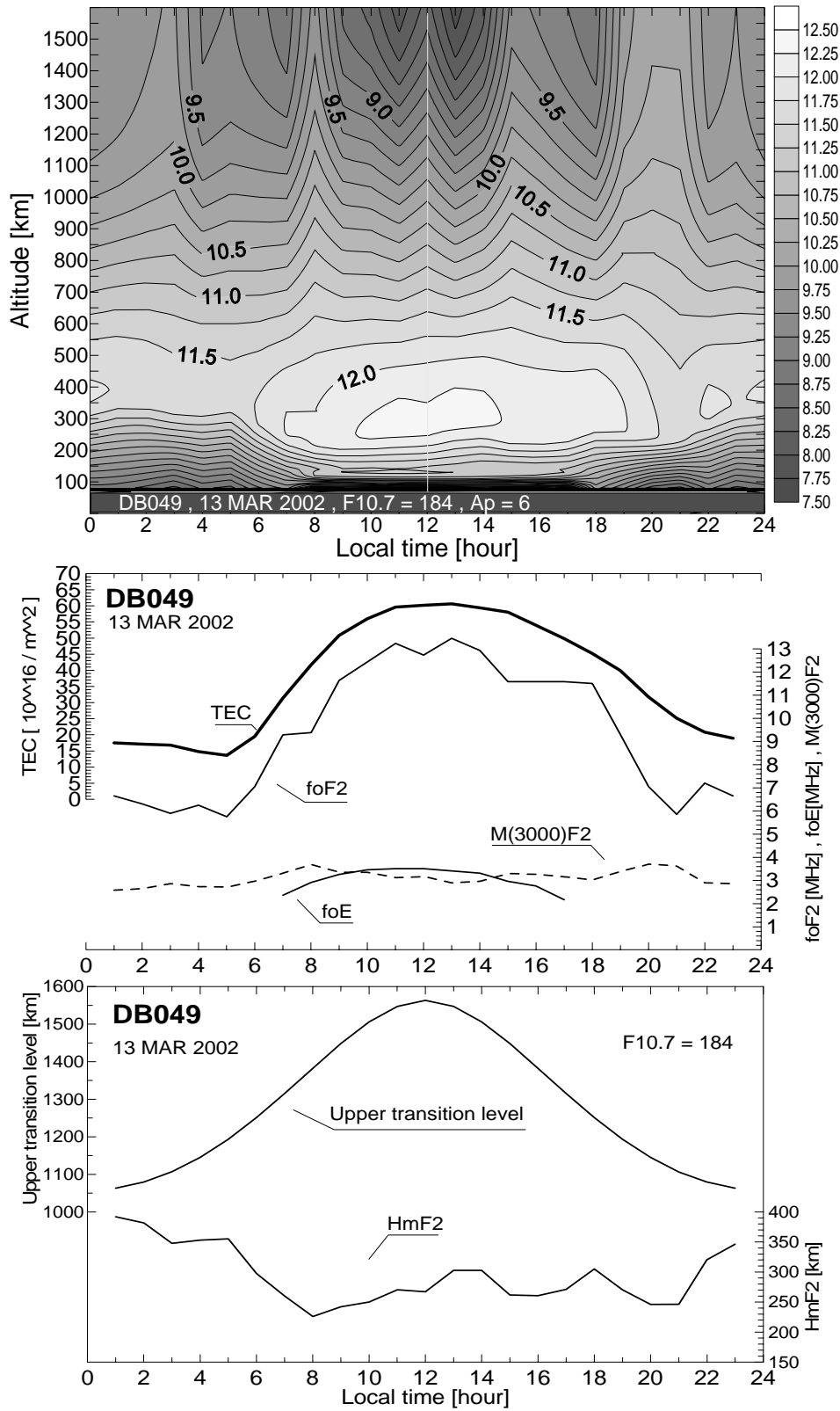


**Fig.7-10C** Operational reconstruction of vertical electron density (log scale,  $m^{-3}$ ) (top panel). The GPS TEC and ionosonde measurements are in the middle, upper transition level and hmF2 values are at the bottom.

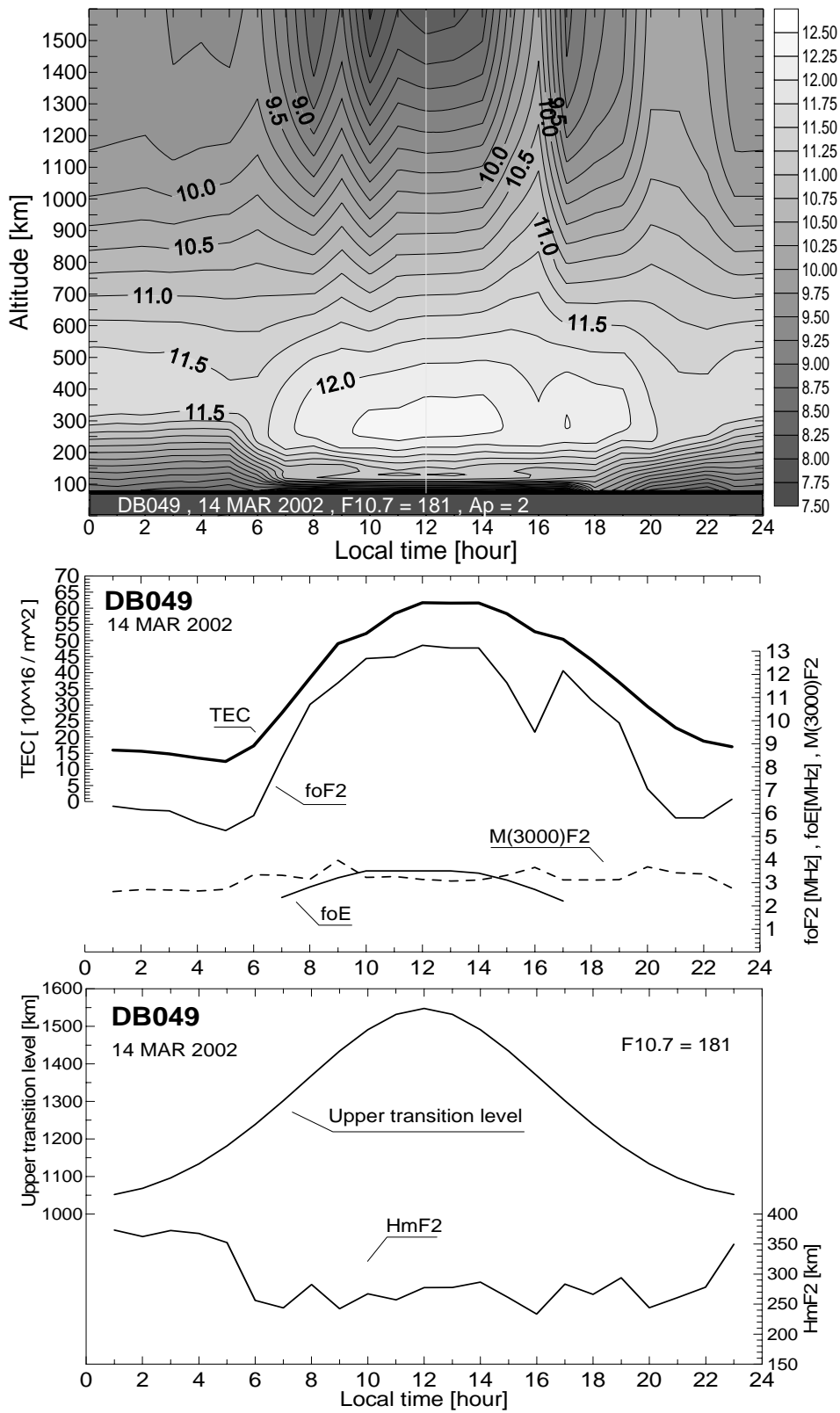


**Fig.7-10D** Operational reconstruction of vertical electron density (log scale,  $m^{-3}$ ) (top panel). The GPS TEC and ionosonde measurements are in the middle, upper transition level and hmF2 values are at the bottom.

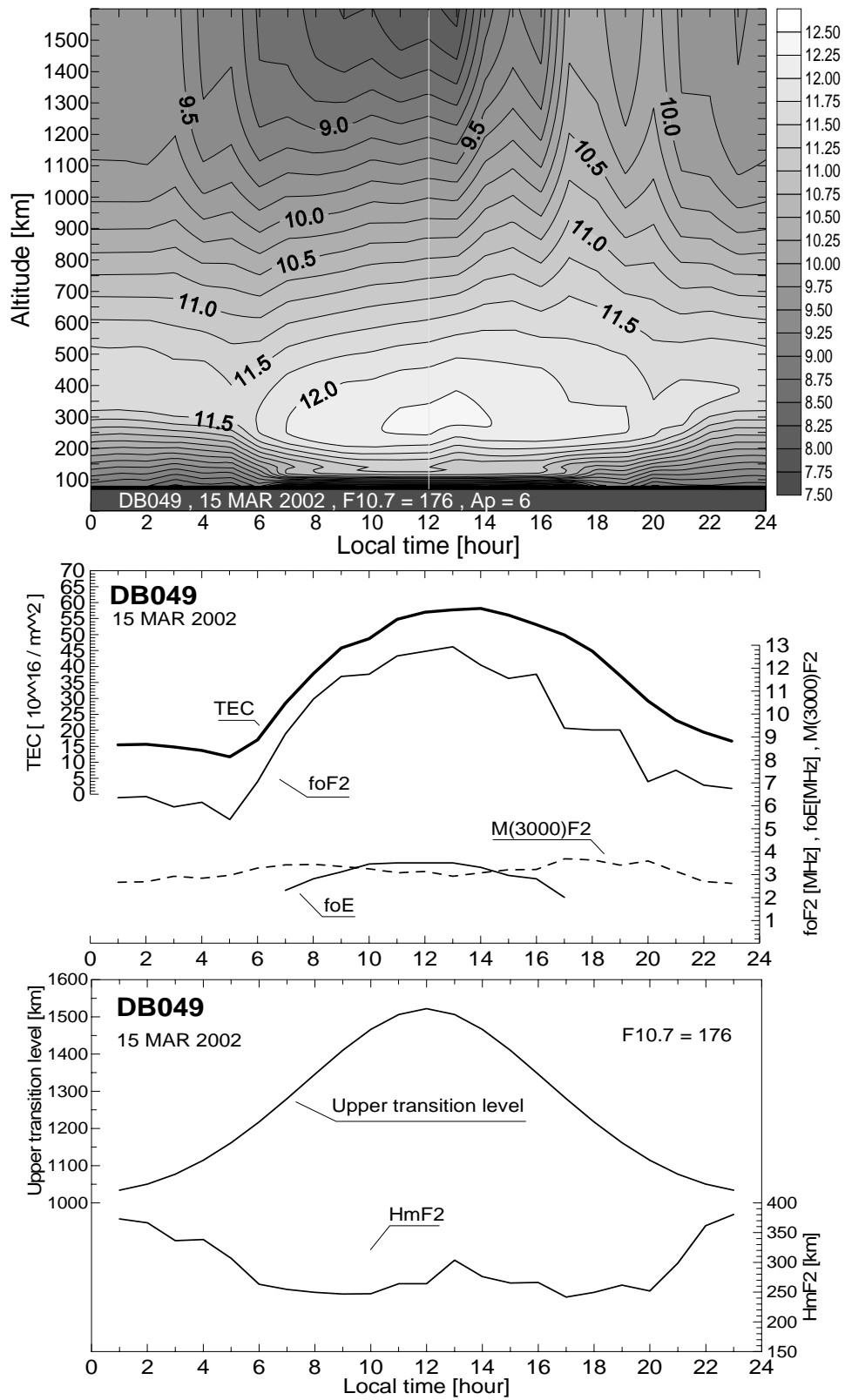


**Fig.7-10E** Operational reconstruction of vertical electron density (log scale,  $m^{-3}$ ) (top panel). The GPS TEC and ionosonde measurements are in the middle, upper transition level and hmF2 values are at the bottom.

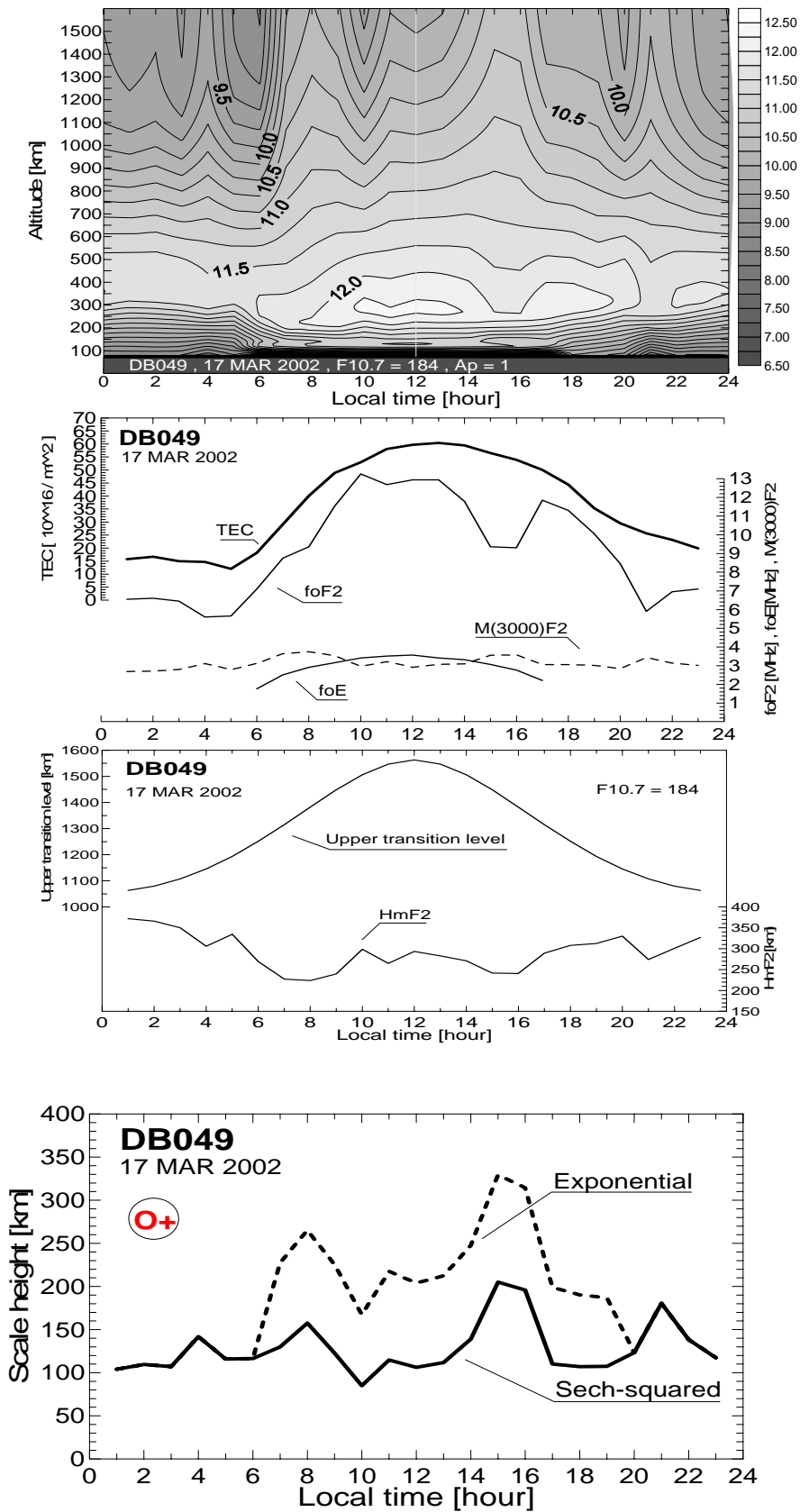


**Fig.7-11** Profile reconstruction using Sech-squared (night-time) and Exponential (day-time) profilers: top - vertical electron density (log scale,  $m^{-3}$ ), middle panels - input measurement data, bottom panel – the reconstructed oxygen ion scale height.

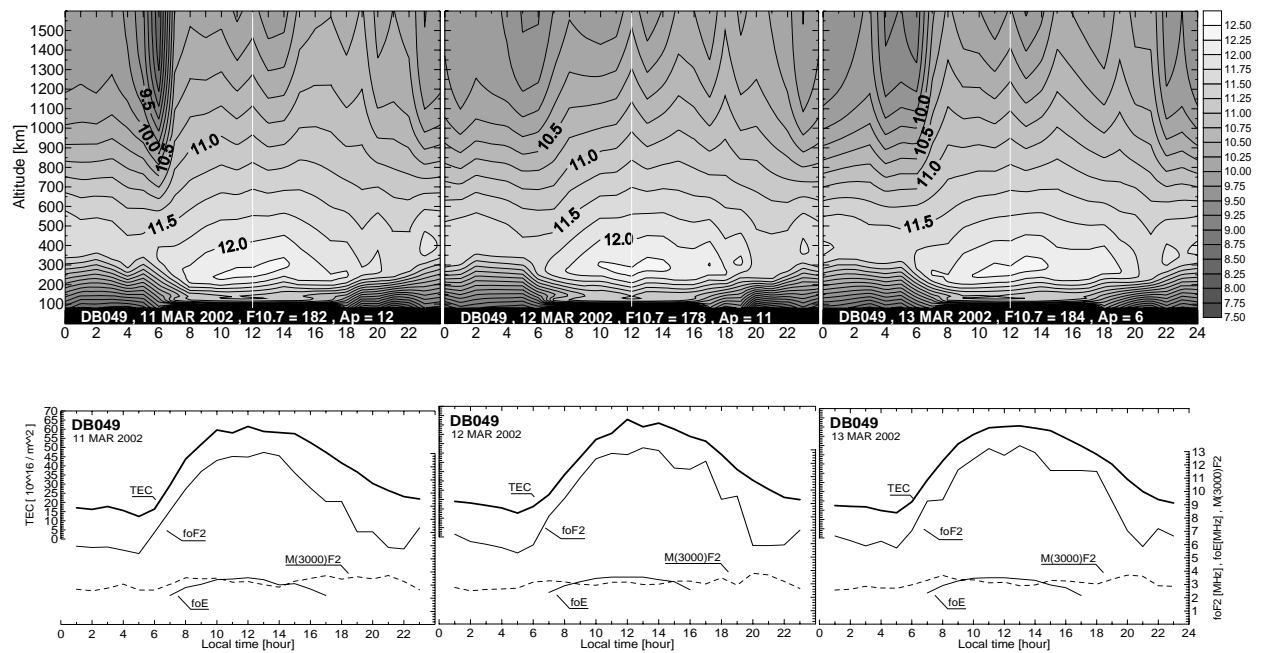


**Fig.7-12** Real-time reconstruction of the electron density profile, 11-13 March 2002, Dourbes (4.6°E, 50.1°N).

The following conclusions can be made for the reported operational reconstruction model:

- The recently-developed electron density reconstruction technique (Chapter 7.1) proved to be very useful in developing a new procedure that will allow obtaining more information on the topside electron density distribution in a real-time mode.
- The developed operational procedure is reliable, easy to maintain and upgrade. It is important that new measurements can be obtained and processed 4 times per hour, which in turn can provide higher resolution in the results.
- The operational model is suitable for investigating in detail the local ionosphere development under storm-time conditions. However, for better identifying and observing a storm, it is necessary to include geomagnetic field measurements – the horizontal component, in particular.
- A crucial advantage of the proposed model is its applicability on a global scale through the ever-growing GPS TEC and ionosonde measurements network. Data, collected at Brussels (50.8°N, 4.4°E) alone, allow the TEC computation from about 35°N to 60°N in latitude and from 20°W to 25°E in longitude.

Important applications of the operational reconstruction model are envisaged, such as test and development of ionosphere-plasmasphere models, optimisation of HF radio systems operation, investigation of ionospheric storms, and other space-weather studies.



## 8. **SUMMARY**

Presented were the most important results from the recent studies of the ionosphere-plasmasphere system response at disturbed and extreme geomagnetic activity conditions. All studies have been carried out at the Royal Meteorological Institute of Belgium with the help of the comprehensive measurement database built at the Geophysics Centre in Dourbes. This database proved to be a valuable source of high-quality and easily available digital data.

Three major topics of importance to the ionospheric response investigations were covered – case studies of storms, development of local geomagnetic activity indices for use in the short-term forecasting, and reconstruction of the vertical electron density distribution. According to each of the above subjects, the following conclusions can be made.

*Ionospheric storm studies:*

- The storm studies are much more reliable and efficient if combined ionosonde and GPS TEC measurements are used.
- Higher resolution data (e.g. every 15 min) are required for a better understanding of the dynamic ionospheric storm behaviour on a global scale.
- The local measurements of the horizontal geomagnetic field component can be used successfully as a reference for storm onset and subsequent main and recovery phases.

*Short-term forecasting of foF2 and TEC:*

- The development of local synthetic geomagnetic activity indices is of crucial importance to the foF2 and TEC short-term forecasting. Such indices are local storm-response characteristics of high precision.
- Differences are observed between the foF2 and GPS TEC behaviour response to intense magnetic activity ( $K_p > 4$ ), mainly with the detected positive response of TEC during winter in contrast with the all-negative foF2 relative deviations.

*Electron profile reconstruction:*

- A recently-developed electron density reconstruction technique can be successfully utilized in investigating the local storm-time ionosphere development.
- A new operational procedure is being developed, which will provide the reconstructed electron density on a near real-time basis.
- An advantage of the profile reconstruction method is its applicability on a global scale through the ever-growing GPS TEC and digital ionosonde measurements network.

The achieved results can be successfully applied in further research and development, such as: evaluation of the relative ionospheric correction to GPS navigation and target location, variability and correlation studies of basic ionosphere-plasmasphere characteristics, long- and short-term prediction of ionospheric parameters for use in space-weather issues, etc.

## **REFERENCES**

*This page intentionally left blank.*

- Akasofu S.I., S. Chapman (1972): *Solar-Terrestrial Physics*, Oxford University Press, Oxford.
- Banks P.M., G.Kockarts (1973): *Aeronomy*, Academic Press, New York and London.
- Buonsanto M., J. Foster, D. Sipler (1992): Observations from Millstone Hill during the geomagnetic disturbances of March and April 1990. *Journal of Geophysical Research*, Vol.97, 1225-1243.
- Chapman S. (1963): Geomagnetic nomenclature, *J. Geophys. Res.*, Vol. 68, No.4, 1174.
- Chapman S., Bartels (1940): *Geomagnetism*, Oxford University Press, Oxford.
- Davies K., G.K. Hartmann (1997): Studying the ionosphere with the Global Positioning System. *Radio Science*, Vol. 32, No.4, 1695-1703.
- De Meyer F. (1981): Mathematical modelling of the sunspot cycle. *Solar Physics*, Vol. 70, 259-272.
- Di Giovanni G., S.M.Radicella (1990): An analytical model of the electron density profile in the ionosphere. *Advances in Space Research*, Vol. 10, No. 11, (11)27-(11)30.
- Dieminger W., G.K.Hartmann, R.Leitinger (Eds.) (1995): *The upper atmosphere – data analysis and interpretation*, Springer, Berlin.
- Dudeney J.R. (1978): An improved model of the variation of electron concentration with height in the ionosphere. *Journal of Atmospheric and Terrestrial Physics*, Vol. 40, No.2, 195-203.
- Dudeney J.R. (1983): The accuracy of simple methods for determining the height of the maximum electron concentration of the F2-layer from scaled ionospheric characteristics, *Journal of Atmospheric and Terrestrial Physics*, Vol. 45, No.8/9, 629-640.
- Feichter E., R.Leitinger (1993): *Longterm studies of ionospheric electron content*.  
Wissenschaftlicher Bericht No.1/1993, Institut für Meteorologie und Geophysik, Karl-Franzens Universität, Graz.
- Fejer B.G. (1997): The electrodynamics of the low-latitude ionosphere: recent results and future challenges. *Journal of Atmospheric and Solar-Terrestrial Physics*, Vol.59, 1465-1482.
- Field P.R., H. Rishbeth, R.J.Moffett, D.W. Idenden, G.H. Millward, A.D. Aylward (1998): Modelling composition changes in F-layer storms. *Journal of Atmospheric and Solar-Terrestrial Physics*, Vol.60, 523-543.
- Foerster M., N. Jakowski (2000): Geomagnetic storm effects on the topside ionosphere and plasmasphere. *Surveys in Geophysics*, Vol. 21, 47-87.
- Fuller-Rowell T.J., D. Rees, H. Rishbeth, A.G. Burns, T.L.Killeen, R.G. Roble (1991): The composition change theory of F-region storms: A reassessment. *Journal of Atmospheric and Terrestrial Physics*, Vol.53, 797-815.
- Fuller-Rowell T.J., M.V. Codrescu, H. Rishbeth, R.J. Moffett, S. Quegan (2000): On the seasonal response of the thermosphere and ionosphere to geomagnetic storms. *Journal of Geophysical Research*, Vol.101, No.A2, 2343-2353.
- Hargreaves J.K. (1992): *The solar-terrestrial environment*. Cambridge University Press, Cambridge.
- Horwitz J.L., R.H. Comfort, P.G. Richards, C.R. Chappell, M.O. Chandler, P. Anderson, W.B. Hanson, L.H. Brace (1990): Plasmasphere-ionosphere coupling: 2. Ion composition measurements at plasmaspheric and ionospheric altitudes and comparison with modelling results. *Journal of Geophysical Research*, Vol.95, 7949-7959.

- Jakowski N. (1981): A method for analyzing ionospheric perturbations by combining ionospheric total electron content with foF2 data. *Physica Solariterr.*, Vol. 15, 130-136.
- Jakowski N. (1996): TEC monitoring by using satellite positioning systems. in: *Modern Ionospheric Science*, pp. 371-390.
- Jakowski N., M. Foerster (1995): About the nature of the nighttime winter anomaly effect. *Planetary and Space Science*, Vol. 43, 603-612.
- Jakowski N., L. Lois (1984): Investigations of ionospheric storms by combining ionospheric total electron content with foF2 data. *Gerlands Beitr. Geophysik*, Vol. 93, 1-11.
- Jakowski N., S. Schluter, E. Sardon (1999): Total electron content of the ionosphere during the geomagnetic storm on 10 January 1997. *Journal of Atmospheric and Solar-Terrestrial Physics*, Vol.61, 299-307.
- Jankowski J., C. Sucksdorff (1996): IAGA Guide for magnetic measurements and observatory practice. IAGA, Warsaw, Poland.
- Jones K.L., H. Rishbeth (1971): The origin of storm increases of mid-latitude F-layer electron concentration. *Journal of Atmospheric and Terrestrial Physics*, Vol.33, 391-401.
- Kutiev I., S.M. Stankov, (1994): Relative abundance of H<sup>+</sup> and He<sup>+</sup> in the outer ionosphere. *Advances in Space Research*, Vol. 14, No.12, (12)139-(12)141.
- Kutiev I., S.M. Stankov (1996): Review of progress in gathering, distributing and using satellite data for activities within COST 238 (PRIME). *Annali di Geofisica* , 39, No.4, 775-781.
- Kutiev I., P. Muhtarov (2001): Modelling the midlatitude response to geomagnetic activity. *Journal of Geophysical Research*, Vol.106, 15501-15510.
- Kutiev I., S.M. Stankov, P.Marinov (1994): Analytical expression of O<sup>+</sup>- H<sup>+</sup> transition surface for use in IRI. *Advances in Space Research*, Vol. 14, No.12, (12)135-(12)138.
- Kutiev I., P. Muhtarov, L. Cander, M.Levi (1999): Short-term prediction of ionospheric parameters based on auto-correlation analysis. *Annali di Geofisica*, Vol.42, 121-127.
- Matsushita S. (1967): Geomagnetic disturbances and storms, In: *Physics of the geomagnetic phenomena*, ( ed. S. Matsushita and W. H. Campbell ), pp.1153-1202, Academic Press, New York.
- Menvielle M., A. Berthelier (1991): The K-derived planetary indices: description and availability. *Reviews of Geophysics*, Vol.29, No.3, 415-432.
- Mikhailov A.A., M. Foerster (1999): Some F2-layer effects during the January 06-11, 1997 CEDAR storm period as observed with the Millstone Hill Incoherent Scatter Facility. *Journal of Atmospheric and Solar-Terrestrial Physics*, Vol.61, 249-261.
- Muhtarov P., I. Kutiev (1999): Autocorrelation method for temporal interpolation and short-term prediction of ionospheric data. *Radio Science*, Vol.34, 459-464.
- Muhtarov P., I. Kutiev, L. Cander (2001): Geomagnetically correlated autoregression model for short-term prediction of ionospheric parameters. *Inverse Problems in Physics*, Vol.17, 1-17.
- Namgaladze A.A., M. Foerster, R.Y. Yurik (2000): Analysis of the positive ionospheric response to a moderate geomagnetic storm using a global numerical model. *Annales Geophysicae*, Vol.18, 461-477.
- Parker E.N. (1967): Disturbance of the geomagnetic field by the solar wind, In: *Physics of the geomagnetic phenomena*, ( ed. S. Matsushita and W. H. Campbell ), pp.1153-1202, Academic Press, New York.

- Parkinson W.D., V.R.S. Hutton (1989): The electrical conductivity of the Earth, In: *Geomagnetism*, (ed. J.A. Jacobs), Vol.3, pp.261-322, Academic Press, London.
- Primdahl F. (1979): *The Fluxgate Magnetometer*, Geophysical Papers, R-55, Danish Meteorological Institute.
- Proelss G.W. (1993): On explaining the local time variation of ionospheric storm effect. *Annales Geophysicae*, Vol.11, 1-9.
- Proelss G.W., L.H. Brace, H.G. Mayr, G.R. Carignan, T.L.Killeen, J.A.Klobuchar (1991): Ionospheric storm effects at subauroral latitude: a case study. *Journal of Geophysical Research*, Vol.96, 1275-1288.
- Rangarajan G.K. (1989): Indices of geomagnetic activity, In: *Geomagnetism*, (ed. J.A. Jacobs), Vol.3, pp.323-384, Academic Press, London.
- Rawer K. (1988): Synthesis of ionospheric electron density profiles with Epstein functions. *Advances in Space Research*, Vol. 8, No. 4, (4)191-(4)198.
- Rishbeth H., T.J. Fuller-Rowell, D. Rees (1987): Diffusive equilibrium and vertical motion in the thermosphere during a severe magnetic storm: A computational study. *Planetary and Space Science*, Vol. 35, 1157-1165.
- Stankov S.M. (1990): A new coordinate change in mathematical modelling of the upper ionosphere. *Comptes Rendus de l'Academie Bulgare des Sciences*, Vol.43, No.11, 29-31.
- Stankov S.M. (1994): *Mathematical modelling of the upper ionosphere and the plasmasphere*, Ph.D. Thesis, Bulgarian Academy of Sciences, Sofia.
- Stankov S.M. (1996a): A steady-state F-region model and its use for satellite data analysis. *Annali di Geofisica*, Vol.39, No.5, 905-924.
- Stankov S.M. (1996b): On modelling the light-ion densities in the ionosphere. *Annali di Geofisica*, Vol. 39, No.6, 1149-1156.
- Stankov S.M. (1996c): On the variations of daytime  $H^+/O^+$  and  $He^+/O^+$  ion densities during low solar activity. *Proceedings of the 1996 Conference on Solar-Terrestrial Influences*, 29 June - 3 July 1996, Sofia, Bulgaria, 29-31.
- Stankov S.M. (1999): The oxygen-helium ion transition level during low solar activity: I. Comparison of AE-C satellite data with IRI model calculations. *Bulgarian Geophysical Journal*, Vol. 25, No.1-4, 95-116.
- Stankov S.M. (2000): The oxygen-helium ion transition level during low solar activity: II. A new empirical model. *Bulgarian Geophysical Journal*, Vol.26, No.1-4, 124-143.
- Stankov S.M. (2002): Evaluation of analytical ionospheric models used in electron density profile reconstruction. *Acta Geod. Geoph. Hung.*, Vol.37, No.2-3.
- Stankov S.M., P.Y. Muhtarov (2001): Reconstruction of the electron density profile from the total electron content using upper transition level and vertical incidence sounding measurements. *Comptes Rendus de l'Academie Bulgare des Sciences*, Vol.54, No.9, 45-48.
- Stankov S.M., I.S. Kutiev, N. Jakowski, S. Heise (2001a): Two-slope electron density profiles based on GPS TEC,  $O^+-H^+$  transition height and ionosonde data, *Proc. COST271 Workshop*, Sopron, Hungary, Proc. Paper No. WG1-13, 1-8.
- Stankov S.M., I.S. Kutiev, N. Jakowski, A. Wehrenpfennig (2001b): A new method for total electron content forecasting using global positioning system measurements, *Proc. ESTEC Workshop on Space Weather, 17-19 Dec.2001, Noordwijk, The Netherlands*.

- Stankov S.M., I.S. Kutiev, N. Jakowski, S. Heise (2002): Electron density profiles deduced from GPS TEC, O<sup>+</sup> - H<sup>+</sup> transition height and ionosonde data, *Acta Geod. Geoph. Hung.*, Vol.37, No.2-3.
- Szuszciewicz E.P., M. Lester, P. Wilkinson, P. Blanchard, M. Abdu, R. Hanbaba, K. Igarashi, S. Pulinets, B.M. Reddy (1998): A comparative study of global ionospheric responses to intense magnetic storm conditions. *Journal of Geophysical Research*, Vol.103, No.A6, 11665-11684.
- Warnant R. (1996): *Etude du comportement du Contenu Electronique Total et de ses irregularites dans une region de latitude moyenne. Application aux calculs de positions relatives par le GPS.*, Dissertation de Docteur en Sciences, Serie Geophysique (N°Hors-Serie) de l'Observatoire Royal de Belgique, Bruxelles, Belgique.
- Warnant R. (1997): Reliability of the TEC computed using GPS measurements – the problem of hardware biases. *Acta Geod. Geoph. Hung.*, Vol.32, No.3-4, 451-459.
- Warnant R. (1998): Detection of irregularities in the total electron content using GPS measurements – application to a mid-latitude station. *Acta Geod. Geoph. Hung.*, Vol.33, No.1, 121-128.
- Warnant R., J.C. Jodogne (1998): A comparison between the TEC computed using GPS and ionosonde measurements. *Acta Geod. Geoph. Hung.*, Vol.33, No.1, 147-153.



**END OF DOCUMENT**